Geoid Modelling in the Sultanate of Oman

Patrick Lasagna

A THESIS SUBMITTED TO

THE FACULTY OF GRADUATE STUDIES

IN PARTIAL FULFILLMENT OF THE REQUIREMENTS

FOR THE DEGREE OF MASTER OF SCIENCE

GRADUATE PROGRAM IN EARTH AND SPACE SCIENCE

YORK UNIVERSITY

TORONTO, ONTARIO

April, 2017

Abstract

This thesis covers the process taken to complete the Oman National Geoid Model (ONGM) project for the Sultanate of Oman. The steps taken to repair poor quality and badly referenced gravity data are explained. Each observation point was assigned a new orthometric height, its position was updated to geodetic coordinates, and its "observed" gravity was inversely calculated. The major biases that existed in the ground dataset were fixed using airborne free air anomalies at altitude. The ground data was merged with downward continued airborne gravity and the merged dataset was used to calculate the gravimetric geoid using the remove-compute-restore (RCR) method. The remove step was completed using the residual terrain model modelling technique (RTM), a General Bathymetric Chart of the Oceans (GEBCO) model mixed with a 30" NASA Shuttle Radar Topography Mission (SRTM) digital terrain model (DTM), and an expansion of the EGM08 Global Geopotential Model (GGM) to degree and order 360. The "residual anomalies" were run through the Stokes integral with Wong Gore Tapering using the GRAVSOFT software package, the effects were restored to calculate the quasigeoid. The gravimetric geoid was computed by adding the $N - \zeta$ separation term to the quasigeoid and was fitted to the GPS-on-benchmarks provided by Oman. The external accuracy of the computed gravimetric geoid is 14 cm below mean sea level (MSL) with a standard deviation of ± 30 cm.

Acknowledgements

The process of earning a master's degree is long and arduous and is certainly not done singlehandedly. This thesis became a reality with the kind support and help of many individuals. I would like to extend my sincere thanks to all of them.

I am highly indebted to Professor Spiros Pagiatakis; professor, mentor, and thesis advisor extraordinaire. He has the attitude and substance of a genius! He continually and convincingly conveys a spirit of adventure in regard to research, and expresses intense passion and excitement with respect to teaching. He provided indispensable advice, insightful comments and feedback that were instrumental in the development of this project. He was always available for my questions, and gave generously of his time and vast knowledge. He always knew where to look for the answers to obstacles while leading me to the right source, theory, and perspective. Thank you for imparting your knowledge and expertise in this study, and for your unequivocal, invaluable support, inspiration, and motivation throughout my entire university studies.

I would like to acknowledge the advice, support and insights from my secondary supervisory committee member, Professor Sunil Bisnath. Your input on an academic level has been exceptional; your wit is refreshing and I am extremely grateful for your part in helping me to achieve my educational goals, as you patiently encouraged me to explore beyond my comfort zone.

Many thanks to the National Survey Authority of Oman and IIC technologies for their gracious permission to utilize the proprietary data in my research. This thesis would not have been possible without their support. A special thank you to Pavel Novak, for his assistance in downward continuing of airborne data, which was fundamental to my project.

My thanks and appreciation go out to all my friends and colleagues. I would like to thank Athina, Sinem, and Franck for being great office mates; their continuous support, guidance, friendship, encouragement, and understanding during my graduate studies was invaluable. To Evan, River, Dennis, Sonal, Younis, Ben, Agata, and all other friends, your support and encouragement was worth more than I can express on paper; you were always there with a word of reassurance, an occasional distraction, and a listening ear; even when I was just complaining.

Last, but not least, I am thankful to my parents Rosie and Peter, my sister Sarah, and the rest of my extended family, who have given their continuous and endless love, unceasing encouragement, patience, and support my entire life regardless of the circumstances. My parents always encouraged me to ask questions and to be curious about how things work. They taught me the value of hard work and an education. All the support they have given me over the years is the greatest gift one can receive. This journey would not have been possible if not for them.

Table of contents

List of tables

List of figures

List of acronyms

Acronyms are listed in the order they appear in the thesis.

ONGM – Oman National Geoid Model

RCR – Remove Compute Restore

RTM – Residual Terrain Model

GEBCO - General Bathymetric Chart of the Oceans

NASA - National Aeronautics and Space Administration

SRTM - Shuttle Radar Topography Mission

DTM – Digital Terrain Model

EGM08 - Earth Gravitational Model 2008

GGM - Global Geopotential Model

GPS – Global Positioning System

MSL – Mean Sea Level

PDO - Petroleum Development of Oman

NSA - National Survey Authority

UTM - Universal Transverse Mercator

WGS84 - World Geodetic System 1984

3D – Three Dimensional

BVP – Boundary Value Problem

FEPG – Fundamental Equation of Physical Geodesy

GOCO05S - Gravity Observation Combination Model 5S

OGBN - The Oman Gravity Base Network

IAGBN - International Absolute Gravity Base Network

IGSN71 - International Gravity Standardization Network of 1971

PSD93 - PDO Survey Datum of 93

GRS67 - Geodetic Reference System 1967

EGM96 - Earth Gravitational Model 1993

RET – Rock Equivalent Topography

GFZ - German Research Centre for Geosciences

ICGEM - International Center for Global Earth Models

FFT – Fast Fourier Transform

GNSS - Global Navigation Satellite System

SST – Sea Surface Topography

List of symbols

Symbols are listed in the order they appear in the thesis.

F	Attractive force between two masses
m_1, m_2	Masses that Attract each other
ℓ	Euclidian distance between the two masses
G	Newton's Gravitational Constant
F_X, F_Y, F_Z	Force components in the X,Y, and Z direction
V	Potential of Gravitation
$\frac{\partial V}{\partial n}$	First normal derivation of potential of gravitation
S	Surface that V is available above or below
Δ	Laplacian operator
V_e	Exterior potential outside S
W	Gravity potential
∂W	Change of potential
g	Gravity Vector
U_0	Normal potential
W_0	The geoid's constant geopotential value
H	Orthometric height
P	Terrain observation point
dH	Change in orthometric height along the plumbline
N	Geoid undulation
U	Normal Potential

T	Anomalous Potential
γ	Theoretical gravity on reference ellipsoid
Δg	Gravity anomaly
g_P	Gravity observed on the terrain
Q	Point on reference ellipsoid beneath P
γ_Q	Normal gravity on reference ellipsoid
R	Mean radius of the earth
σ	Integration over the surface of the earth
$S(\psi)$	Stokes Function
ψ	Spherical Distance
(θ, λ)	Computation point spherical coordinates
(θ', λ')	Running point spherical coordinates
h	Geodetic height of a point above the reference ellipsoid
Δg_{fa}	Free Air gravity anomaly
g_G	Gravity measured on the ground
Δg_{ba}	Bouguer gravity anomaly
ρ	Density; taken as 2.67 g/cm^3
ζ	Height Anomaly
h^*	Normal height
$\widetilde{\Delta g}$	Molodenskij gravity anomaly
G_1	Molodenskij correction to the Stokes function
C_i	Geopotential number
δS	Transformation Scale factor
R_X, R_Y, R_z	Transformation Rotation Factors

$\Delta x, \Delta y, \Delta z$	Transformation Translation Factors
(Φ, λ)	Geodetic coordinates (latitude and longitude)
$\Delta g_{ba\_complete}$	Complete Bouguer gravity anomaly
c_p	Classical Roughness term for a point
δg	Gravity Disturbance
K	Observation point at altitude
g_K	Observed gravity at altitude
γ_K	Normal gravity at altitude
H_a	Orthometric height of airborne observation point
$\Delta g(r, \Omega)$	Downward Continued gravity anomaly
$G(\phi, \lambda)$	Gaussian filter
d	Spatial distance of Guassian filter
σ_{km}	Gaussian filter cutoff frequency
Δg_{ter}	Terrain effects on gravity anomalies
H_{ref}	Reference height surface
$SRTM_{[3" \times 3"]}$	$3" \times 3"$ gridded SRTM dataset
$SRTM_{[30" \times 30"]}$	$30" \times 30"$ gridded SRTM dataset
$SRTM_{ref}{}_{[30" \times 30"]}$	$30" \times 30"$ gridded reference SRTM dataset
$\Delta g_{fa}{}_{[30" \times 30"]}$	$30" \times 30"$ gridded free air anomalies
$c_p{}_{[30" \times 30"]}$	$30" \times 30"$ gridded roughness correction terms
$\Delta_{BA}{}_{[30" \times 30"]}$	$30" \times 30"$ gridded bouguer slab differences
$\Delta g_{ter}{}_{[30" \times 30"]}$	$30" \times 30"$ gridded terrain effects
$\Delta g_{egm08}{}_{[30" \times 30"]}$	$30" \times 30"$ gridded EGM08 gravity anomalies

$\Delta g_{res_{[30"\times 30"]}}$	$30" \times 30"$ gridded residual gravity anomalies
$S_{mod}(\psi)$	Stokes function modified with Wong-Gore tapering effects
$\zeta_{\Delta g_{res}[30"\times 30"]}$	$30" \times 30"$ gridded height anomalies from residual gravity anomalies
$\zeta_{egm08_{[30"\times 30"]}}$	$30" \times 30"$ gridded EGM08 height anomalies
$\zeta_{\Delta g_{ter}[30"\times 30"]}$	$30" \times 30"$ gridded height anomalies from terrain effects
$\zeta_{[30"\times 30"]}$	$30" \times 30"$ gridded height anomalies
$\Delta g_{sbg_{[30"\times 30"]}}$	$30" \times 30"$ gridded simple bouguer anomalies
$(N-\zeta)_{[30"\times 30"]}$	$30" \times 30"$ gridded geoid-height anomaly separation
$N_{[30"\times 30"]}$	$30" \times 30"$ gridded geoid
ΔN	Difference between geometric and gravimetric geoid
$N_{fitted_{[30"\times 30"]}}$	$30" \times 30"$ gridded fitted geoid

1 Introduction

The fundamental task of geodesy is to study the varying shape, size, and gravity field of the Earth. While mathematical approximations of Earth's shape exist in the form of reference ellipsoids, a physically defined surface describing its shape is required. The geoid takes into account all masses and mass distributions present, and best describes the physical shape of the Earth.

Observed gravity and terrain elevations are the fundamental quantities required to calculate the geoid. The gravity observations and computed gravity anomalies with respect to a model Earth, allow for the characterization of mass distribution that might not otherwise be observable. The geoid is calculated using Stokes integral (Hofmann-Wellenhof & Moritz, 2006) as a low-pass convolution filter of gravity anomalies over the entire surface of the Earth. The result is an equipotential surface that approximates mean sea level globally. If precise gravity measurements are collected over the surface of the Earth, and the topographic masses above the geoid are mathematically or physically removed, then computing the geoid is a straightforward application of the Stokes integral.

In addition to characterizing the shape of the Earth, the geoid also functions as a level surface to which orthometric heights refer. To transfer elevation from one point to another, spirit levelling is most commonly used; the difference in heights is measured using a level instrument and two levelling rods. When spirit levelling is carried out over large distances, multiple setups must be made to transfer elevation from a point on the coast at mean sea level, to a point thousands of kilometers away. To take into consideration the varying mass distribution of the topographic masses, spirit levelling must always be combined with gravity measurements to establish orthometric heights. This is a time consuming and costly endeavor.

With the advent of high accuracy global positioning system (GPS) measurements, the geoid can also be used as an alternative to spirit levelling. Since geodetic heights (GPS, or ellipsoidal heights) relate the terrain to the reference ellipsoid, and the geoid deviates from the reference ellipsoid, the height between the geoid and the terrain (orthometric height) can be determined without levelling. This method of geometrically determining orthometric heights is an attractive alternative to spirit levelling, despite the additional gravity observations and calculations required to compute the geoid.

1.1 The Oman National Geoid Model project

In 2013, the Sultanate of Oman desired a national geoid model, initiating the Oman National Geoid Model (ONGM) Project. A legacy ground gravity dataset was available from the National Survey Authority (NSA) of Oman, with approximately 230 000 point gravity observations divided into 82 survey lines. In addition, a newly observed ground gravity dataset of 6000 points, a newly observed airborne dataset with countrywide coverage (Géophysique GPR I'ntl Inc., 2015), and a set of GPS observations on Oman's current leveled benchmarks were available from the Sultanate of Oman for the development of their national geoid model.

1.2 Objective of work

The calculation of a geoid model requires the availability of a digital terrain model, and a reliable and accurate gravity dataset. The initial Oman ground gravity dataset was not sufficient for geoid computation. It was observed over a period of at least fifty years and critical metadata were not available. The dataset as a whole was incomplete; each point contained a Universal Transverse Mercator (UTM) northing and easting coordinate, several previously calculated Bouguer anomalies of different kinds, and the point's survey line (survey project) identification. However, not all points had a supplied elevation, or sufficiently accurate latitude and longitude. More importantly, only 25 percent of the points were supplied with an observed gravity value, which is essential for the calculation of gravity anomalies necessary for the geoid computation. In addition to the above, the gravity data were referenced to both the old horizontal (ellipsoid) and gravity datums that are incompatible with new modern reference systems. These issues do not allow for the merging of ground gravity observations with airborne measurements to fully characterize the Earth's gravity field, and furthermore, prevent the calculation of an accurate complete geoid.

This thesis undertakes the steps required to complete the ONGM project. This process involves the repair of biased ground gravity data, its integration with an airborne gravity dataset using spatial filtering, the calculation of the gravimetric geoid using the remove-compute-restore method, and the subsequent fitting of the geoid to the GPS-on-benchmarks.

1.3 Thesis contributions

The major contribution of this thesis is the workflow to resolve the deficiencies in the ground gravity dataset presented above to get the ground gravity dataset to a reasonable accuracy level, so that it can be merged with airborne gravity measurements for a complete geoid

model calculation. This workflow can be applied to other biased, low quality, ground gravity datasets in other countries. In addition to the reclamation process of the low-quality gravity dataset, other contributions of this thesis include: creation of automated geoid calculation workflows, a rigorous geoid solution testing scheme, the fitting of a geoid solution to GPS-on-benchmarks; Python software development related to gravity grid merging, gravity and vertical datum shifts, integration of gridded results in multiple formats from multiple sources, and gravity observation line bias detection.

1.4 Overview of methods

In this research, the following methodology is used to repair the deficiencies of the ground gravity data. The observation points are transformed from their supplied Universal Transverse Mercator (UTM) coordinates on Clarke 1880 ellipsoid to their geodetic coordinates and UTM coordinates referenced to the World Geodetic System 1984 (WGS84). Then, the orthometric height for each point is replaced with an interpolated orthometric height from the NASA Shuttle Radar Topography Mission (SRTM) digital terrain model. The observed gravity is then inversely calculated from the corresponding Bouguer gravity anomaly provided at each observation point by making assumptions about the crustal density. Finally, the heavily biased gravity values that were apparently referenced to gravity benchmarks with arbitrary gravity values are repaired using the airborne data, in the gravity anomaly space resulting in an unbiased ground free air gravity anomaly dataset, covering the entire country.

1.5 Layout of thesis

This thesis elaborates on the steps required to transform poor quality ground gravity data and airborne gravity measurements into an unbiased and consistent dataset. Chapter 2 presents the basic background theory pertaining to the Oman geoid modelling process, as well as a literature review on the most common methods of calculating the geoid in practice is introduced. Chapters 3 to 5 detail the steps taken to repair the ground data, remove their biases, and integrate them with the airborne measurements, to obtain free air gravity anomalies that are used to calculate the Oman geoid model. In Chapter 6, the software workflow used to calculate the geoid using Python and the GRAVSOFT software package (Forsberg & Tscherning, GRAVSOFT, 2008) is presented and explained. Lastly, the results of the calculations as well as recommendations for future work are presented in Chapters 7 and 8, respectively.

2 Theory of geoid modelling

2.1 Attraction and potential

Newton's law of gravitation states that two objects with point masses m_1 and m_2 seperated by a distance ℓ will be attracted to each other with a force equal to (Hofmann-Wellenhof & Moritz, 2006):

$$F = G\frac{m_1 m_2}{\ell^2} \tag{2.1}$$

where G is the Newton's gravitational constant. When one mass is significantly larger than the other (e.g. $m_1 \gg m_2$), then it is convenient to call the smaller mass the attracted mass and set it equal to unity. In a 3D-Cartesian system (x, y, z), the force between the attracting mass $P(x_P, y_P, z_P)$, and the attracted mass $Q(x_Q, y_Q, z_Q)$ can be given in component form by:

$$F_X = -G\frac{m}{\ell^2}\frac{x_P - x_Q}{\ell} \tag{2.2}$$

$$F_Y = -G\frac{m}{\ell^2}\frac{y_P - y_Q}{\ell} \tag{2.3}$$

$$F_Z = -G\frac{m}{\ell^2}\frac{z_P - z_Q}{\ell} \tag{2.4}$$

where ℓ is the Euclidian distance between P and Q. The scalar function V, called the potential of gravitation can be expressed with Equation (2.5).

$$V = \frac{Gm}{\ell} \tag{2.5}$$

Equations (2.2), (2.3), and (2.4) can be expressed as partial derivatives of V with respect to the coordinate axes $x, y,$ and z.

$$F_X = \frac{\partial V}{\partial x}, F_Y = \frac{\partial V}{\partial y}, F_Z = \frac{\partial V}{\partial z} \tag{2.6}$$

The potential of gravitation is used to represent the components $F_X, F_Y,$ and F_Z using a single function.

2.2 Geodetic boundary-value problems

The three boundary-value problems (BVP) used in physical geodesy provide a way of relating the scalar potential function V, or its first normal derivative $\frac{\partial V}{\partial n}$, or a linear combination of both given as boundary values on a surface S, to values of V at other locations. Their primary purpose is to determine the harmonic potential function V in a region of space inside or outside the surface S as a function of the given boundary values (Hofmann-Wellenhof & Moritz, 2006).

A function is harmonic in a region if it satisfies Laplace's equation at every point of the region. Laplace's equation is shown below in Equation (2.7) (Hofmann-Wellenhof & Moritz, 2006),

$$\Delta V = \frac{\partial^2 V}{\partial x^2} + \frac{\partial^2 V}{\partial y^2} + \frac{\partial^2 V}{\partial z^2} = 0 \tag{2.7}$$

where V is the harmonic function of interest, and Δ is the Laplacian operator.

In addition to the Laplace equation above, if the region is a closed surface S, then the harmonic function should approach zero proportionally to $1/\ell$ as ℓ approaches infinity (Hofmann-Wellenhof & Moritz, 2006).

The first BVP is also known as *Dirichlet's* problem. Given any function V on a surface S, find a function V' that is harmonic either inside or outside S that satisfies the boundary values V on S (Heiskanen & Moritz, 1967). Dirichlet's problem applied to gravitational potential is as follows: given the value(s) of the gravitational potential function V at a boundary surface S, find the potential in the interior V_i and exterior V_e of the boundary surface. Of particular interest to geodesy is the gravitational potential outside the boundary, which is solved in closed form using Poisson's integral.

The second BVP is known as *Neumann's* problem. In contrast to the first BVP, instead of a function V on the surface S, its first normal derivative $\frac{\partial V}{\partial n}$ on the surface is provided. The first normal derivative is perpendicular to and directed outwards from S as demonstrated in Figure 2-1. The goal is the same as the 1st BVP: find the harmonic function V inside or outside S that satisfies the boundary values $\frac{\partial V}{\partial n}$ on S. Finding a harmonic function for the exterior problem V_e, is particularly important to geodesy.

The third BVP, also known as the boundary-value problem of physical geodesy, combines the first and second BVP's. Given a linear combination of the function V and its first normal derivative $\frac{\partial V}{\partial n}$ on the boundary surface S, find the harmonic function V inside or outside S that also

satisfies the boundary values on S. The third BVP is extremely important because its solution for the exterior potential V_e, the Stokes integral, allows for the determination of the geoid undulations from a reference ellipsoid (Hofmann-Wellenhof & Moritz, 2006).

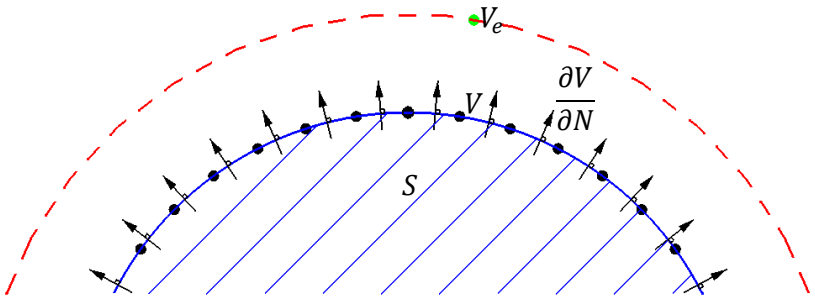

Figure 2-1. Boundary-value problems. *This figure displays the third BVP. The dotted red surface denoted by V_e is the value of V outside the blue boundary surface S. The linear combination of V and its first normal derivative $\frac{\partial V}{\partial N}$ are available as boundary values on the surface, denoted by the black arrows and black dots respectively.*

2.3 Gravity and level surfaces

The total force acting on a point mass at rest on the Earth's surface is the sum of the gravitational attraction from the Earth's mass and the centrifugal force from the Earth's rotation. This force results in acceleration called gravity and is represented by the gravity vector g, and its potential field is represented by the geopotential W (Hofmann-Wellenhof & Moritz, 2006).

A surface on which the gravity potential W is equal to a constant value is called an equipotential or level surface. The downward gradient of the gravity potential, the gravity vector, is orthogonal to the equipotential surface passing through the same point (Hofmann-Wellenhof & Moritz, 2006). The change in potential ∂W with respect to the normal vector n, the negative vertical gradient, is given by Equation (2.8),

$$\frac{\partial W}{\partial n} = -g \tag{2.8}$$

where g is the gravity vector, and n is the normal vector to the equipotential surface.

An ellipsoid of rotation is a common mathematical approximation for the shape of the Earth. The surface of this ellipsoid is an equipotential surface of normal potential U_0 when the ellipsoid includes in it the total mass of the solid earth, oceans, and atmosphere, and spins with angular velocity ω equal to Earth's spin.

If all of the oceans were left to settle without the influence of any dynamics of the Earth or ocean currents, tidal effects, and other geodynamic phenomena, they would form an equipotential surface. This equipotential surface would also represent the mean sea level that is also known to represent the geoid. The equipotential surface corresponding to the geoid has a constant geopotential value W_0, which may also be set to be equal to the normal potential U_0 on the surface of the reference ellipsoid. There are an infinite number of equipotential surfaces corresponding to an infinite number of potential values $(W_1 \dots W_n)$. The level surfaces will not be parallel to each other due to anomalous mass distribution within the Earth. The non-parallelism of level surfaces is shown in Figure 2-2. Lines that intersect all level surfaces orthogonally are called plumb lines. Since the level surfaces are not parallel, these plumb lines will be curved; this is shown in Figure 2-2. The gravity vector at any point is tangent to the plumb line at that point (Hofmann-Wellenhof & Moritz, 2006).

The orthometric height H of a terrain point P is given by the length of the plumb line from the geoid to the point, measured upwards. To determine the change in potential between the geoid and the measured terrain point, Equation (2.8) can be used with a single change; the term dn is replaced with dH, which is the upward pointing vector along the plumb line towards the terrain point. Since the gravity vector g is pointing downwards, and dH is measured upwards, the angle between them is 180° and Equation (2.8) can be rewritten as,

$$dW = \|g\|\|dH\| \cos 180° = -g dH \tag{2.9}$$

where g is the gravity vector, and dH is the change of orthometric height along the plumb line. Equation (2.9) relates dynamic components dW to geometric ones dH (Heiskanen & Moritz, 1967).

One important use of a level surface is to provide a reference surface for heights. The geoid is the most commonly used level surface as it represents mean sea level. Figure 2-2 shows the relationship between the terrain, the geoid, and mean sea level.

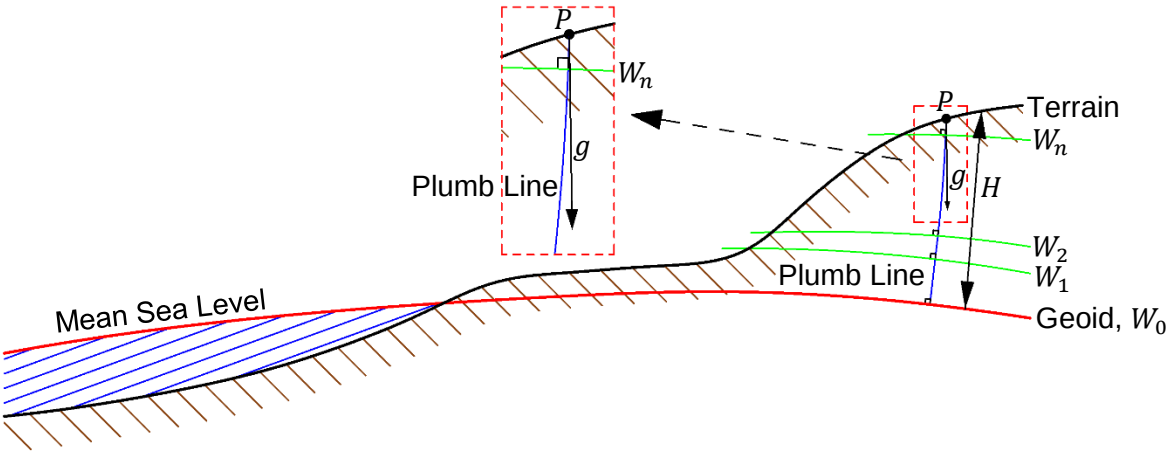

Figure 2-2. Level surfaces. *Level surfaces with different values of W will not be parallel to each other. This is due to the anomalous mass distributions in Earth's interior. The plumb line is orthogonal to every level surface and as a result, it will have a slight curve. The gravity vector g at a level surface n is orthogonal to W_n and tangent to the plumb line at the point where it crosses W_n.*

2.4 Anomalous potential and gravity anomalies

The reference ellipsoid is a relatively close assumption $(\pm\ 100\ m)$ to the true shape of the Earth, the geoid. The gravity potential on the geoid is usually set to be identical to the normal potential on the reference ellipsoid, that is, $W_0 = U_0$. Therefore, it is mathematically convenient to represent the geoid, as the normal ellipsoid plus the geoid undulation N, and the gravity potential W, as the normal potential U plus the anomalous potential T. The geoid and reference ellipsoid are compared in Figure 2-3. Using Bruns formula (Hofmann-Wellenhof & Moritz, 2006), the geoid undulation N is related to the anomalous potential T on the geoid and normal gravity γ (theoretical gravity) on the reference ellipsoid using Equation (2.10).

$$N = \frac{T}{\gamma} \tag{2.10}$$

The gravity vector on the geoid can also be defined as the systematic normal gravity vector on the ellipsoid plus a correction term called the gravity anomaly vector Δg. In practice, however, the magnitude of gravity anomaly is expressed using Equation (2.11). It is the difference between the magnitude of the gravity vector on the geoid g_p at point P, and the magnitude of normal gravity γ_Q on the reference ellipsoid at point Q.

$$\Delta g = g_P - \gamma_Q \tag{2.11}$$

The difference in direction of vectors g_p and γ_Q in Equation (2.11) is called the deflection of the vertical; it is often very small and it is outside the scope of this thesis, because its effect on

gravity anomalies is very small so it will not have a measurable effect on the geoid. Figure 2-3 shows the gravity vector g_p on the geoid with normal n, and the normal gravity vector γ_Q on the ellipsoid with normal n'.

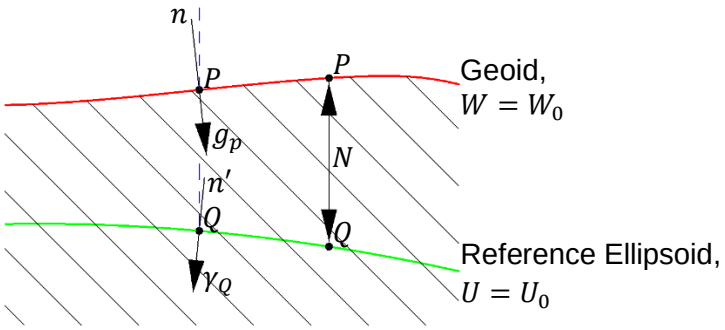

Figure 2-3. Geoid and reference normal ellipsoid.

2.5 The fundamental equation of physical geodesy

The fundamental equation of physical geodesy (FEPG), shown in Equation (2.12), is the fundamental partial differential equation that relates the unknown anomalous potential T and its normal derivative to a measureable quantity Δg (Hofmann-Wellenhof & Moritz, 2006).

$$\frac{\partial T}{\partial h} - \frac{1}{\gamma}\frac{\partial \gamma}{\partial h}T + \Delta g = 0 \tag{2.12}$$

Since Δg is not known throughout space, Equation (2.12) has no solution; however, if Δg is known over the boundary surface of the geoid, then the partial differential equation in Equation (2.12) can be used as a boundary value condition when solving the third BVP for the anomalous (disturbing) potential T.

If no masses exist above the geoid, then the anomalous potential T is harmonic outside the geoid and satisfies Laplace's equation ($\Delta T = 0$). Therefore,

$$\Delta T \equiv \frac{\partial^2 T}{\partial x^2} + \frac{\partial^2 T}{\partial y^2} + \frac{\partial^2 T}{\partial z^2} = 0 \tag{2.13}$$

is solvable for T at every point outside the geoid, subject to the boundary condition given by the FEPG in Equation (2.12) (Hofmann-Wellenhof & Moritz, 2006).

If Δg is known (given) over the entire surface of the geoid, then a linear combination of T and its first normal derivative $\frac{\partial T}{\partial h}$ is known on the boundary surface S, here the geoid (cf. Equation (2.12)). Therefore, the solution of Equation (2.13) outside S can be achieved using Equation (2.12) as a boundary condition, leading to the third boundary-value problem of potential theory (Hofmann-Wellenhof & Moritz, 2006).

On the geoid, the solution for T at a point is given by Stokes formula (Hofmann-Wellenhof & Moritz, 2006), and is shown in Equation (2.14),

$$T = \frac{R}{4\pi} \iint_{\sigma} \Delta g \; S(\psi) d\sigma \tag{2.14}$$

where R is the mean radius of the Earth, and Δg are gravity anomalies that refer to the geoid with no masses above it. The double integral limit is carried over the entire globe σ and the gravity anomaly varies with the moving point p' on the sphere. $S(\psi)$ is the Stokes function at the spherical distance ψ between points p and p' and is given by Equation (2.15),

$$S(\psi) = \frac{1}{sin(\psi/2)} - 6\, sin\left(\frac{\psi}{2}\right) + 1 - 5cos\psi - 3cos\psi \, ln\left(sin\left(\frac{\psi}{2}\right) + sin\left(\frac{\psi}{2}\right)^2\right) \tag{2.15}$$

where ψ is the spherical distance between the vectors taken from the center of the Earth to the running point (θ', λ') being iterated over σ, and the point of computation at (θ, λ). $S(\psi)$ acts as a weighting function for the gravity anomalies in Equation (2.14) and is plotted in Figure 2-4.

The formula to calculate the spherical distance ψ between points $p(\theta, \lambda)$ and $p'(\theta', \lambda')$ in polar coordinates is given by Equation (2.16), and Figure 2-5 displays the spherical distance ψ between the two points p and p'.

$$\psi = cos^{-1}(sin\theta sin\theta' + cos\theta cos\theta' \, cos(\lambda' - \lambda)) \tag{2.16}$$

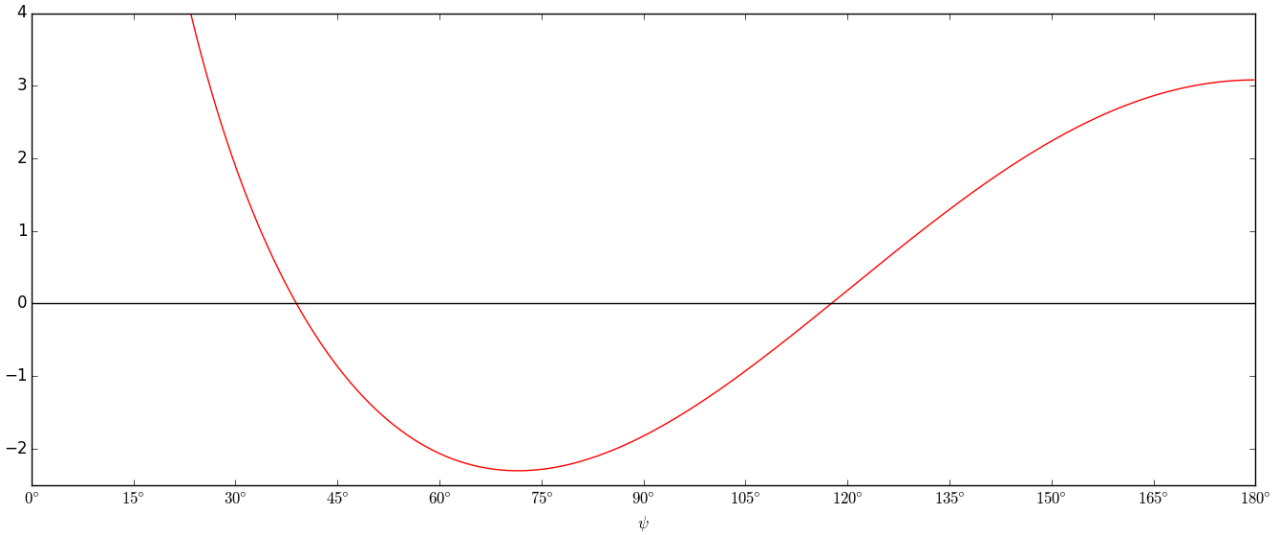

Figure 2-4. Stokes function $S(\psi)$. *This figure displays the value of* $S(\psi)$ *as* ψ *varies from* $0°$ *to* $180°$. *Smaller spherical distances correspond to much larger weights which have been truncated to illustrate smaller weights. The weighting function increases as the spherical distance passes* $120°$,*because masses opposite the computation point, present on the other side of the Earth, begin to have a larger contribution to the calculation.*

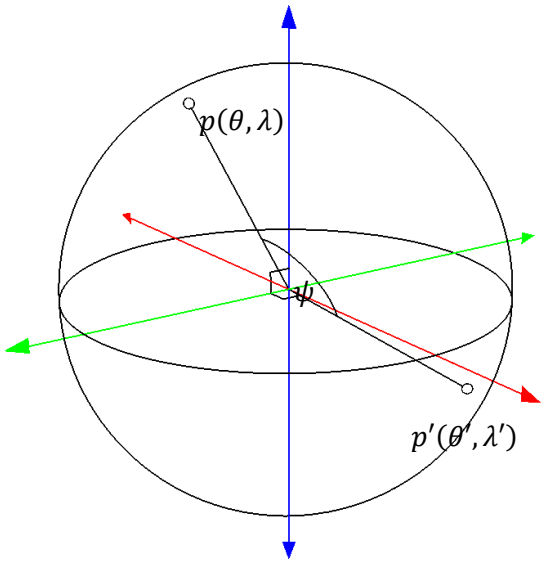

Figure 2-5. Spherical distance in spherical coordinates.

2.6 The geoid

The geoid is a mathematically modelled equipotential surface that approximates mean sea level globally. It describes the shape of the Earth, taking into account all masses and mass distributions present. Since the masses and their distribution are not readily known or measureable, values of gravity g measured on and above the Earth's surface are used. The geoid

can be calculated from gravity anomalies and a digital terrain model (DTM) using the Stokes integral, which is derived by substituting Equation (2.14) into Bruns formula (2.10) and is shown below in Equation (2.17). The Stokes integral is a low-pass filter (convolution integral) over the entire surface of the Earth that is used to compute the geoid undulation N for a single computation point P. Unless stated otherwise, all equations are from Hofmann-Wellenhof & Moritz (2006).

$$N = \frac{R}{4\pi\gamma_0} \iint_{\sigma} \Delta g \, S(\psi) d\sigma \tag{2.17}$$

N is the geoid undulation, the height of the geoid from a reference ellipsoid and γ_0 is the normal gravity on the reference ellipsoid Q corresponding to point P where the geoid undulation is being calculated. The geometry of the problem can be seen in Figure 2-6.

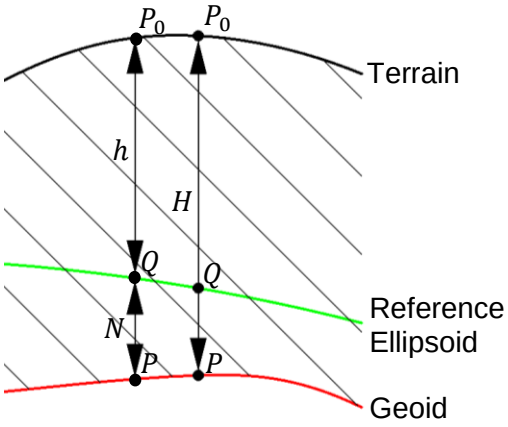

Figure 2-6. Relationship between the terrain, a reference ellipsoid, and the geoid. *The geodetic height h plus the geoid undulation N equals the orthometric height H.*

The integral limit in Equation (2.17) is of extreme importance, as gravity anomalies are required all over the surface of the Earth to properly determine N. In practice, one might have access to gravity anomaly grids at high or medium spatial resolution (i.e. 30" or better for the area of interest), but not for the rest of the Earth. To deal with this lack of gravity information, gravity is approximated outside the area using a global gravity model, such as EGM08 or GOCO05s.

The Stokes integral has two requirements that must be fulfilled for the results to be correct. First, as the solution to the geodetic boundary-value problem, the Stokes integral requires the gravity anomalies to represent the boundary-values on the geoid. That is, g_P must refer to the geoid. Second, there must be no masses present outside the geoid, ensuring that g on the geoid truly is the boundary surface (Hofmann-Wellenhof & Moritz, 2006), as the BVP's used in physical geodesy are the solution to Laplace's Equation, and $\Delta V \neq 0$ if masses exist above S.

2.7 Gravity anomalies

The gravity anomalies required as input for Stoke's formula or integral are given by Equation (2.11). The gravity on the geoid g_p and the gravity on the reference ellipsoid γ_Q must be defined, such that there are no masses present above the geoid, to satisfy the requirements of the boundary value problems. Since gravity cannot be measured on the geoid, gravity measured on or above the Earth's surface must be reduced to the geoid. Furthermore, even if gravity could be measured at the geoid, all the mass on Earth above the geoid would have to be removed. This changes the mass distribution of the Earth, making it impossible to determine the actual geoid.

If the masses above the geoid are ignored, then gravity measured on the ground (terrain) g_G can be reduced to the geoid to acquire g_p using a free air gradient in Equation (2.18). The resultant gravity anomaly computed with Equation (2.11) is called a free air anomaly Δg_{fa}.

$$\Delta g_{fa} = g_G + 0.3086H - \gamma_Q \tag{2.18}$$

The free air gradient present in the second term on the right-hand-side assumes that the point is floating in space, and is downward continued to the geoid through the "free air". The gravity value increases as a result of its observation point being moved closer to the center of mass of the Earth.

Bouguer anomalies deal with the terrain that is ignored by the free air gradient. There are two types of Bouguer anomalies, simple and complete. The complete Bouguer anomaly will be mentioned in Chapter 4. Equation (2.19) shows the calculation of a simple Bouguer anomaly

$$\Delta g_{ba} = \Delta g_{fa} - 2\pi G\rho H \tag{2.19}$$

where G is the universal constant of gravity, ρ is the density of the slab, generally taken with mean rock density $(2.67 g/cm^3)$, and H remains the orthometric height of the point.

The Bouguer anomaly is the free air anomaly corrected by the simple Bouguer reduction term. The term corresponds to the gravitational attraction of an infinite (area) slab of density ρ and height H, over the computation point. The correction is subtracted from the free air anomaly, representing the "restoring" of the attraction provided by the infinite slab, away from the center of mass of the Earth.

2.8 The quasigeoid and the theory of Molodenskij

To bypass the second constraint of the Stokes integral, the theory of Molodenskij is used. The terrain replaces the geoid as the boundary surface, and the result of the Stokes integral is the quasigeoid, instead of the geoid. While the quasigeoid is approximately equivalent to the geoid in terms of shape, unlike the geoid, it has no physical meaning and is merely a mathematical surface of convenience (Vanicek, 1974). Figure 2-7 shows the relationship between the terrain, the reference ellipsoid, the quasigeoid, and a new surface, the telluroid.

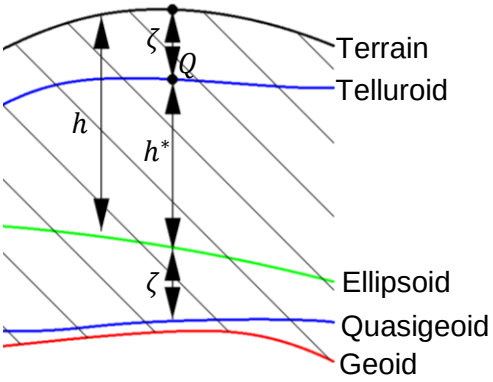

Figure 2-7. Relation between classical surfaces in geodesy and Molodenskij surfaces. *The telluroid, terrain, and reference ellipsoid are related in a similar way to the terrain, the reference ellipsoid, and the geoid. When dealing with Molodenskij surfaces, the geodetic height h is equal to the sum of the normal height h^* and the height anomaly ζ. By comparison, the orthometric height can be determined by adding the geoid undulation from the reference ellipsoid N, to the geodetic height h*.

The difference between the geodetic height h and the normal height h^* defines the height anomaly ζ, which is numerically close to the geoid undulation N. Similar to the concept of the geoid undulation N, with respect to the reference ellipsoid, the height anomaly can also be used as a deviation of another surface from the reference ellipsoid, namely the quasigeoid or it can be seen as a deviation of another surface from the terrain known as the telluroid surface. The height anomaly ζ is the result of Molodenskij's equivalent to the Stokes integral shown in Equation (2.20) (Vanicek, 1974),

$$\zeta = \frac{R}{4\pi\gamma_0}\iint_{\sigma}\left(\widetilde{\Delta g} + G_1\right) S(\psi)\, d\sigma \tag{2.20}$$

where γ_0 is the normal gravity on the telluroid, and $\widetilde{\Delta g}$ are not the free air anomalies mentioned in Equation (2.11); rather, the ones expressed using Equation (2.21),

$$\widetilde{\Delta g} = g_P - \gamma_Q \tag{2.21}$$

where P is a point on the terrain and Q is its corresponding point on the telluroid. The additional component inside the integral G_1 is the Molodenskij correction term to the Stokes function, and is shown in Equation (2.22) (Vanicek, 1974),

$$\mathrm{G}_1 = \frac{R^2}{2\pi}\iint_{\sigma}\frac{H'-H}{\rho^3}\left(\widetilde{\Delta g}+\frac{3\gamma_0}{2R}\zeta_0\right)d\sigma \tag{2.22}$$

where H is the orthometric height of the computation point, H' is the orthometric height of the moving point in the integral, ρ is the standard mean rock density of $2.67 g/cm^3$, $\widetilde{\Delta g}$ and γ_0 remain the same as in Equation (2.20), and ζ_0 is the result of Equation (2.20) ignoring G_1.The G_1 term is very small compared the value of ζ_0, and is often neglected (Vanicek, 1974).

This thesis makes use of the method of Molodenskij to calculate the quasigeoid, but neglects the G_1 term from Equation (2.22) based on (Vanicek, 1974), and uses the classical free air gravity anomalies defined using Equation (2.11) instead of the gravity anomalies defined by Equation (2.21) i.e $\Delta g \cong \widetilde{\Delta g}$ because thetwo gravity anomalies are numerically similar (see below).

Classical free air gravity anomalies are calculated using gravity measured on the ground downward continued in the free air a distance H to the geoid using the free air gradient acquired from Brun's generalized formula by setting $\rho = 0$, calculating g from the Somigliana-Pizzetti normal field (Heiskanen & Moritz, 1967), and taking J as the mean curvature of the equipotential surface of the normal gravity field. Molodenskij free air gravity anomalies use normal gravity on the ellipsoid upward continued a distance h^* from the ellipsoid to the telluroid using the accurately determined free air gradient of Molodenskij, which, on average, has the same value as the normal gravity gradient calculated from Brun's formula mentioned above. The two gravity anomalies differ by the following:

$$0.3086 \times (H - h^*)\ mGal \tag{2.23}$$

The difference between H and h^* is the same as N and ζ and is negligible when dealing with gravity anomalies. In an exaggerated case, if the difference between the two heights is equal to 2m, then the difference in gravity anomalies will be ~ 0.6 mGal; insignificant when calculating the geoid. From the above, Δg is calculated from the downward continuation of terrain gravity and it is by nature numerically unstable and perhaps theoretically impossible to achieve, whereas $\widetilde{\Delta g}$ is the upward continuation of normal gravity on the ellipsoid, an operation that is numerically

stable and theoretically correct. Therefore, it is physically and numerically more meaningful to use $\widetilde{\Delta g}$ (surface gravity anomaly) and Molodenskij's theory to calculate ζ and subsequently N, rather than using Δg assuming that it is defined on the geoid and Stokes' integral to calculate the geoid. Molodneskij's theory is therefore adopted in the research.

Since Equation (2.20) computes the quasigeoid instead of the geoid, an additional correction namely $N - \zeta$ separation term must be added to it. It is given by Heiskanen & Moritz (1967) in Equation (2.24).

$$N - \zeta \approx \frac{\Delta g_{ba} H}{\bar{\gamma}} \tag{2.24}$$

The term is estimated by using the simple Bouguer anomalies Δg_{ba} (Equation (2.19)), the orthometric height H, and mean normal gravity $\bar{\gamma}$, which is $9.81\ m/s^2$.

2.9 Spirit levelling and gravity

One major surveying task is the process of geodetic (spirit) levelling, which aims to measure the difference in elevation between two points. If the points are separated by a large distance, multiple levelling setups must be made. The final difference in elevation is computed by summing up the height differences of each setup. It is through this method that the orthometric height H of a point can be transferred to another point when gravity along the levelling route is also measured. The process for a single setup is shown in Figure 2-8.

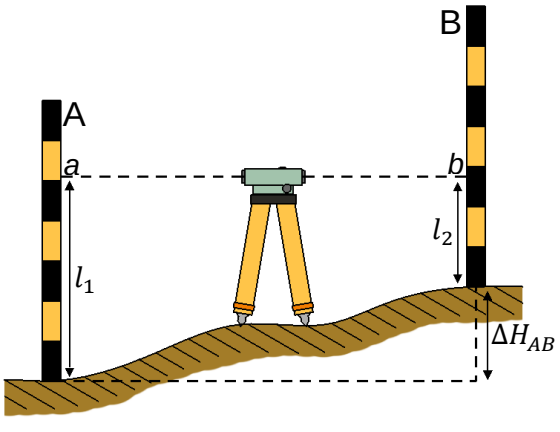

Figure 2-8. A spirit levelling setup*. The difference in rod readings at point A and B (l_1 and l_2 respectively) will give the change in height between A and B, if the line between a and b is horizontal and the distance between A and B is short (i.e. less than 50 m).*

If perfectly observed height differences for each setup in a closed levelling loop are added together, the sum will not be rigorously zero (Hofmann-Wellenhof & Moritz, 2006). In addition, if an alternate path is taken to complete the levelling loop, the sum of the levelled differences will not be zero and will not be the same if another arbitrary path is followed. This path-dependence is due to the non-parallelism of level surfaces mentioned previously; the geometric, observed height difference for a setup is not the same as the physical, orthometric height difference. The inconsistency between the two height differences can only be eliminated if Earth's gravity field is accounted for.

The Helmert orthometric height at a point P_i on the terrain is defined by Equation (2.25) (Hofmann-Wellenhof & Moritz, 2006),

$$H_i \approx \frac{C_i}{g_i + 0.0424\ell} \tag{2.25}$$

where C_i is the geopotential number, g_i is the measured gravity and ℓ is the leveled height, all at point P_i. The geopotential number is determined by measuring levelled height differences and gravity along the levelling path (see Equation (2.26)), and the coefficient 0.0424 is one-half of the Poincaré-Prey gravity gradient in mGal/m along the plumb line at P_i. The Poincaré-Prey gradient is an approximate value highly dependent on the crustal density in the vicinity of P_i.

The geopotential number P_i is calculated as follows:

$$C_i = \sum_{k=1}^{n} \bar{g}_k \delta\ell_k \tag{2.26}$$

where k denotes the levelling segment of measured height difference $\delta\ell_k$, and $\bar{g}_k$ is the mean observed surface gravity within the levelling segment.

The above levelling process is costly and time consuming, especially so, if gravity and height differences must be observed to get the orthometric height of a point. The geoid provides a cheaper, more efficient alternative to levelling by mathematically relating the geodetic height observed by GPS to orthometric height. Figure 2-9 shows the relationship between the two heights and the geoid.

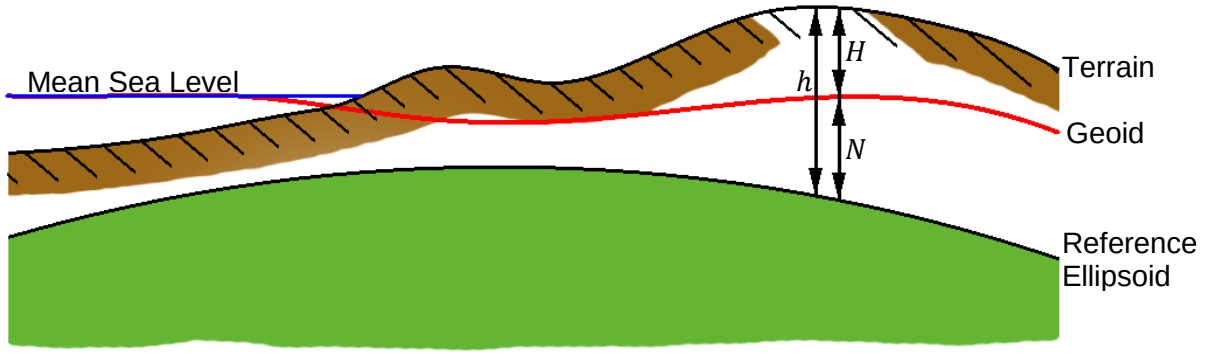

Figure 2-9. Height systems. *The geodetic height h is the height of a point above the reference ellipsoid. It is also known as ellipsoidal or GPS height. The orthometric height H of a point is the distance along the gravity plumbline from the geoid to the point. The geoid undulation N relates the two together; it is calculated as a deviation from a reference ellipsoid.*

If h and N refer to the same reference ellipsoid, their relation to H can be expressed below in Equation (2.27).

$$h = H + N \tag{2.27}$$

This allows for the orthometric height of a point to be determined without spirit levelling, if the geodetic height and geoid undulation is known, and can even be used to calculate ΔH between two points using differential GPS.

2.10 The "frequency" of a surface

Direct observations of Earth's gravity are discrete measurements of Earth's continuous gravity field. Depending on the altitude of the observations, different spatial variabilities of the field can be characterized. This spatial variability can be likened to the frequency of a sine or cosine wave. A high frequency sine wave will have many more repetitions over the same time period than that of a lower frequency. Figure 2-10 shows a comparison between surfaces with a low spatial frequency (variability) and a high spatial frequency.

In the case of gravity observations, the higher aerial density of the points and the closer to the Earth's surface the observation points are, the higher the frequency of the gravity anomalies, a direct result of the $1/r^2$ term in Newton's law of gravitation. As the distance between the observation point and the Earth increases, r^2 will increase exponentially with a power of 2. Since the difference between a small mass and a large mass will never increase exponentially, the r^2 term will always grow faster. This means that the further away from the potential source

the measurements are taken, the more uniform the potential will appear as the effects from masses merge together. For example, the Earth's gravity field will appear uniform if measured from the surface of Mars as r increases, and will be highly dependent on terrain if measured on the surface of Earth as r decreases.

Spatially, terrestrial gravity observations exhibit the higher frequencies of the Earth's gravity field, characterizing the rapid transitions between gravity values over shorter distances. Airborne measurements characterize the medium frequency components of the gravity field and will also show the general trends present in the field over much longer distances than the terrestrial data. Finally, satellite observations characterize the low frequency components of the field, and show trends present on a global scale.

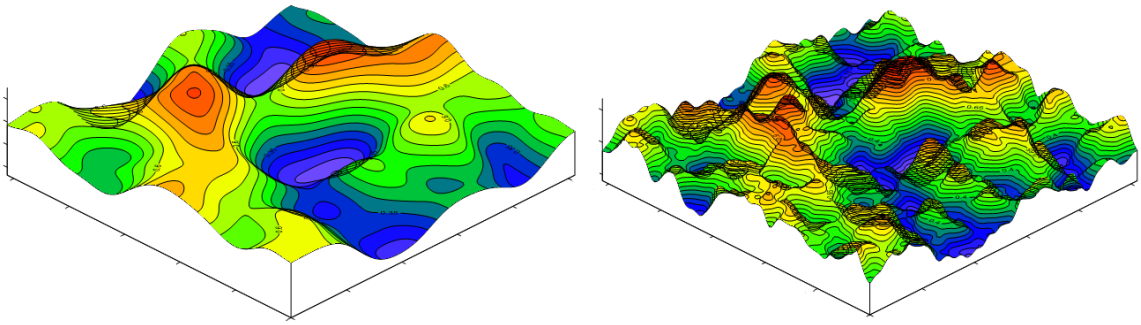

Figure 2-10. Low frequency (left) versus high frequency (right) datasets.

2.11 Oman Gravity Base Network (OBGN)

The Oman Gravity Base Network (OGBN) is composed of 39 ground gravity base stations, two of which were determined using absolute gravimetry in 1993 (Liard & Gagnon, 1993). The two stations are located in Rustaq and Sayq, and were used in 1994 as reference (base) stations for tying in the remainder of the base stations to the International Absolute Gravity Base Network (IAGBN) at epoch 1993. Figure 2-11 shows the currently established gravity base network.

Before the establishment of the OBGN in 1994, Oman's gravity datum was defined using the International Gravity Standardization Network of 1971 (IGSN71); so any gravity measurements taken before the OBGN readjustment in 1994 refer to a different gravity datum, and are not fully compatible with newer gravity measurements (Ravaout, 1996).

The gravity stations were adjusted for the last time in May 1996; both absolute reference stations were kept fixed, and the resultant gravity network is compatible with IAGBN at epoch

1993. Metadata and least squares adjustment models, pertaining to the network adjustment, are not available; only station locations and descriptions are present in the dataset.

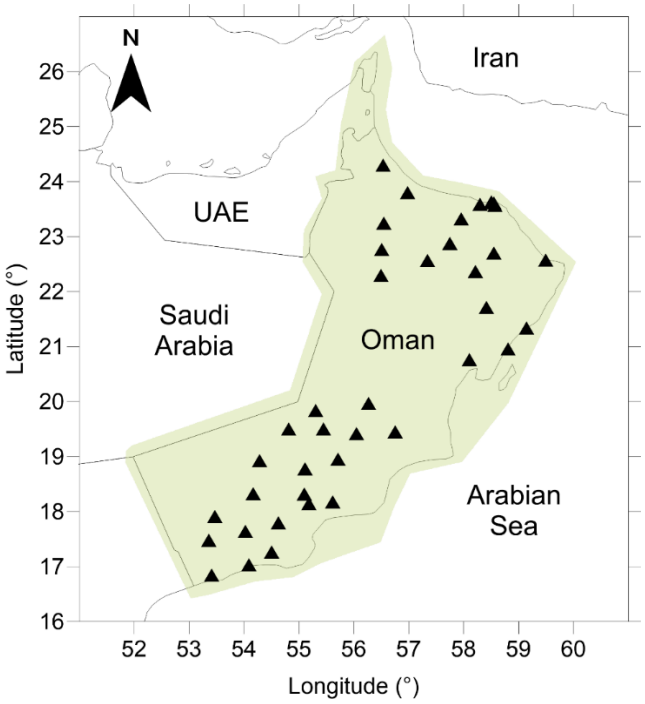

Figure 2-11. Oman gravity base network. *The Black Triangles represent the 39 first order benchmarks that make up the Oman Gravity Base Network.*

2.12 Geoid computation in practice

The standard computation practice to determine the geoid is the remove-compute-restore (RCR) method (Sansó, 1994). The primary concern in the computations is the presence of topographic masses above the geoid that need to be dealt with to remain consistent with the second rule of the Stokes integral. The method used in this thesis is the residual terrain model (RTM) method. First, topographic masses are approximated by a low frequency topography surface whose gravity effect is subtracted from the classical free air gravity anomalies Δg, creating residual anomalies. Further to the removal of the low frequency topography effect, a global geopotential model gravity effect on the free air gravity anomalies is also removed (Forsberg & Tscherning, 2008). The smooth reduced residual anomalies are now missing both the global characteristics of Earth's gravity field and the gravity effects from local low frequency topography. The computed residual anomalies are mostly composed of the gravity effects from the roughness of the remaining residual topography and are put through the Stokes integral to get their high frequency geoid equivalent (Forsberg, 1984). In the next step, both removed effects are converted

to their quasigeoid equivalents, and are then added back to get the quasigeoid. The geoid is then calculated from the quasigeoid by adding a correction that is a function of the simple Bouguer anomalies as described in the previous section, and in Heiskanen & Moritz (1967).

Sjöberg (2005) discusses the practical implementation of the remove-compute-restore method. In addition to describing the RCR method in detail, the paper discusses the approximations made when using it, and provides a few recommendations to increase the solution quality. The most important recommendation is that if residual anomalies were computed by removing the low frequency effects of a global geopotential model, they should be run through a modified stokes kernel with the same frequency effects removed.

The RCR method has been used in several large-scale geoid models, including the Andes Mountains (Tocho et al., 2005), the Baltic and Nordic region (Omang & Forsberg, 2000), Japan (Fukuda & Segawa, 1990), and the Konya Closed Basin in Turkey (Alpay Abbak et al., 2012).

The Andes geoid project was a preliminary analysis of a variety of gravity reduction techniques in preparation for the determination of a national Argentinian geoid. The area of interest of the study was the most rugged part of Argentina; therefore, whatever method worked best there, would be effective elsewhere in the country. The residual terrain model (RTM) (Forsberg, 1984), Rudzki's inversion, Airy-Heiskanen topographic-isostatic reduction, and Helmert's second condensation methods were examined (Heiskanen & Moritz, 1967; Bajracharya et al., 2001). Tocho et al. (2005) found that Rudzki's inversion method provided the best gravimetric geoid results with respect to the geometrically determined geoid; however, it is not a commonly used computation method due to its treatment of topography (Tocho et al., 2005). According to Heiskanen & Moritz (2006), although being conceptually important, the Rudzki reduction does not correspond to a geophysically meaningful model, and highly discourages its use in practice (Heiskanen & Moritz, 1967).

The Baltic and Nordic geoid was calculated using three separate terrain reduction techniques. The RTM (Forsberg, 1984), Helmert condensation (Heiskanen & Moritz, 1967), and a combination of the RTM and Helmert methods (Forsberg et al., 1996) were compared. All three methods were implemented using the RCR technique. The RTM method utilizes a very smooth reference surface, along with a roughness correction, to compute the terrain effects that are removed. The Helmert method does not remove masses; instead it shifts them down to the geoid using the same roughness correction as the RTM method, resulting in Faye anomalies. The indirect effect on the gravity anomalies that occurs when masses are shifted is also compensated

for (Sideris & She, 1995), but is often small enough to neglect. The RTM/Helmert method removes the RTM terrain effect from the gravity anomalies, grids them, and then adds them back before applying the compute state of the RCR technique. The compute step was completed using the standard Stokes integral (see Equation (2.17)) implemented with FFT. Omang & Forsberg (2000) found that the RTM/Helmert combination produced slightly better results with respect to GPS-on-benchmarks. They concluded that this was most likely a result of gridding the smoothest RTM anomalies, and restoring the Faye anomalies to avoid linear approximations in the RTM method. The results were not applicable to this thesis or the computation of Oman's geoid. The advantage of gridding the smoothest gravity anomalies in the RTM/Helmert method had little relevance to the Oman project; the byproduct of merging the bias repaired ground gravity data and downward continued airborne measurements already resulted in pre-gridded data prior to the initiation of the RCR method. With respect to the pure Helmert method, the GRAVSOFT GCOMB function used by Omang & Forsberg (2000) to compute and apply the indirect effect was not adequately documented, and its results may be questionable.

The Japanese geoid project was an extension to a previously determined gravimetric geoid model (Ganeko, 1983), that was computed exclusively with the Stokes integral and gravity data. Fukada and Segawa (1990) suggest that with the advent of satellite altimetry and new terrestrial gravity measurements, an improved geoid is possible. Their paper detailed the steps taken to compute the geoid using multiple combinations of terrestrially observed gravity and satellite altimeter data: gravity data only, altimeter data only, gravity data augmented with altimeter data, and altimeter data augmented with gravity data. The RCR method was implemented to calculate the geoid for each case. In the remove step, the effects of the terrain were calculated using the RTM method, due to topographic data being more reliable than crustal information required by other methods, as noted by Fukada and Segawa (1990). Instead of using the Stokes integral on the resulting residual anomalies, least squares collocation was used to estimate their geoidal effects. Fukada and Segawa (1990) found that using terrestrial gravity with altimeter data in places where gravity data were not available provided the most reliable geoid solution. The least squares collocation method optimally determines the value of the geoid at each point based on nearby observation points using a covariance function. This method will not work for Oman, because an optimal least squares solution requires the observations to have no systematic biases; Oman's ground gravity data will always have small biases, even after repair. In addition, the empirical covariance function is often difficult to determine and requires properly referenced unbiased gravity data; which is not available.

Lastly, the Turkish Konya Closed Basin geoid was computed as a way to compare the RCR method and the stochastic KTH method (Alpay Abbak et al., 2012). The KTH method utilizes a least squares stochastic modification of the Stokes integral by taking into account errors present in the GGM and terrestrial data, and applies additional additive corrections related to: topographic corrections, indirect effects, downward continuation effects, and atmospheric effects (Sjöberg, 1984, 1991, 2003) . Alpay Abbak et al., (2012) found that for mountainous regions with limited terrestrial observations, the KTH method had an absolute accuracy that was 3 centimeters better than the RCR method (Alpay Abbak et al., 2012). By merging the limited terrestrial observations in mountainous regions with comprehensive airborne measurements, the final Oman dataset will adequately characterize the gravity field in mountains, eliminating the need for the KTH method. In addition, the least squares component of the KTH method requires a-priori estimations of the errors of the gravity data, which were not rigorously provided in the initial Oman gravity dataset, and would require approximate estimation.

The RTM method (Forsberg, 1984) was chosen in this research for the remove step of the process, as it is the simplest conceptually to compute. Most importantly, it is highly dependent on terrain, making it easily computable and verifiable when a digital terrain model (DTM) is available. In addition, the RTM method requires a digital terrain model to compute, and topographic data are more reliably acquired than Earth's other crustal information (Fukuda & Segawa, 1990).

2.13 Summary

This chapter introduced several fundamental concepts that are essential to presenting the rest of the thesis. First, the geodetic boundary value problems and their application to geodesy were discussed. The concept of a level surface, anomalous potential, gravity anomalies, the fundamental equation of physical geodesy, and their relations to each other, were presented and discussed. The mathematically defined physical surface, the geoid, and the mathematical surface, the quasigeoid, were described. The surveying technique of spirit levelling, and the application of the geoid as an alternative were presented. The idea of the "frequency" of a surface was explained and the current state of the Oman Gravity Base Network was explored. Finally, detailed descriptions and comparisons of the methods currently used to calculate the geoid in other countries were provided, in an effort to determine the optimal technique best suited for the ONGM project.

3 Ground gravity repair

3.1 The Oman gravity dataset

The Oman gravity dataset contains the bulk of Oman's ground gravity observations. It consists of 229 298 observation points separated over 82 survey lines, shown in Figure 3-1. The average point density is one observation per 1.35 km^2.

Some lines appear to be an amalgamation of several gravity surveys taken for different purposes, while other measurement campaigns appear to have been artificially split into multiple lines. The large vertical green block of gravity points running through the center of the country in Figure 3-1 likely depicts a combination of exploration and gravity observation surveys, while several other multicolored areas are separated unnaturally, possibly corresponding to the various districts of Oman, or the border between UTM zones 39 and 40.

The arbitrary grouping of observation points into survey lines, illustrated in Figure 3-1, and the lack of additional information about them made finding critical metadata about the ground observation points difficult.

A thorough examination of the available technical reports and survey documents did not provide any additional information. In particular, the following important pieces of metadata pertaining to the gravity data necessary to compute the geoid were not found:

1.) Information pertaining to the national gravity network each line or observation refers to.
2.) Specific information about the reduction methods used to compute the provided gravity anomalies, primarily the density used in the Bouguer reduction, and whether the terrain roughness effect was removed from the gravity observations.
3.) Explicit information on the type of height provided; how it was acquired, and its accuracy.
4.) Information pertaining to how each Bouguer anomaly column of the provided gravity dataset was calculated.

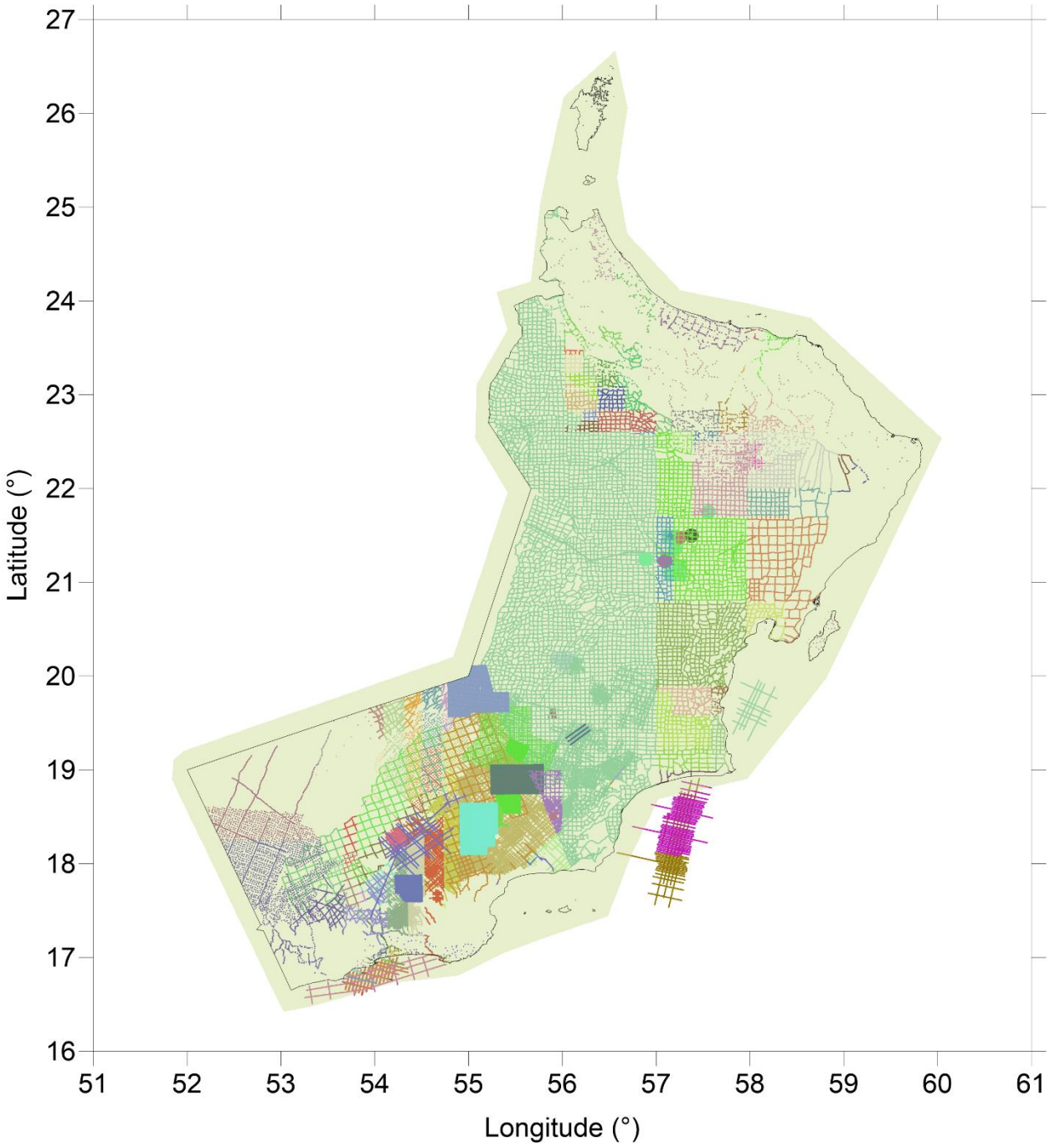

Figure 3-1. Map of legacy Oman ground gravity dataset. *Each color represents one of the 82 "survey" lines denoted in the initial ground gravity dataset. Some lines appear to be an amalgamation of several observation campaigns, namely the large vertical green block of gravity points running through the center of the country. Not included are the ~6000 new points observed in 2015.*

In addition to the lack of metadata, the actual data were incomplete and not in an adequate form to calculate the geoid. The list below briefly outlines where the gravity dataset was deficient, and the steps required to make it usable. A more detailed explanation is provided in the chapters and sections that follow.

1.) The observation points were given as Eastings and Northings in Oman's PDO Survey Datum of 93 (PSD93), and were converted to Latitude and Longitude in the WGS84 system.
2.) Not all observation points came with a height value, additionally, it was unknown whether the supplied heights were orthometric heights, and whether they referred to the correct global geopotential model. The heights for all points were taken from a consistent source with known properties and accuracies, such as NASA's Shuttle Radar Topography Mission (SRTM) model.
3.) Not all observation points came with the observed gravity value g. While all observation points came with some form of Bouguer anomaly (e.g., BOUGUER_26), it was not clear how it was calculated, i.e., what crustal density was used in the calculations. The observed g was inversely computed from the supplied gravity anomalies.
4.) New gravity observations taken for the purpose of this project were merged with the legacy ground gravity dataset.
5.) Free air and simple Bouguer anomalies were calculated from observed gravity at each observation point using a consistent formula.
6.) The free air and Bouguer anomalies were adjusted on a line-by-line basis to remove the sizeable biases arising from reference points of arbitrary gravity value. This bias repair was done using the medium frequency airborne gravity dataset. After the bias shifts, observation lines that still contained large outliers were also removed.
7.) To apply the Stokes integral, the bias shifted gravity anomalies were gridded. They were converted to complete Bouguer anomalies to be as smooth as possible, and then were gridded and converted back to free air anomalies.
8.) The medium frequency airborne gravity data and the high frequency ground gravity data were combined into one dataset with minimal frequency overlap between the two. This was done by low-pass filtering of the airborne data with an isometric Gaussian filter, and high-pass filtering the ground data using the inverse of the same filter; then adding the medium and high frequency components together.

3.2 Coordinate transformation from PSD93 to WGS84

The Oman gravity dataset is transformed from the PSD93 datum to the WGS84 datum. This process involves transforming from the non-geocentric Clarke 1880 ellipsoid to the geocentric WGS84 ellipsoid. First, the gravity survey points are transformed from UTM Zone 40 Easting and Northing coordinates to an (XYZ) Cartesian coordinate system with respect to the Clarke 1880 ellipsoid. Then the coordinates are transferred to the (XYZ) Cartesian coordinate system associated with the WGS84 ellipsoid using a seven parameter transformation. Table 3-1 describes the transformation parameters found in a report provided by Oman's National Survey Authority (NSA) (NSA, 1993).

Table 3-1. PSD93 to WGS84 transformation parameters

From	**To**	**Transformation Parameters**						
		Scale Factor	**Rotation Factors**			**Translation Factors**		
PSD93	**WGS84**	$\boldsymbol{\delta S\ (ppm)}$	$\boldsymbol{R_x}$(")	$\boldsymbol{R_y}$ (")	$\boldsymbol{R_z}$ (")	$\boldsymbol{\Delta x\ (m)}$	$\boldsymbol{\Delta y\ (m)}$	$\boldsymbol{\Delta z\ (m)}$
(XYZ)	*(XYZ)*	*+16.867*	*-0.616*	*-1.655*	*+8.378*	*-182.046*	*-225.604*	*+173.384*

Finally, the WGS84 (XYZ) coordinates are converted to geodetic latitude (ϕ) and longitude (λ) in the WGS84 system. The entire transformation process is carried out using the *pyproj.transform* method from the Python software package *pyproj* (Whitaker, 2016). A custom defined datum with parameters identical to the PSD93 datum is converted to the standard WGS84 datum (EPSG No. 4326). The custom paramaters for the pyprojProj object are given in Table 3-1:

Table 3-2. PSD93 pyproj paramaters

Projection String
"+proj= utm +a= 6378249.202 +rf= 293.466 +towgs84= -182.046, -225.604, 173.384, -0.616, -1.655, 8.378, 16.867 +zone= 40N +ellps= clrk80 +units= m"

This conversion is necessary to bring all the data to a common reference coordinate system. Geodetic latitude and longitude will allow the heights of the gravity points to be estimated from the SRTM, ensuring that a gridded gravity anomaly dataset will be spatially compatible with the EGM08 global geopotential model.

3.3 Standardization of observation point orthometric heights

To compute gravity anomalies of any type, the orthometric height of the computation point is required. The geodetic height observed with GPS relative to the reference ellipsoid is not sufficient because it is not measured with respect to the geoid.

Only about 54 percent of gravity observation points supplied included a corresponding height measurement, shown in red, in Figure 3-2. The technical and survey reports did not clarify the source of the provided heights (e.g. spirit levelling, GPS measurements, altimetry, scaling off a topographic map, etc.). Additionally, no height accuracy estimates were provided.

Ultimately, it will be better for long-term calculation consistency if all heights come from a single source with a known vertical datum and accuracy level. The source of heights chosen is NASA's Shuttle Radar Topography Mission (SRTM) (NASA, 2016), which refers to the geoid defined by the EGM96 (D/O 360) global geopotential model. The official absolute mean error of the SRTM is at the 16 meter level, but independent studies have put it in the range of 4-8 meters (Gorokhovich & Voustianiouk, 2006) with a standard deviation of $\pm$ 15-30m depending on the region and topography. This is sufficient for the ONGM project. The SRTM's datum is transformed from EGM96 (D/O 360) to EGM08 (D/O 2190) to make it consistent with the global geopotential model that will be used to calculate the geoid. Figure 3-3 illustrates the steps required to shift the EGM96 SRTM to EGM08.

Additionally, any negative and zero SRTM values corresponding to locations at or below sea level are replaced with values from the 30" $\times$ 30" General Bathymetric Chart of the Oceans (GEBCO) dataset (BODC, 2016).

Any subsequent calculations that require a Digital Terrain Model (DTM), are carried out by using various resampled spatial resolutions of the EGM08 shifted SRTM with bathymetry DTM. The Orthometric height of each gravity observation point is determined by nearest neighbor interpolation from a 3" (~100m) spatial resolution SRTM, which is a reasonable compromise between accuracy and complexity, as the resampled SRTM has a spatial resolution of nearly eight times the resolution of the ground gravity dataset. Figure 3-4 shows the SRTM dataset.

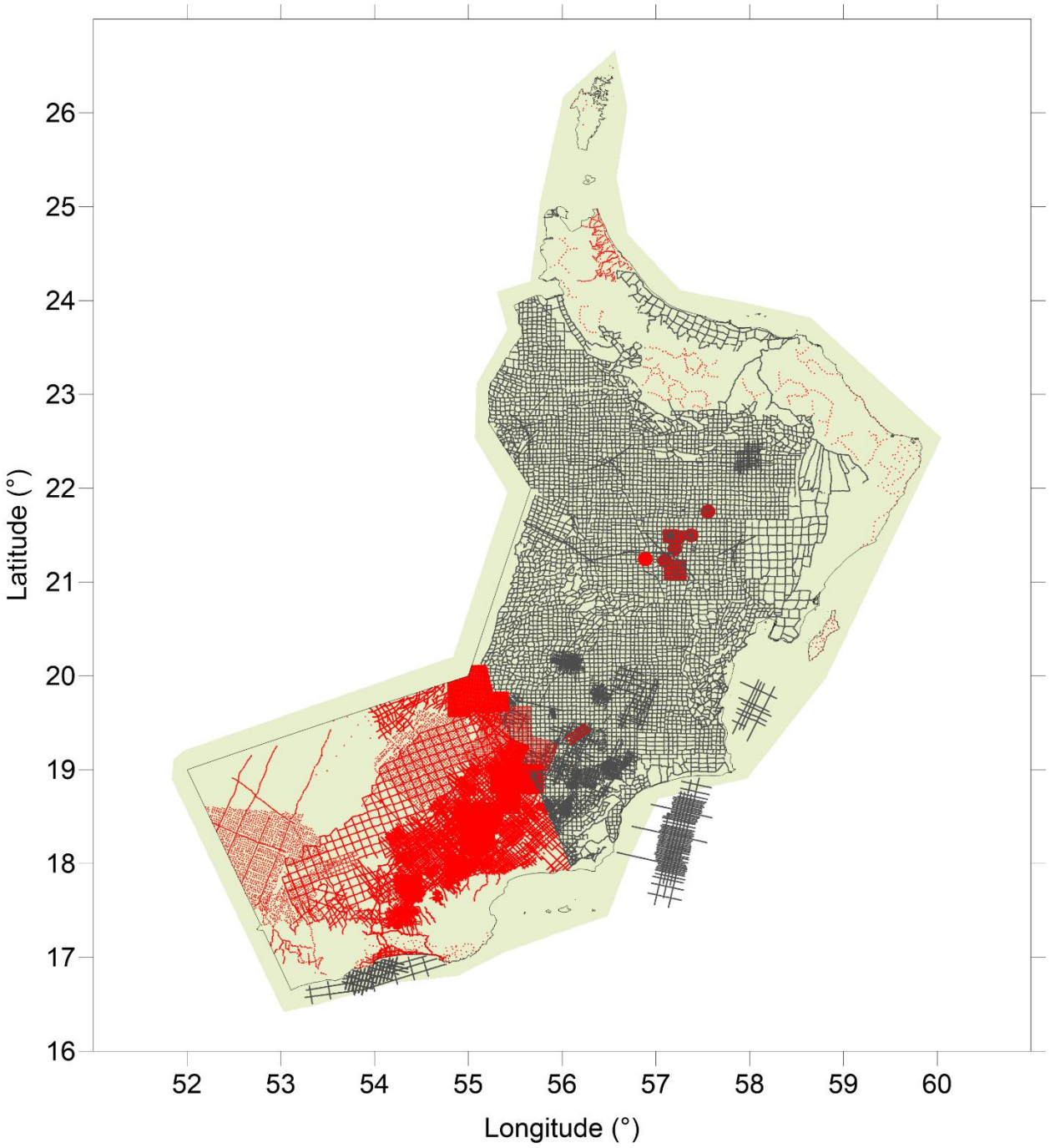

Figure 3-2. Ground gravity observation points with supplied elevation information. *The red points represent the observations with a supplied height. The concentrated red areas likely represent exploration surveys where knowledge of the elevation of the observation points would facilitate the application of the Bouguer correction.*

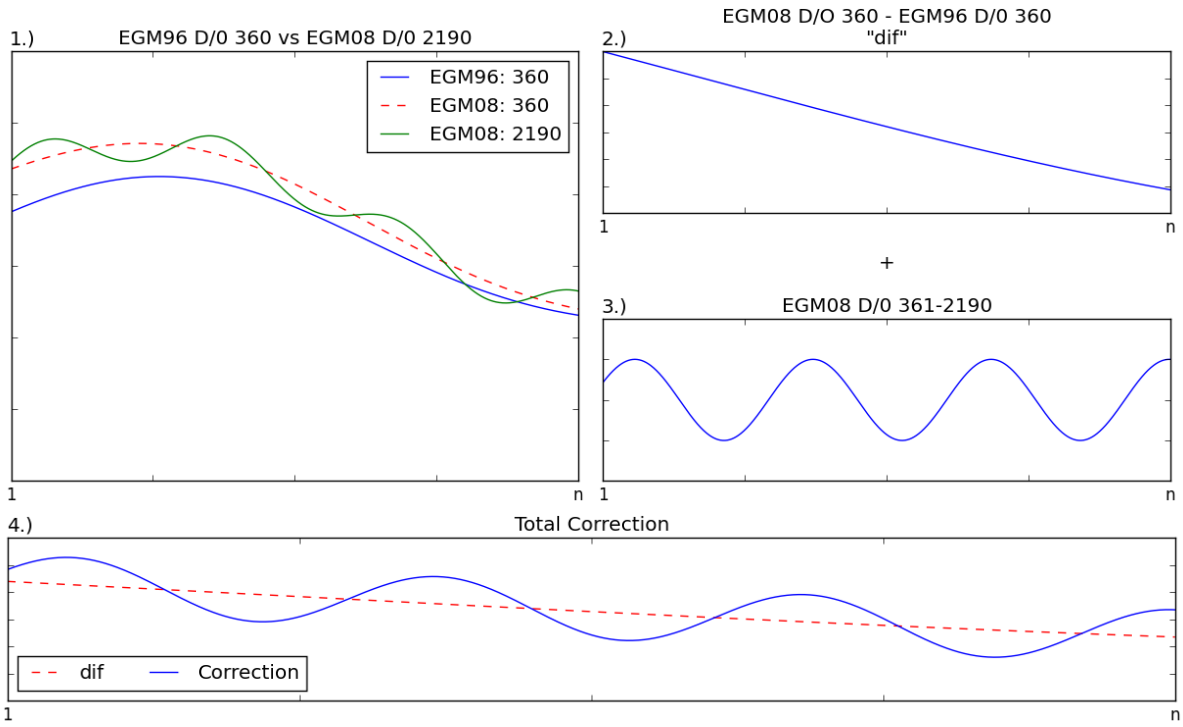

Figure 3-3. Illustration of datum shifting the SRTM dataset from EGM96 to EGM08. *Panel (1) Compute the EGM96 and EGM08 model geoid to EGM96's maximum degree and order of 360, represented by the blue and red dashed line in Panel 1 respectively, (2) Add their difference to the SRTM model to account for the datum difference up to degree and order 360. (3) Add the contribution of EGM08 from degree and order 361 to 2190 to the SRTM. This adds the additional effects of EGM08 not accounted for in EGM96. (4) Shows the complete total correction in blue, compared to the incomplete low order correction in dotted red.*

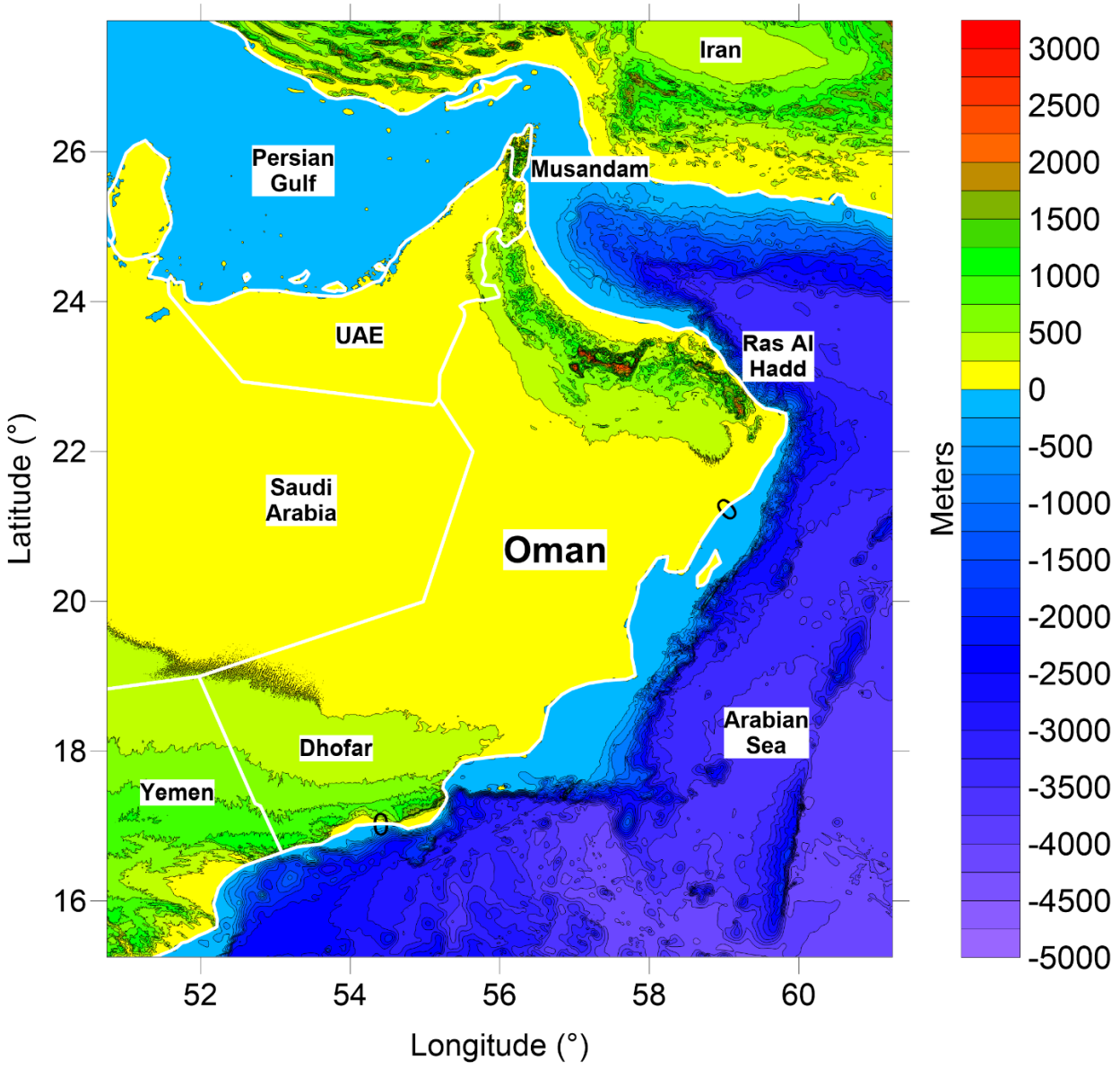

Figure 3-4. SRTM augmented with bathymetry dataset. *The dataset is the amalgamation of a 3" SRTM model resampled to 30" and a 30" GEBCO bathymetry model. The bathymetry is "draped" over the SRTM, where all zero and negative points in the SRTM are replaced with the equivalent point in the bathymetry.*

3.4 Inverse calculation of "observed" gravity

To ensure consistency between different gravity observation lines, all provided gravity anomalies are reduced to their "observed" values; that is, gravity g that would have been observed with a gravimeter at each data point on the surface of the Earth. First, the technical reports provided are reviewed to determine how each gravity anomaly in the legacy dataset was calculated. Due to the lack of information, an attempt is made to inversely convert the gravity

anomalies into gravity values that are subsequently compared with the observed g values only at the subset of points that come with such values. The differences are plotted in a histogram to visually verify if the transformation has been successful. Upon verification of the similarity of the histograms the transformation is then applied to all gravity points, regardless of origin, to generate a proxy of the observed gravity. This approach may introduce biases in certain survey lines due to the incorrect transformation. However, given that additional critical information is lacking, the additional biases are an acceptable compromise that is addressed later using airborne gravity anomalies.

The gravity dataset contains six different types of Bouguer anomalies labelled as “B26”, “Bme”, “B20”, “B23”, “B25”, “B28”. How each Bouguer anomaly was calculated is unknown, although it is suspected that the number in the label indicates the value of crustal density used. For instance, “B26” may indicate Bouguer gravity anomalies calculated with crustal density of $2.67\ g/cm^3$. Bouguer gravity anomaly “B26” is available for every observation point, so it is selected as a consistent basis to inversely calculate gravity. The general form of a simple or incomplete Bouguer gravity anomaly is given in Equation (2.19); however, substituting standard crustal density $\rho = 2.67 g/cm^3$ formulates Equation (3.1),

$$\Delta g_{BA} = g_G + 0.1967 H_P - \gamma_Q \tag{3.1}$$

where g_G is the observed gravity on the terrain point P that is being inversely computed, H_p is the orthometric height, and γ_Q is the normal gravity of the corresponding point Q on the reference ellipsoid. The numerical component of the second term corresponds to the Bouguer plate reduction gradient with standard crustal density plus the free air reduction from Equation (2.18).

In this study, the simple Bouguer anomaly is used rather than the complete Bouguer anomaly because no other information pertaining to which points received additional corrections was found. A Ministry of Petroleum and Minerals report (Ravaout, 1996), indicated that only observed gravity in the Musandam, Ras Al Hadd, and Dhofar mountainous regions received the roughness correction using an unknown DTM. However, as the numbers of the affected points, their exact location, and the value of the terrain corrections applied to them are unknown, no terrain reductions are applied to points in these areas.

The formula used to compute the normal gravity γ_Q for the inverse gravity computations is found in the same Ministry of Petroleum and Minerals report (Ravaout, 1996). It is concluded that the gravity anomalies provided in the legacy ground gravity dataset were most likely

calculated using the Geodetic Reference System 1967 (GRS67) gravity formula, which is shown in Equation (3.2)

$$\gamma_{GRS67} = 978031.846(1 + 0.005278895\, sin^2\, \phi + 0.000023462\, sin^4\, \phi) \quad (3.2)$$

where ϕ is the geodetic latitude of the desired point.

Further supporting this normal gravity formula is the fact that the Oman Gravity Base Network and its parent datum, the International IGSN71 gravity network, are fully compatible with the GRS67 gravity formula.

Before the inverse calculations are finalized, several tests are conducted using the available points with supplied observed gravity values. The two parameters of the inverse gravity calculation namely, the crustal density of the Bouguer plate and the Bouguer gravity anomaly column, were varied. Of the ~230 000 points, only about 25 percent (56 500) had measured gravity values. All of the observations were assumed to have been corrected for tides; it is standard practice in any gravity survey and it is highly unlikely they were not applied. They are mostly situated in the southern part of the country, with a few thousand in central Oman. The locations of the points can be seen in Figure 3-5.

Upon computing the inverse gravity values using Equations (3.1) and (3.2) for each point where observed gravity is provided, a histogram of the differences defined by Equation (3.3), is created.

$$\delta g = g_{Observed} - g_{inverse} \quad (3.3)$$

The purpose of this exercise is to determine whether the differences are small enough for the inverse computation to be valid for the rest of the gravity points using the same process. Figure 3-6 shows the initial histogram, which is bi-modally distributed. Each peak possibly corresponds to a survey(s) taken with respect to different gravity reference points. For easier viewing and decision-making, the two peaks are separated into two histograms and any visible outliers are removed, resulting in Figure 3-7 and Figure 3-8. The bin sizes of the three histograms were determined using $\lceil \sqrt{n} \rceil$, where n is the number of differences.

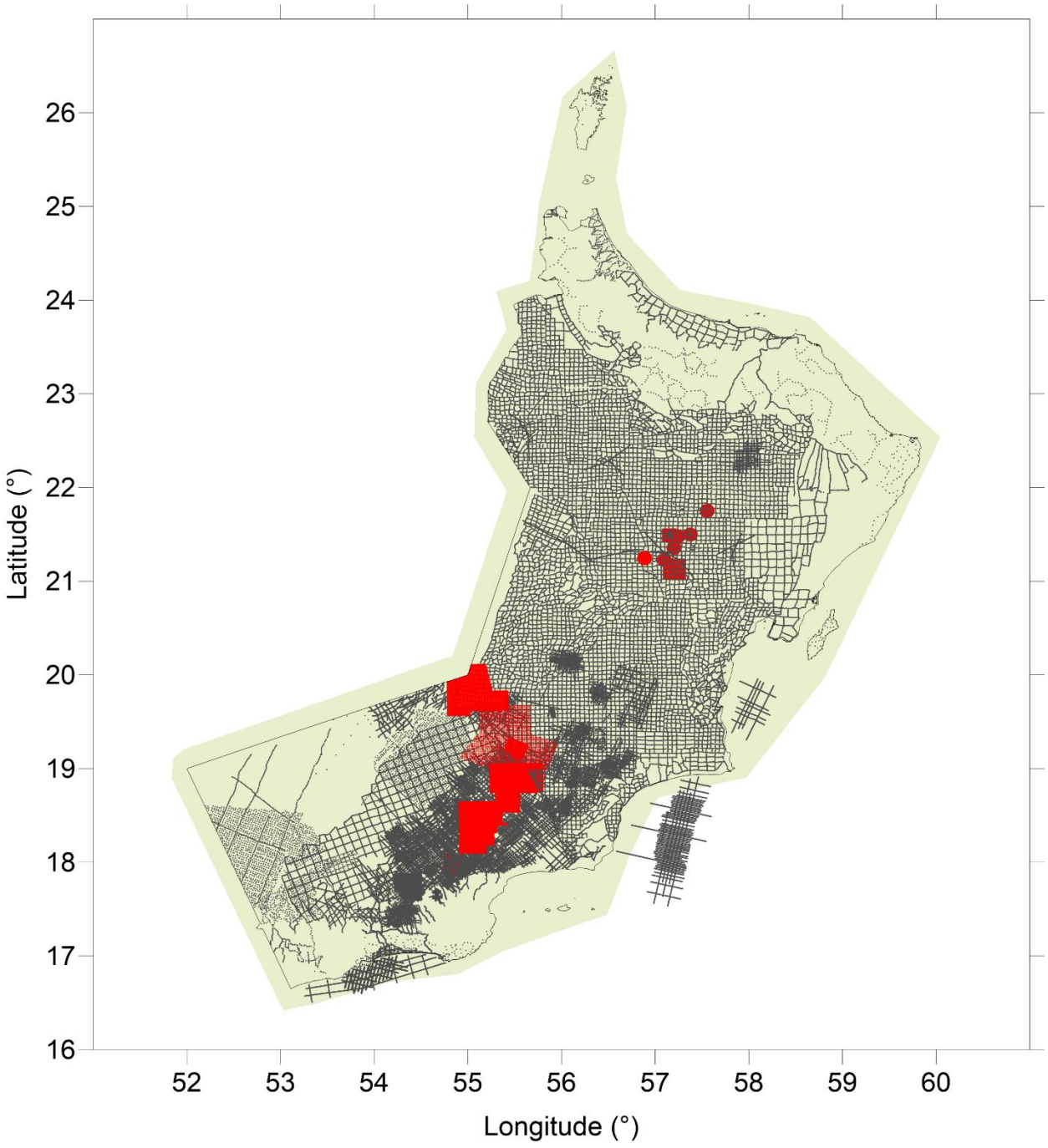

Figure 3-5. Ground gravity observation points with supplied observed gravity values. *The red points represent the observations that came with a supplied observed gravity (g) value. The concentrated red areas likely represent exploration surveys, where the gravity value was kept in addition to any number of Bouguer anomalies.*

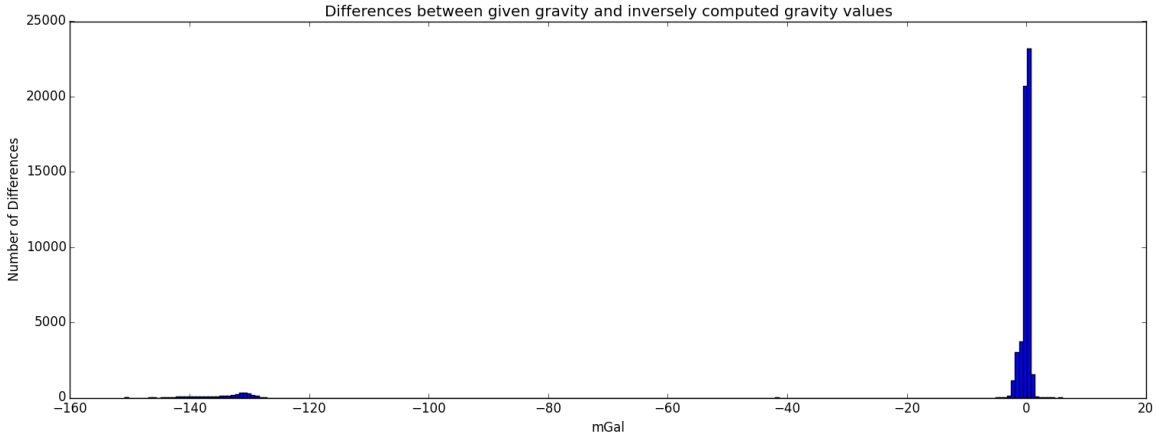

Figure 3-6. Differences between given gravity and inversely computed gravity values*. Two distinct peaks are present; the "shortness" of the left peak indicates that the outliers are probably part of one or two survey lines. The majority of differences are in the peak centered around 0 mGal. The mean of the dataset is -6.9 mGal and the standard deviation is 29.4 mGal, which are a direct result of the "outliers" present in the left peak.*

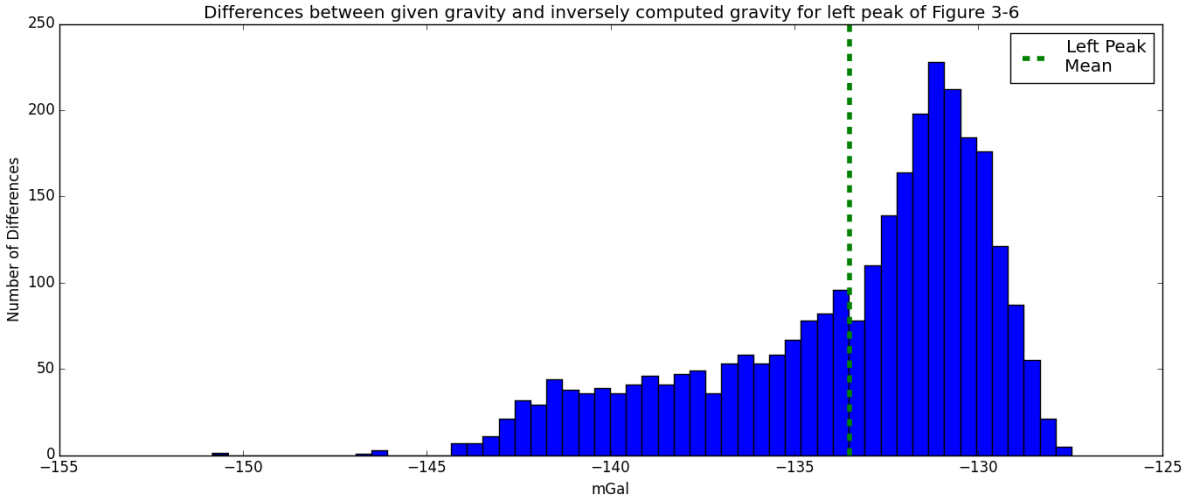

Figure 3-7. Differences between given gravity and inversely computed gravity for left peak of *Figure 3-6*. *The left peak is negatively skewed; the reason for this is unknown. The data is shifted by a -133.5 mGal bias that may have resulted from the use of a gravity benchmark with an arbitrary gravity value to tie the points, or the use of another unknown normal gravity value different from* γ_{GRS67}*. Regardless of the source, this bias issue is corrected in the following chapter. The standard deviation is* $\pm$ *3.82 mGal.*

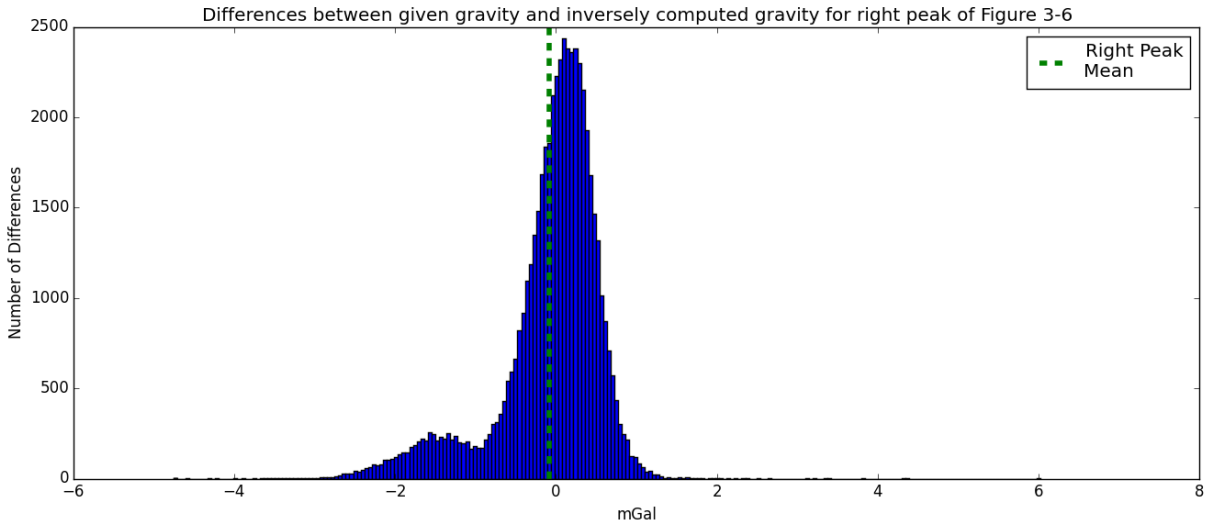

Figure 3-8. Differences between given gravity and inversely computed gravity for right peak of *Figure 3-6*. *The right peak appear to be normally distributed around -0.08 mGal with a standard deviation of* $\pm$ *0.65 mGal, but has a small bump around the -1.7 mGal mark. This bump is due to one or more survey lines that were slightly biased from an unknown source. Much like the points in Figure 3-7, the biases are compensated for in the following chapter. The majority of points that were supplied with gravity observations (52 671) lie within* $\pm 3\sigma$ *of the mean value, meaning the inverse calculation provides acceptable gravity values for 93.2 percent of the points.*

3.5 Augmenting of the old data with new gravity points

The 6506 new gravity points that were measured in 2015 (Géophysique GPR l'ntl Inc., 2015) need to be integrated to the inversely calculated gravity values computed in the previous section. The new points were observed in the mountainous and populous areas of the country to better characterize the regions where terrain would affect the measurements the most, and thus the resolution and accuracy of the geoid model where it would be used the most. The locations of the newly observed points relative to the legacy ground gravity dataset can be seen in Figure 3-9 (red dots).

To prevent the new gravity points from being obscured by possibly biased measurements present in the legacy ground gravity dataset, all legacy data points within 33" (~1000 km) of a newly observed point were removed. Approximately 4000 points were removed. The new gravity points were assigned four "survey lines" that can be used to separate them from the legacy dataset, where each line corresponds to a different observation location. The points can be seen in Figure 3-9.

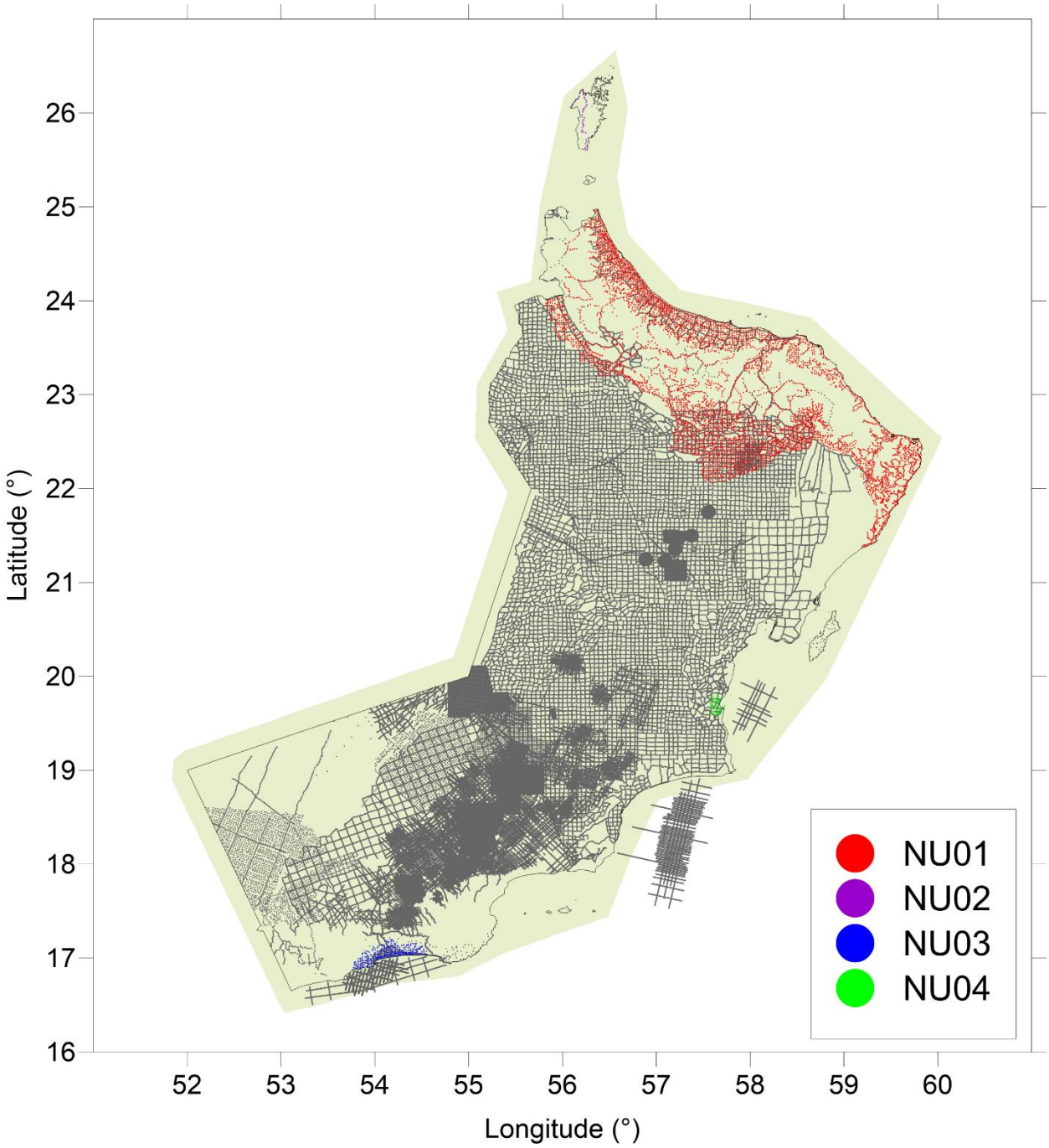

Figure 3-9. New gravity observation points with respect to the legacy dataset with no points removed. *The red points in the northern mountainous region (Al Hajar Mountains) are assigned line number NU01. The purple points in the separated northern part (Ruus al Jibal) are assigned line number NU02. The blue points in the southern part of the country (Salalah) are assigned line number NU03. The green points in the eastern part (Duqm) are assigned line number NU04. The 33" cutoff compliments the spacing of the final free air anomalies* $(30" \times 30")$.

3.6 Initial determinations of gravity anomalies

The next stage includes the computation of the two types of gravity anomalies required to calculate the geoid. The free air and simple Bouguer anomalies are calculated using the ground gravity dataset created in the previous two sections. This stage is initially conducted without taking into consideration the expected very large biases present in the ground gravity anomaly dataset. These biases will be addressed using an airborne gravity dataset in following chapter.

For the WGS84 ellipsoid, the normal gravity γ_Q can be calculated using Equation (3.4) (DMA, 1987)

$$\gamma_Q = 978032.67714 \, \frac{1 + 0.00193185138639 \sin^2 \phi}{\sqrt{1 - 0.0066943799901 \sin^2 \phi}} \, mGal \tag{3.4}$$

where, similarly to Equation (3.2), ϕ is the geodetic latitude of the computation point.

The initial calculations of the free air anomaly grid appears to exhibit severe biases in several locations. A plot of the biased free air anomalies can be seen in Figure 3-10. The largest biases are shaded purple and highlighted in the southern part of the country. They have a bias magnitude of about 90 mGal. Other biases exist elsewhere in the country but they are much smaller in scale (e.g. small area circled in white in the center of the country).

In addition to the biases, there are two other deficiencies present in the gridded free air gravity anomalies in Figure 3-10. Firstly, the gravity data exhibit traits that free air anomalies are not expected to have, such as the high frequency noise in the dashed white ellipse located in the northern part of the country. Secondly, the free air gravity anomalies do not characterize all the terrain features, even though they should be highly correlated to the terrain. The northern-most solid white circled area should have a similar shape to the part of the mountains that can be seen in the same area in Figure 3-4, but it does not.

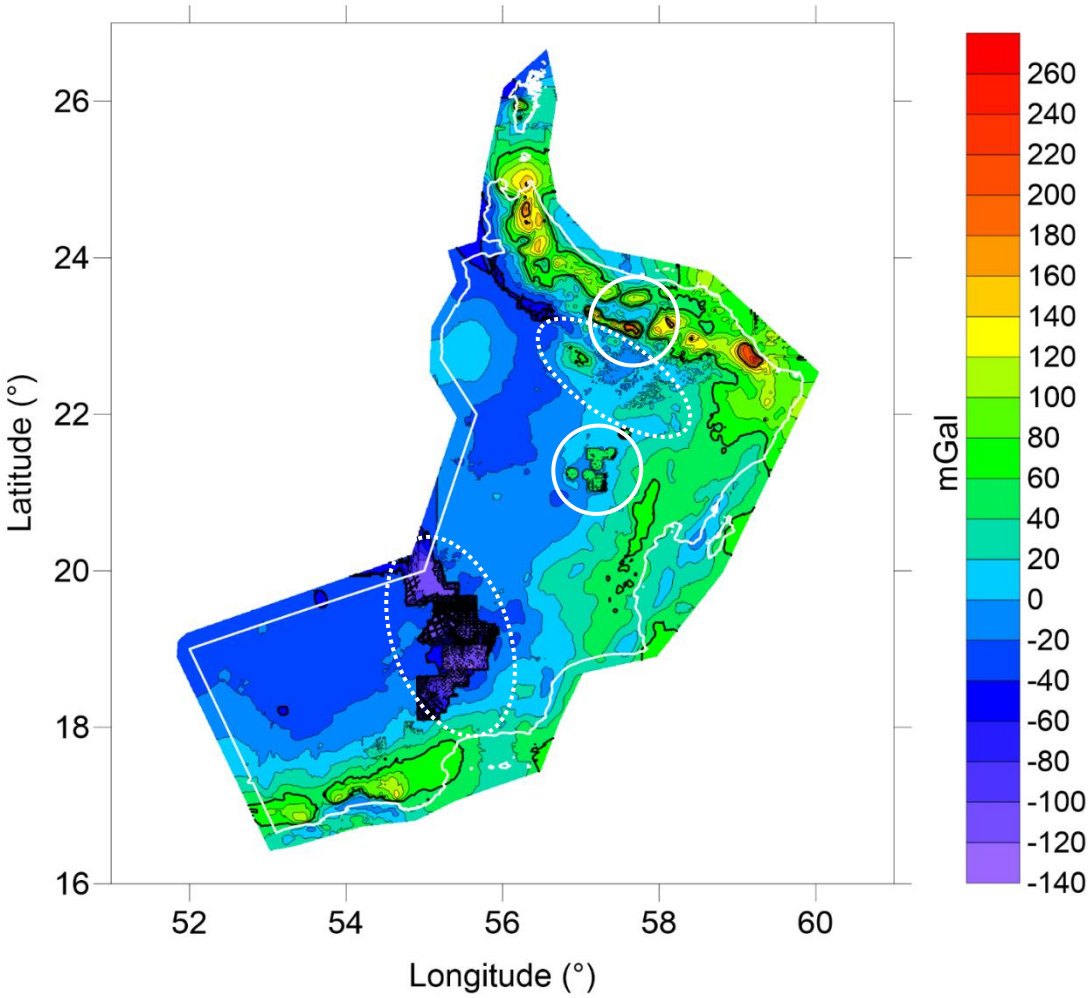

Figure 3-10. Original biased ground free air anomalies. *In general, any bias or error in the free air anomalies will negatively affect the quality of geoid and corrections need to be considered. Solutions specific to the inconsistencies highlighted in this diagram will be discussed in the following chapters.*

3.7 Summary

This chapter explained the steps taken to establish a preliminary ground gravity dataset from the legacy gravity dataset. Gravity anomalies were first transformed from the PSD93 UTM datum to the geodetic WGS84 datum. New orthometric elevations for each observation point were taken from the SRTM dataset that was datum shifted vertically from EGM96 to EGM08. Bouguer gravity anomalies taken form the legacy gravity dataset were used to inversely calculate "observed" gravity g, and the new gravity observation points from 2015 were integrated into the legacy gravity dataset. Free air gravity anomalies were computed for the entire gravity dataset; however, components of the gravity anomaly dataset were biased by up to about 90 mGal and will be repaired in the following chapter.

4 Ground gravity bias repair and gridding

Figure 3-10 shows several significant biases in the free air anomalies that are the result of inadequately computed inverse gravity values or arbitrarily referenced gravity measurements, due to the exploratory nature of the legacy gravity dataset. It was mostly populated from geophysical exploration surveys, where tying in gravity survey lines to the existing gravity network is not necessary. The lack of reference to a national gravity network means that each survey was internally consistent, but would be biased relative to surveys conducted elsewhere in the country.

Any biases present in the free air anomaly dataset, even small ones, would improperly bias the final geoid model. The biased lines could have been disregarded, but that would eliminate a large portion of valuable high frequency ground gravity data. Therefore, it is very important to reclaim as much of the problematic data as possible.

4.1 Ground gravity bias repair

The 82 original legacy survey lines and the four new additions are first split into 124 smaller segments where visible groupings of points existed. For example, one original survey line with discernable clusters of points in the northern and southern part of the country (cf., Figure 3-1) is split into two separate survey segments.

It is then postulated that the free air anomalies contained in each individual survey line and their equivalent interpolated free air anomalies from an alternate known reliable free air gravity dataset (e.g., airborne), from the same region, would have similarly shaped histograms offset by a bias value. This bias value would be equal to the difference in the simple mean of each dataset, given by Equation (4.1), and would be the offset in milligals required to un-bias the gravity anomalies.

$$bias = \mu_{known} - \mu_{biased} \tag{4.1}$$

The first order statistic μ is the only statistic that can be applied from the known dataset. The ground gravity dataset characterizes what is essentially an “infinite” frequency. It is the closest point to the center of mass of the Earth that gravity can be measured. Any other dataset, be it airborne, downward continued airborne, or satellite, cannot fully characterize the same

frequency in its histogram. Thus, the conventional image processing techniques of histogram equalization or histogram matching is not applicable; the two histograms will express different frequency components. Shifting the biased ground free air anomalies by the difference in histogram means is the extent of the bias repair that can be conducted without the introduction of additional frequency related biases.

The known gravity dataset that is used here for the repair of biases is the set of airborne free air gravity anomalies downward continued to the geoid. The downward continuation process adds additional higher frequency components to the medium frequency airborne gravity anomalies that are the best estimates of the anomalies determined from ground gravity observations. Note that the downward continuation of the airborne free air gravity anomalies is discussed extensively in the next chapter. The difference in the mean values between the two datasets in a region is used to un-bias the free air anomalies determined from ground gravity observations, hereafter called ground gravity anomalies.

For every point in each survey line, the downward continued airborne gravity anomaly is estimated using the nearest neighbor interpolation method. The histograms of the two sets of gravity anomalies (ground and airborne) are then plotted and their means are differenced. The histograms are used to check the similarity of the distributions before the difference of their mean is used to remove the bias from the gravity anomalies determined from ground observations.

Figure 4-1 illustrates an extreme case of bias, and the corresponding histograms for each are shown in Figure 4-2. Figure 4-3 shows a case in which bias shifting is not justifiable, along with the equivalent histograms in Figure 4-4. Figure 4-5 shows a histogram of all the biases that are computed for all survey lines, and Figure 4-6 shows each line with its bias.

The steps taken thus far do not fully eliminate all biases present on a line-to-line basis. Lines L4A and L4B are removed because they appear to be visibly biased even after being bias shifted (see Figure 4-9). A ground-to-airborne comparison plot and the associated histogram for each line is shown below (L4A: Figure 4-7, Figure 4-10, L4B: Figure 4-8, Figure 4-11). These lines are located in the oceans surrounding Oman and represent a portion of the seaborne gravity measurements available. The postulation about the similarity of the histograms of ground and airborne gravity anomalies is not valid in either survey lines' case. The cause for this issue is unknown, but it may have something to do with the surrounding terrain or the method of observation of the seaborne gravity measurements. Approximately 4000 points are removed altogether; representing less than 2 percent of the ground dataset.

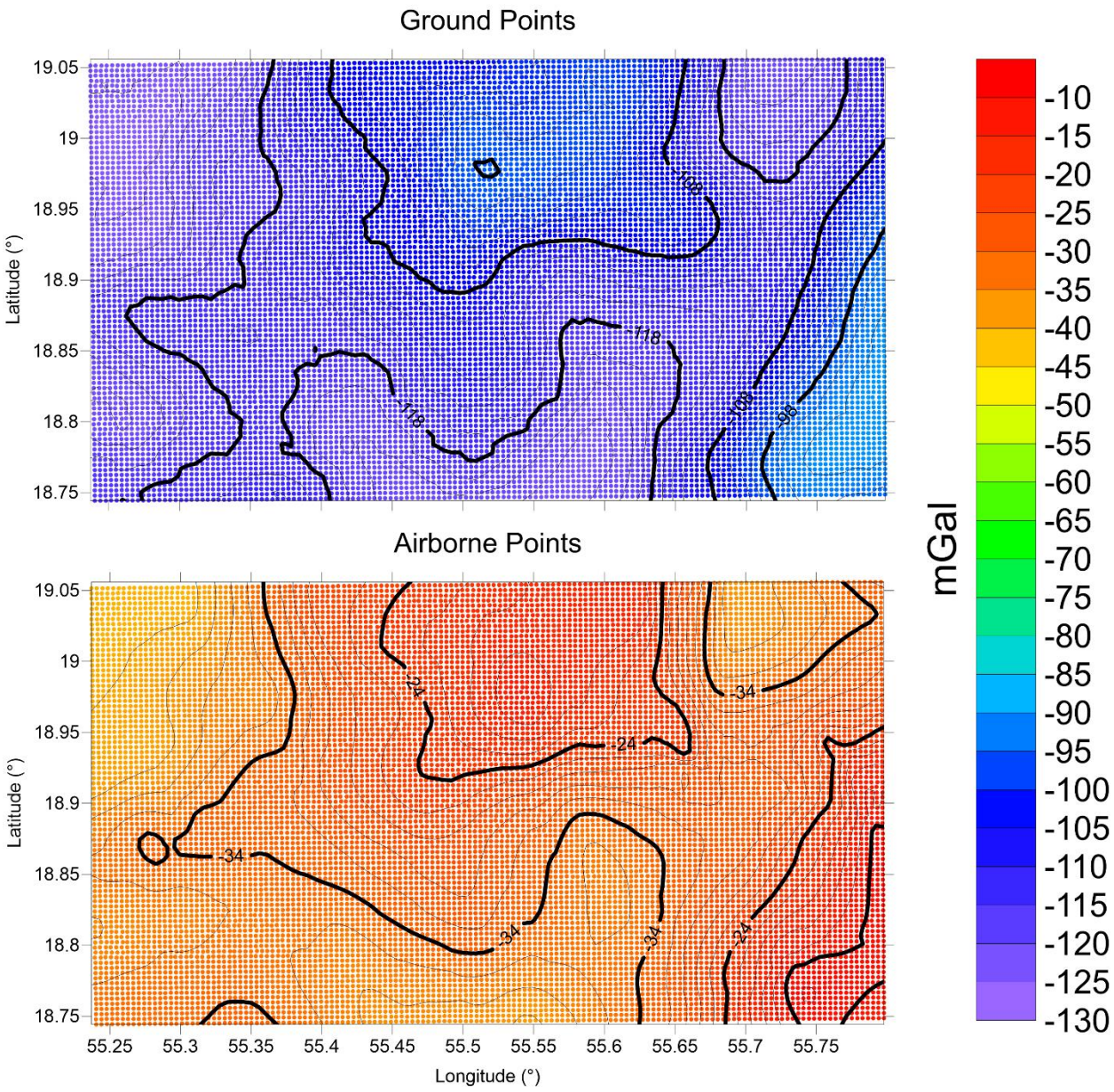

Figure 4-1. Comparison of ground gravity anomalies (upper panel) and their equivalent airborne gravity anomalies (lower panel) of survey points in Line L68 indicated by the colored dots. *The very densely spaced, almost grid like, ground gravity observations and their equivalent airborne points are completely different visually, but with closer inspection of the contours, the same general "shape" of the gravity anomalies is present in each. This supports the idea that the larger biases that appear in this example and several other "survey" lines in the southern part of the country are a result of poor referencing of an exploration survey to a gravity datum.*

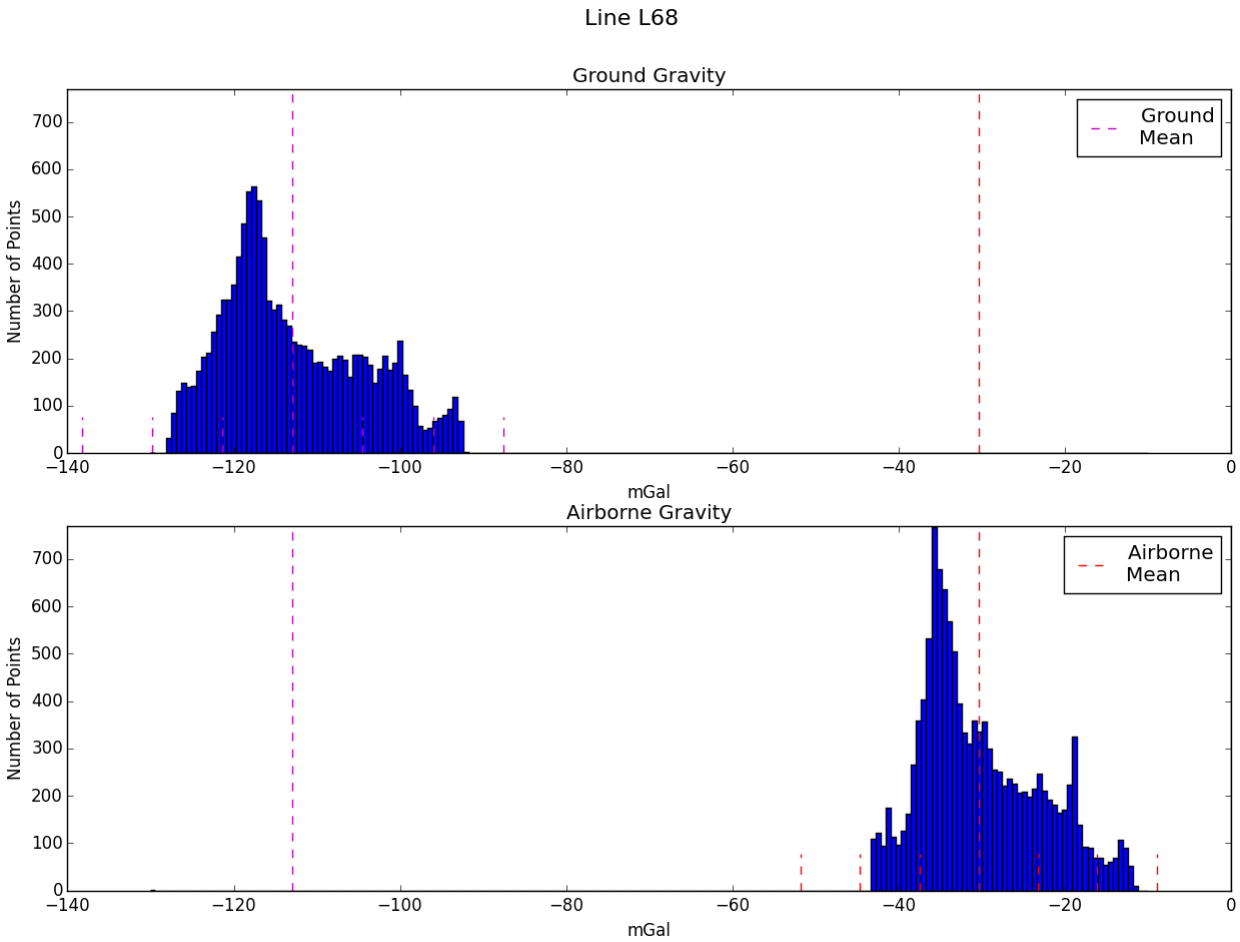

Figure 4-2. Histogram of ground gravity anomalies (upper panel) and their equivalent airborne gravity anomalies (lower panel) of survey points in Line L68. *The histograms are very similar, are positively skewed and have very similar variance and range. Their means however are offset by 80 mGal (bias).*

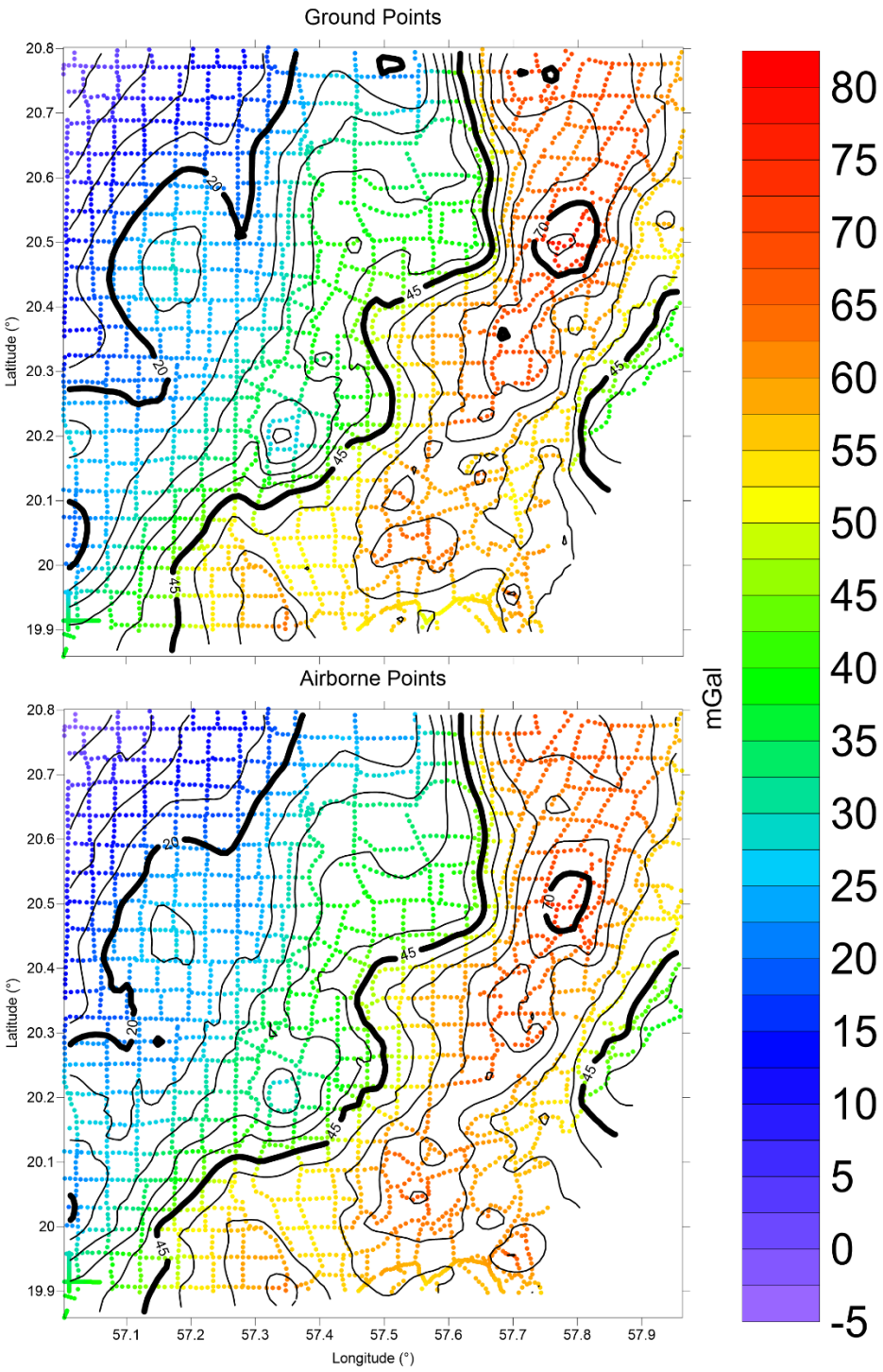

Figure 4-3. Comparison of ground gravity anomalies (upper panel) and their equivalent airborne gravity anomalies (lower panel) of survey points in Line L79 indicated by the colored dotes. *The ground line and the equivalent airborne line are extremely similar; they are probably referenced to the same gravity network. This was the normal case for very large "survey" lines, most of which were present in the northern part of the country. The grid pattern present in these larger observation lines suggests that they were not conducted for exploration surveys, and are more likely to be properly referenced to the national gravity network*

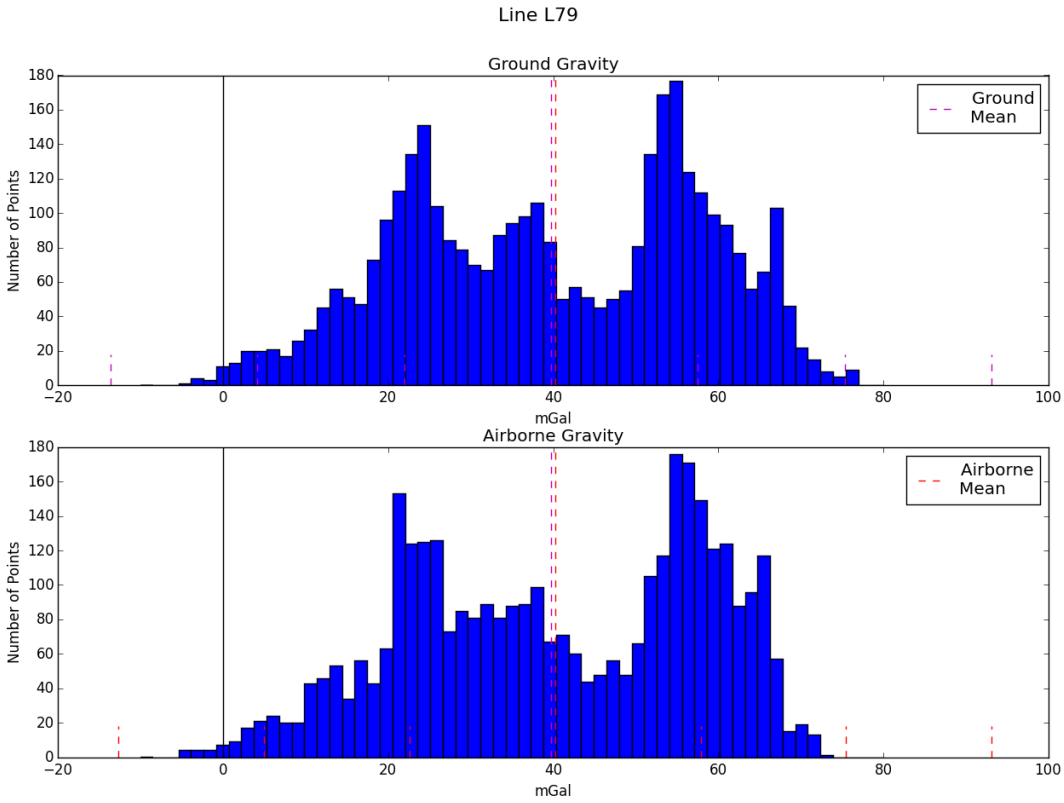

Figure 4-4. Histogram of ground gravity anomalies (upper panel) and their equivalent airborne gravity anomalies (lower panel) of survey points in Line L79. *The histograms are very similar, are bimodally distributed, have comparable peaks at similar locations, and nearly identical variance and range. The histograms and Figure 4-3 demonstrate that there is no bias of any kind, and the calculated bias is small enough to be negligible.*

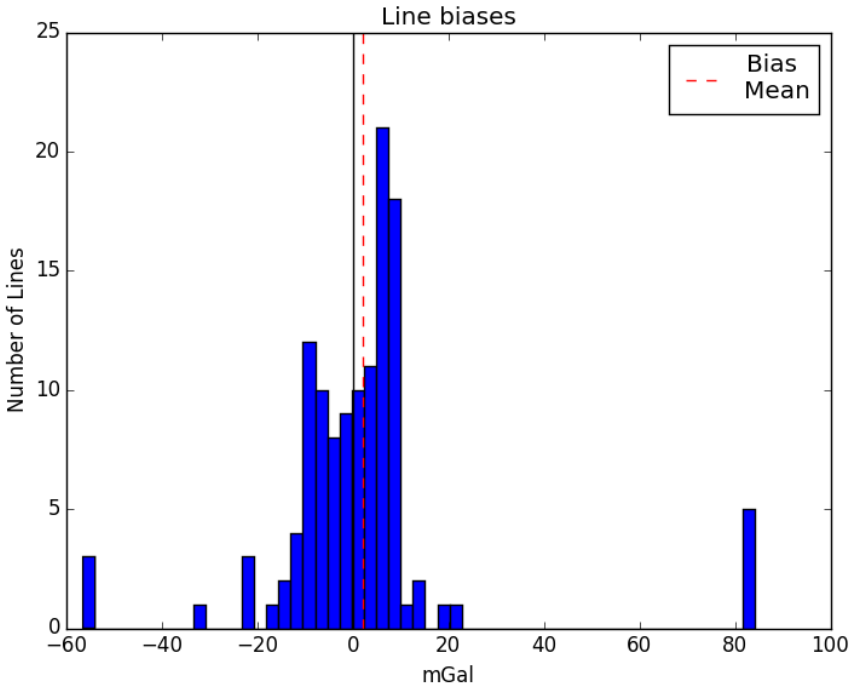

Figure 4-5. Histogram of all biases*. The mean of the biases is 2 mGal, and the majority of survey lines are within the -20 to 20 mGal region.*

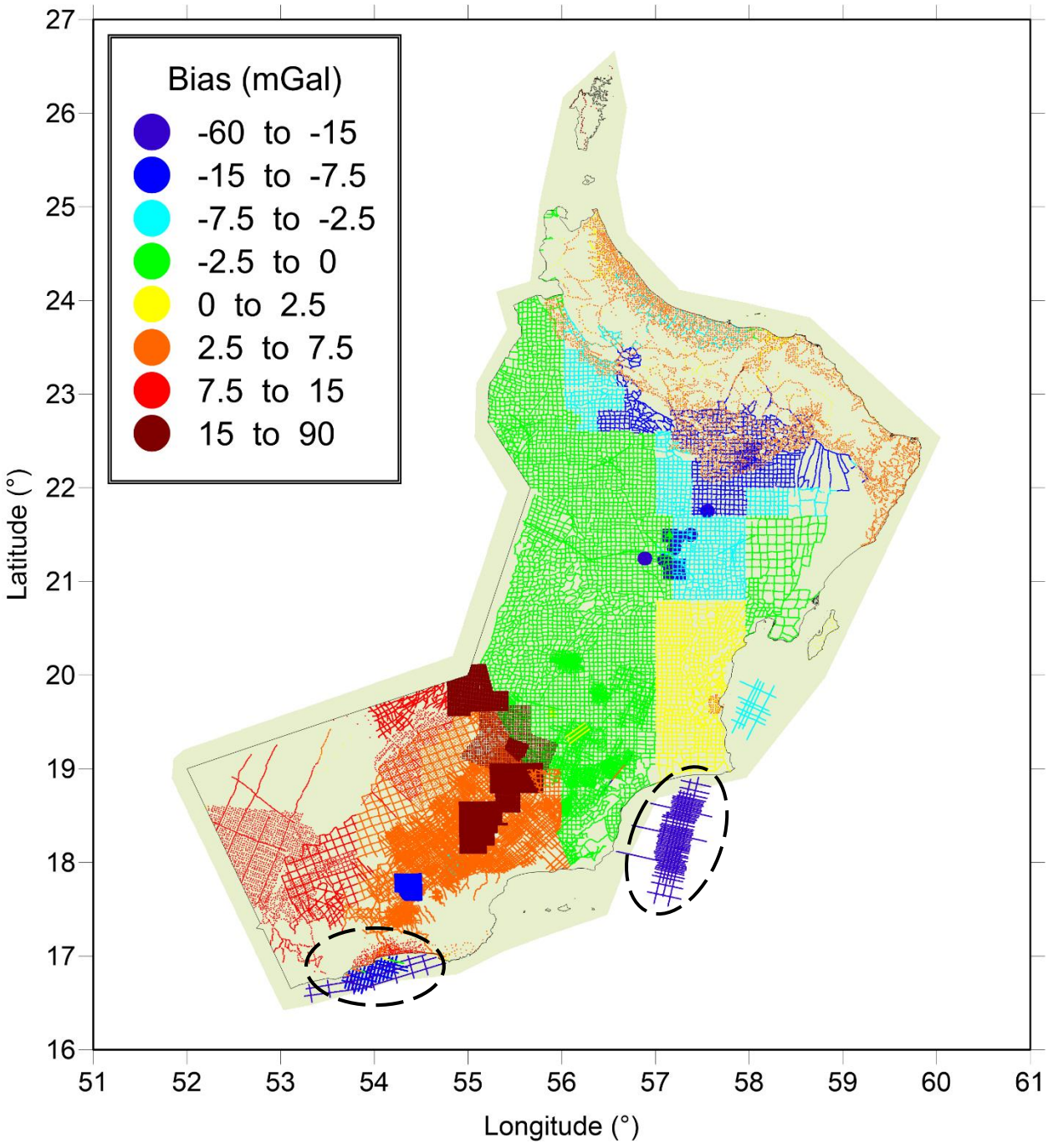

Figure 4-6. Color-coded biases of each ground survey line*. Part of the lines (L4A and L4B) circled in black were removed as outliers.*

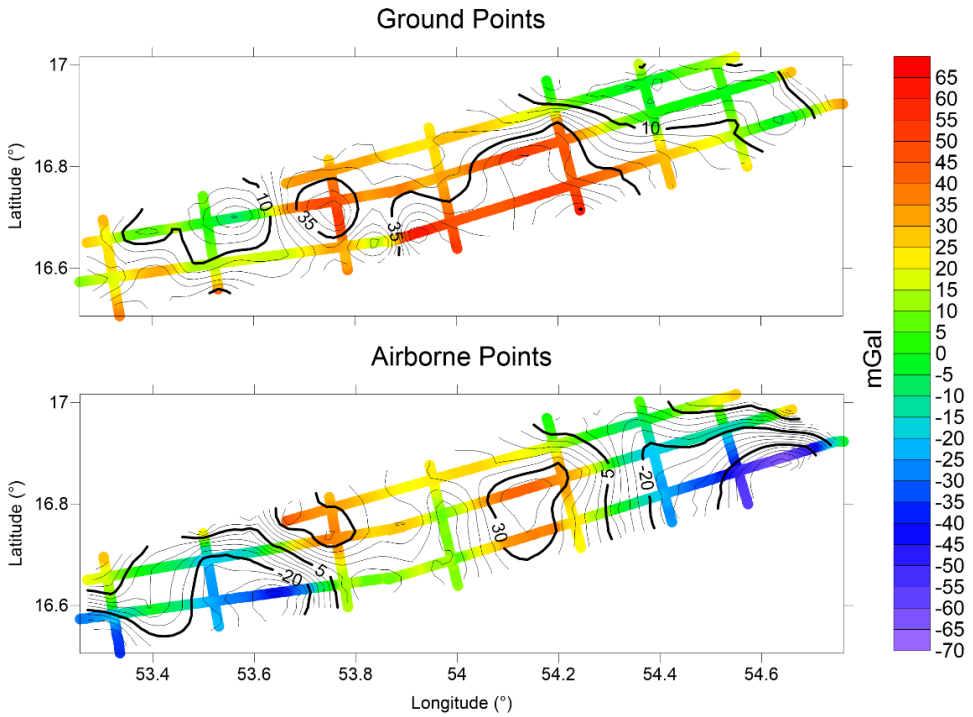

Figure 4-7. Comparison of ground gravity anomalies (upper panel) and their equivalent airborne gravity anomalies (lower panel) of survey points in Line L4A. *Unlike Figure 4-1 and Figure 4-3, there does not appear to be any visual correlation between the ground and airborne points. The distinctly different ground and airborne contours in each map also support this. There is no information on how or where the seaborne gravity was observed, whether it was filtered, etc.*

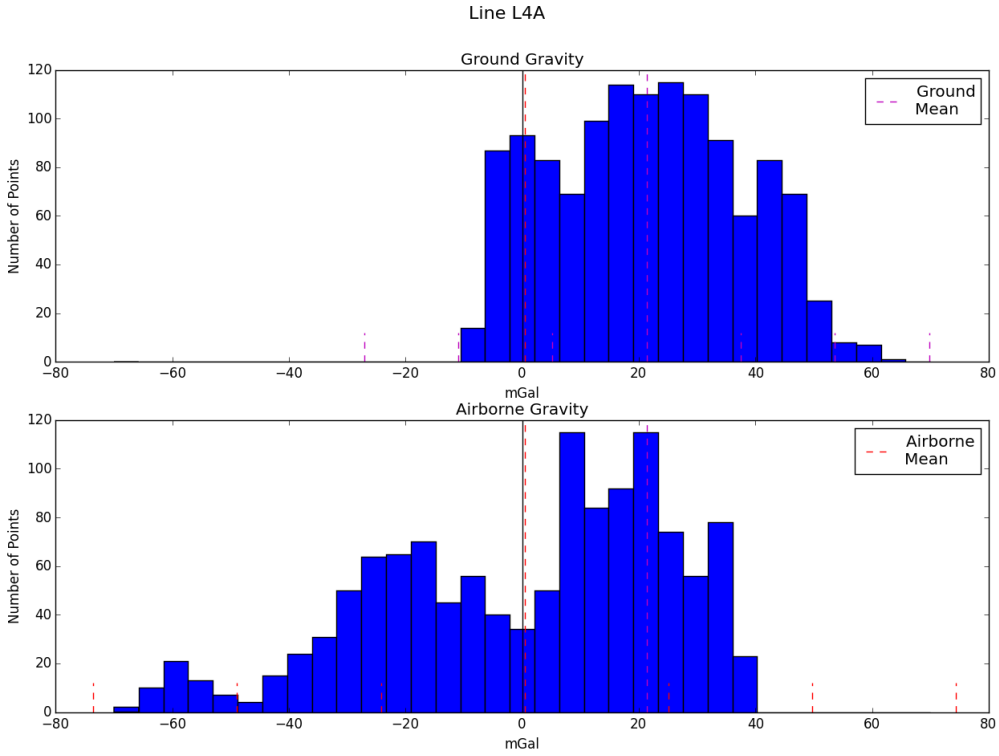

Figure 4-8. Histogram of ground gravity anomalies (upper panel) and equivalent airborne gravity anomalies (lower panel) of survey points in Line L4A. *The noticeable difference in histograms demonstrates that the initial postulation made to allow bias shifting is false in Line L4A.*

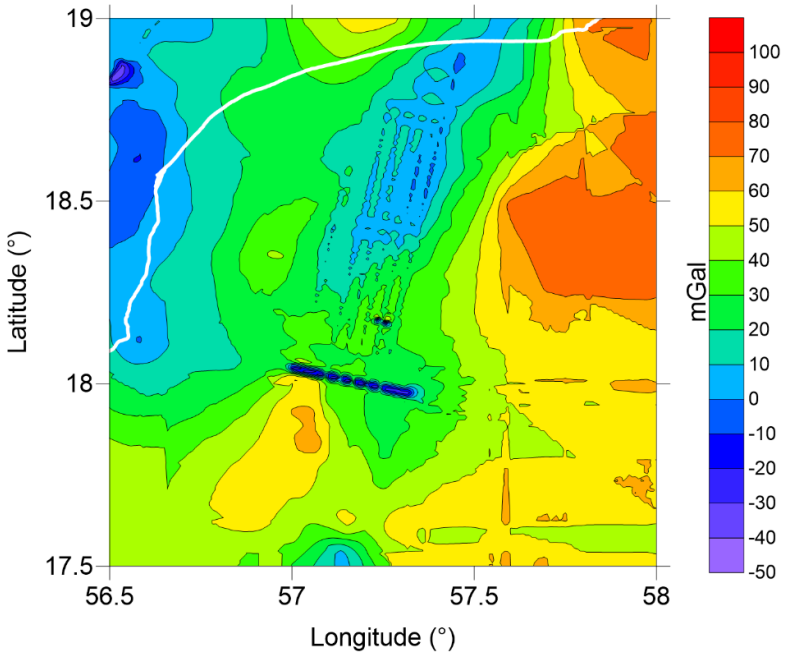

Figure 4-9. Example of the biases remaining in line L4B after bias repair. *The noticeable straight lines remaining after bias repair demonstrate that for this line in particular, bias shifting was not effective. The gridded gravity anomalies characterize features (e.g. "scratches") that cannot exist in earth's gravity field.*

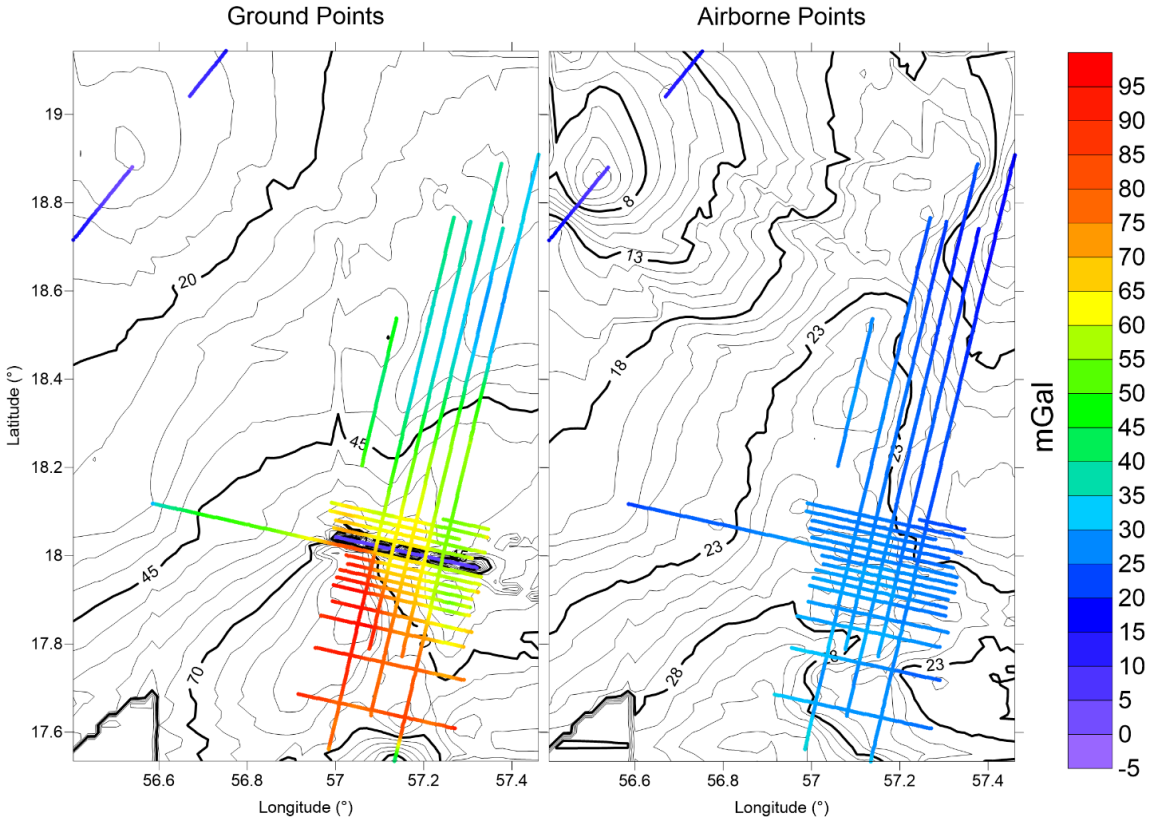

Figure 4-10. Comparison of ground gravity anomalies (left panel) and their equivalent airborne gravity anomalies (right panel) of survey points in Line L4B. *Similar to Line L4A, the contours of the "ground" gravity points bear no resemblance to their airborne counterparts. Colors signify the value of the gravity anomaly indicated on the side color scale bar.*

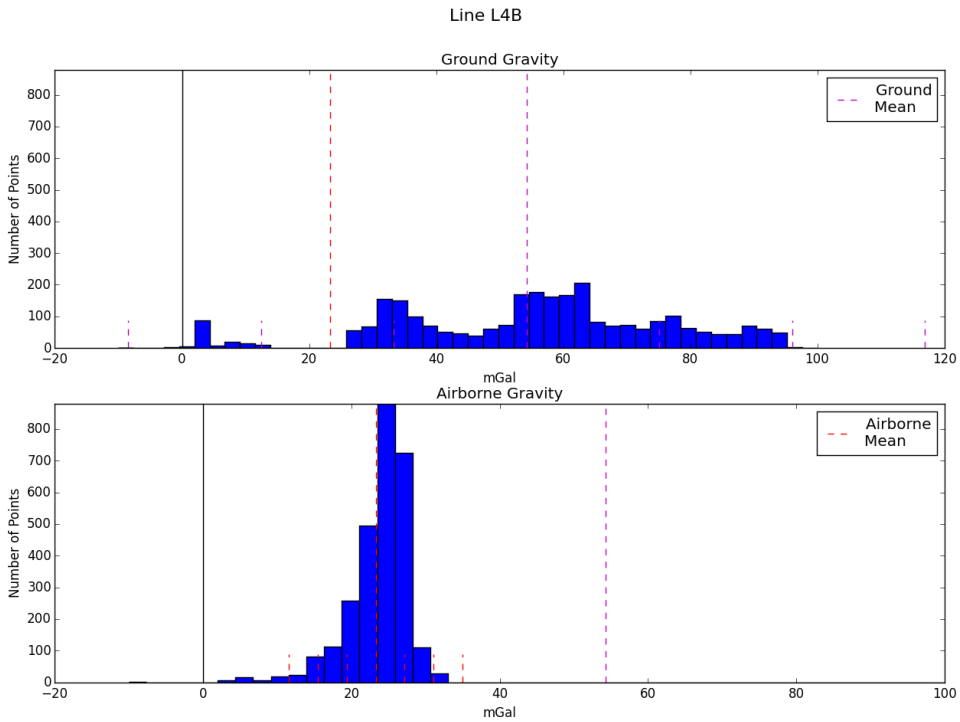

Figure 4-11. Histogram of ground gravity anomalies (upper panel) and their equivalent airborne gravity anomalies (lower panel) of survey points in Line L4B*. Similar to Line L4A, there is a noticeable difference between the ground and airborne histograms that invalidates the histogram postulation.*

In addition to the outliers (L4A, L4B) that were removed previously, inconsistencies between different survey lines at their borders with other lines existed. Some survey lines, such as line L79 in Figure 4-3, contain tens of thousands of points spread over large regions of the country. While Figure 4-3 demonstrates that the airborne and ground datasets are visually almost identical, very small but undefined biases still exist. In addition, several of the lines containing newly observed and properly referenced gravity data, that were previously assumed to be correct and un-biased, due to being observed relative to Oman's current gravity datum, were found to have rather large biases. It is still unclear whether the biases in these new observations were a result of poorly referenced gravity measurements, bias errors from the downward continuation of the airborne gravity anomalies in the mountainous areas, or related to other unknown effects of the histogram postulation.

4.2 Gridding of gravity anomalies

The bias repaired, point gravity anomalies need to be gridded in order to be merged with the airborne gravity anomalies. When gridding point values with least squares collocation (Kriging), the best results are attained when the values to be gridded are as smooth as possible.

An adequately smooth point dataset has minimal high frequency variation. Of all the gravity anomalies, complete Bouguer anomalies are the “smoothest”, and therefore, the most desirable set of values to grid. A complete Bouguer anomaly, shown in Equation (4.2), was calculated for the entire Oman territory, by adding an additional terrain roughness term to Equation (2.19).

$$\Delta g_{ba\_complete} = \Delta g_{fa} - 2\pi G\rho H + c_p \tag{4.2}$$

The additional terrain roughness term, c_p is known as the classical terrain correction term. It is always positive, and takes into account the deviation of the topography from the Bouguer plate correction applied to the free air anomalies in Equation (2.19), and is given by Equation (4.3) (Tocho et al., 2005).

$$c_P = G \iint_E \int_{H_P}^{H} \frac{\rho(x,y,z)(H_P - z)}{\left(\sqrt{(x_P - x)^2 + (y_P - y)^2 + \left(H_p - z\right)^2}\right)^3} dxdydz \tag{4.3}$$

The first integral limit is given by E and represents the integration over the entire surface of the Earth. The second integral limit from H_P to H represents integration over the height from the terrain at H_P downwards to the height H of the integration point. The denominator of the quantity inside the integral is the Euclidian distance between the integration point and the location of the terrain correction. The coordinates $x,\ y$, and z are the variables of the integration. The location of the point where the terrain correction is being computed, is represented by the variables x_P, y_P, and H_P.

The always positive nature of the roughness correction term is a result of the interaction between the computation point P and masses above and below it (Hofmann-Wellenhof & Moritz, 2006). Mass surpluses from the terrain, present above the Bouguer plate at point P, attract P in a direction opposite to gravity. Removing the mass surpluses will increase the value of g at point P because their attraction is no longer competing against gravity. Mass deficiencies, which are areas with assumed zero mass, below the Bouguer plate, will not have an attractive force on P. Filling in the deficiencies will add more mass below P and will also increase g at point P. Since the roughness term characterizes the high frequency deviations from the Bouguer plate, the greater the variation of the terrain surrounding point P, the larger the correction term will be. A diagram showing how the roughness of the terrain contributes to c_p at a calculation point can be seen in Figure 4-12.

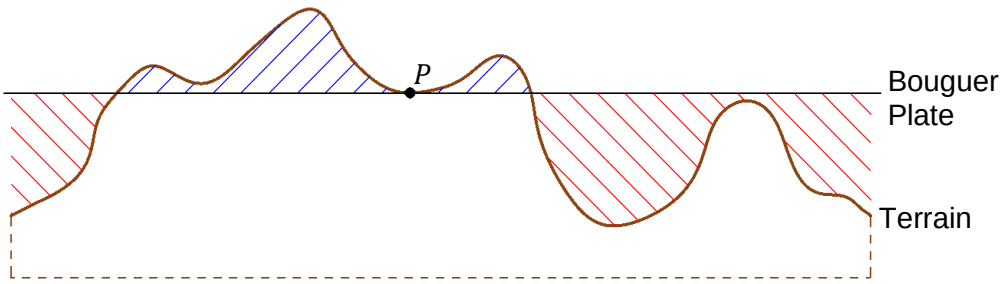

Figure 4-12. Roughness terrain correction. *Mass surpluses are shown in blue and mass deficiencies are shown in red. Mass surpluses are removed to eliminate the attraction opposite the gravity vector; increasing the value of g at point P. Empty mass deficiencies with zero attraction to P are filled in to increase the value of g at point P.*

The triple integral required to compute the roughness term is simplified when detailed density information is unknown. The density ρ is taken as the mean rock density of $2.67\ g/cm^3$ and the second integral limit is removed entirely; replacing the z variable with the orthometric height of each moving point designated by the double integral limit over the surface of the Earth. Due to the insignificant contributions to the terrain correction term from distant masses, the first integral limit is often simplified to a specific neighborhood around the computation point extending to about 100 km in radius, depending on the roughness of the terrain.

The terrain roughness correction is calculated for every ground gravity observation point with a 100 km calculation radius using GRAVSOFT's TC function; however, a modification was made to the SRTM with bathymetry DTM. Due to the software's inconsistent and poorly documented method of handling negative elevations, the bathymetry component of the SRTM was converted to its rock equivalent topography (RET) form (Kuhn & Hirt, 2016). RET approximately condenses the masses of the ocean water and the ocean bottom topography (rock) to their equivalent mass in rock (Kuhn & Hirt, 2016). Since the average rock density is about 2.5 times greater than the density of water, it will take less volume of rock to have the same effect as the volume of water associated with the SRTM's bathymetry. For example, 1000 m of water will be equivalent to ~400 m of rock, so the -1000 m elevation in the SRTM with bathymetry dataset will be reduced to about -400 m in the RET SRTM dataset, and the roughness correction algorithm with density $\rho = 2.67 g/cm^3$ can be applied in the oceanic regions where bathymetry is available. The RET SRTM keeps the densities between land and sea consistent at $2.67 g/cm^3$.

Several functions in the GRAVSOFT software package make a distinction for negative elevation in input DTM files. In most cases, the grid cells with negative elevations are treated as being filled with sea water instead of material with density ρ. However, in practice, when dealing

with negative DTM elevations, the performance of the GRAVSOFT functions is not consistent with its documentation.

Since RET produces negative elevations that need to be treated with a density of $\rho = 2.67 g/cm^3$, a constant value equal to the inverse of the deepest elevation is added to the dataset, resulting in a minimum of zero and removes any confusion with respect to negative elevations. The effects of the constant term are removed at the end of the roughness calculations. The terrain roughness corrections for northern Oman can be seen in Figure 4-13.

After the terrain roughness is calculated the complete Bouguer anomalies are computed and gridded to $30" \times 30"$ using Golden Sun Software's SURFER program. After gridding, they are converted back to free air anomalies that are now reliably gridded and can be merged with the downward continued airborne data.

The "inverse" corrections that convert complete Bouguer to free air anomalies are performed at each grid cell using values of H from the SRTM. Since it is not advisable to grid data with high variability, the high frequency roughness terms computed for the 230 000 gravity points cannot be used to reclaim simple Bouguer anomalies from complete Bouguer anomalies. To compensate for this, the roughness term is computed for every grid cell's latitude and longitude inside Oman's borders; then the points are arranged into an array, providing a "gridded" roughness term.

The gridded free air anomalies have a strong dependence on terrain, a result of using H provided by the SRTM to inversely compute them from complete Bouguer anomalies. The final ground free air anomalies are shown in Figure 4-14.

The free air anomalies also characterize gravity features that were not directly observed, such as the tops of mountains, or any large areas that have not been surveyed. Depending on the interpolation distance and spatial location, the interpolated values for these areas can be unreliable; they are highly dependent on measurements taken nearby. Gravity is often observed at the base or valleys of mountains. Gridding these observed values can incorrectly skew the gridded values at the peaks of the mountains. When dealing with gaps in ground gravity coverage, such as the empty area in the southern part of Oman in Figure 3-1, points interpolated very far away from measured points have a much higher cumulated gridding error and are less dependable. While the ground gravity dataset characterizes much of the high frequency components in the gravity field, it still has gaps in its medium frequency coverage. The steps taken to compensate for this shortcoming will be discussed in the next chapter.

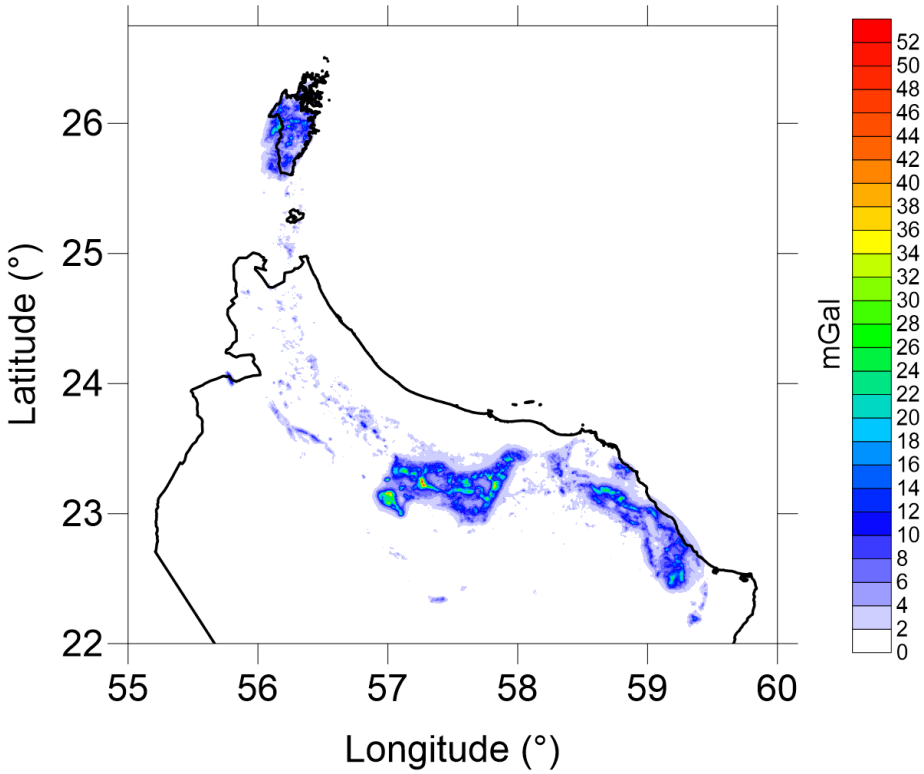

Figure 4-13. Terrain roughness corrections for northern Oman. *There is a strong correlation between the magnitude of the roughness correction and the elevation of nearby terrain features. The only other non-zero correction term, not shown here, is located in the southern mountains in the Dhofar region.*

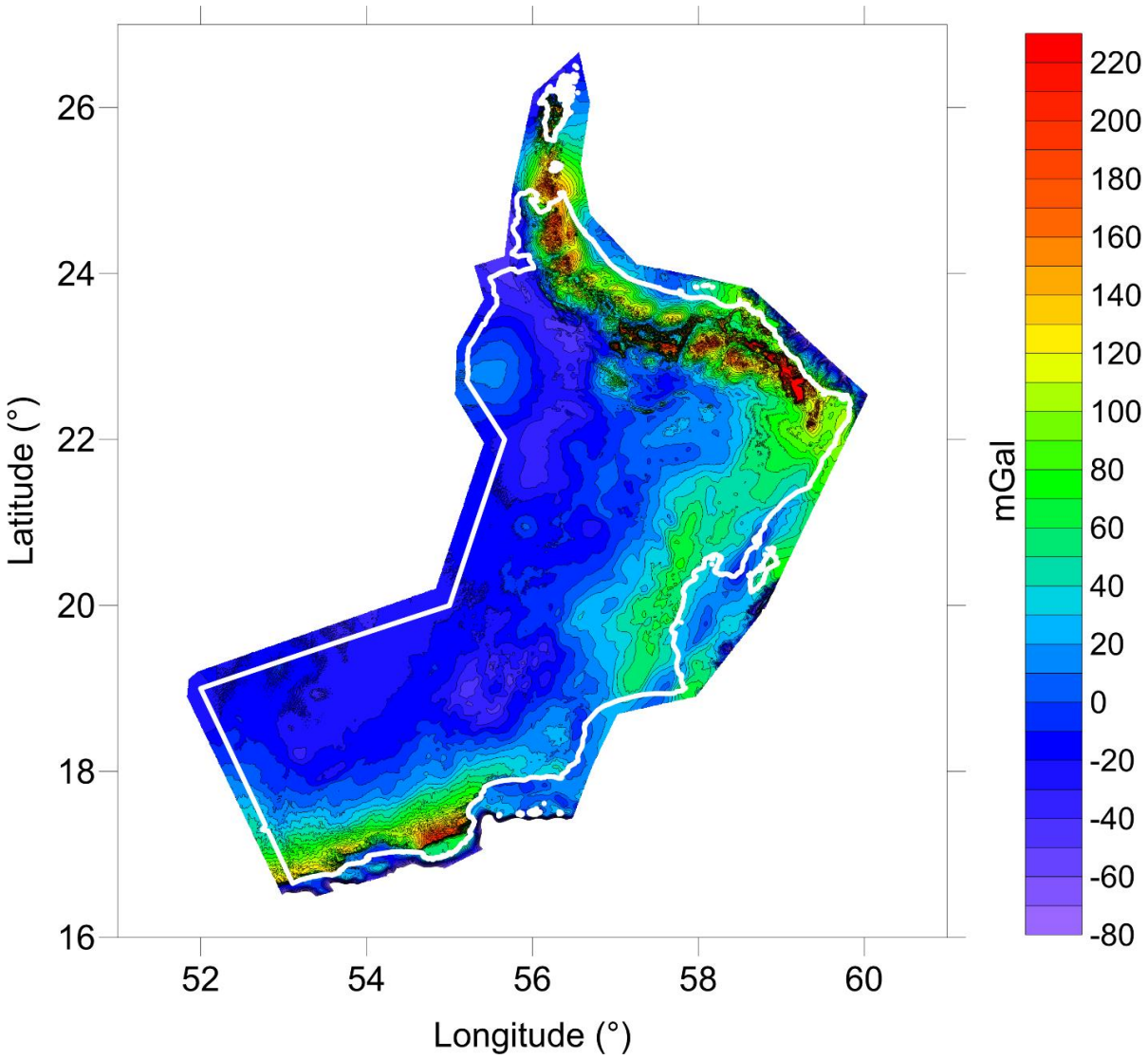

Figure 4-14. Bias-free ground free air anomalies*. The free air anomalies also show features that were not present in previous plots of free air anomalies, especially in areas where gaps in the gravity coverage that appear in Figure 3-1 are present.*

4.3 Summary

This chapter detailed the steps taken to un-bias the ground gravity anomaly dataset and prepare it for merging with the airborne dataset. Each gravity survey line was biased relative to the airborne free air anomaly dataset. The difference of the mean of the free air gravity anomalies of each survey line and its equivalent downward continued airborne free air anomalies was added to the survey line to un-bias it. Survey lines L4A and L4B, containing shipborne data, were removed and the reasons for their removal were discussed in detail. Lastly, the ground free air gravity anomalies were provided in a gridded format by first transforming them to complete Bouguer anomalies, gridding the smooth complete Bouguer anomalies and transforming them back.

5 Airborne data and ground-airborne data integration

5.1 Airborne gravity dataset

A large airborne gravity dataset with ~1.4 million points was observed over the entire country in the summer of 2015 (Géophysique GPR I'ntl Inc., 2015). It was observed over four measurement campaigns, with a traverse line spacing of 5 km in the mountainous and coastal region, and 10 km in the flat desert region. Its average altitude was ~900 m above the geoid, with the aircraft remaining about 600 m above the terrain at all times (Géophysique GPR I'ntl Inc., 2015). The dataset originally contained gravity disturbances δg, the formula for which is given in Equation (5.1).

$$\delta g = g_K - \gamma_K \tag{5.1}$$

The equation for δg is different from the formula for free air anomalies given in Equation (2.11). While free air anomalies are the difference between measured gravity and normal gravity on two different surfaces, gravity disturbances are the difference between measured gravity g_K and normal gravity γ_K on the same surface (at the same point). In the case of the airborne data, where K is the observation point in the air, the standard free air anomaly given by Equation (2.11) can also be re-written as a function of observations at K, as shown in Equation (5.2) (Hofmann-Wellenhof & Moritz, 2006),

$$\Delta g_{fa} = (g_K + 0.3086 H_a) - (\gamma_K + 0.3086(H_a + N)) \tag{5.2}$$

where H_a is the orthometric height of the airborne observation point, $H_a + N$ is the geodetic height of the observation point, and N is the geoid undulation of the terrain point corresponding to the airborne point. The first term in Equation (5.2) shows that gravity on the geoid g_p is equivalent to g_K measured at point K plus a free air reduction to the geoid. The second term in Equation (5.2) shows that normal gravity on the reference ellipsoid γ_Q is equivalent to normal gravity γ_K at point K plus a free air reduction to the reference ellipsoid. Therefore, Equation (5.2) can be used to convert observed gravity at point K to free air anomalies at altitude.

Since gravity disturbances, not observed gravity, were provided in the airborne dataset, Equation (5.2) can be simplified by cancelling the $+0.3086H_a$ free air gradient term and expanding the remaining terms. Equation (5.3) shows that taking away $0.3086N$ from the gravity disturbances will give the free air anomaly at altitude.

$$\Delta g_{fa} = g_K - (\gamma_K + 0.3086N) = g_K - \gamma_K - 0.3086N = \delta g - 0.3086N \quad (5.3)$$

The free air anomalies at altitude can be seen in Figure 5-1. No additional steps were taken to smooth the free air anomalies before gridding, as airborne measurements lack high frequency measurements and are already smooth.

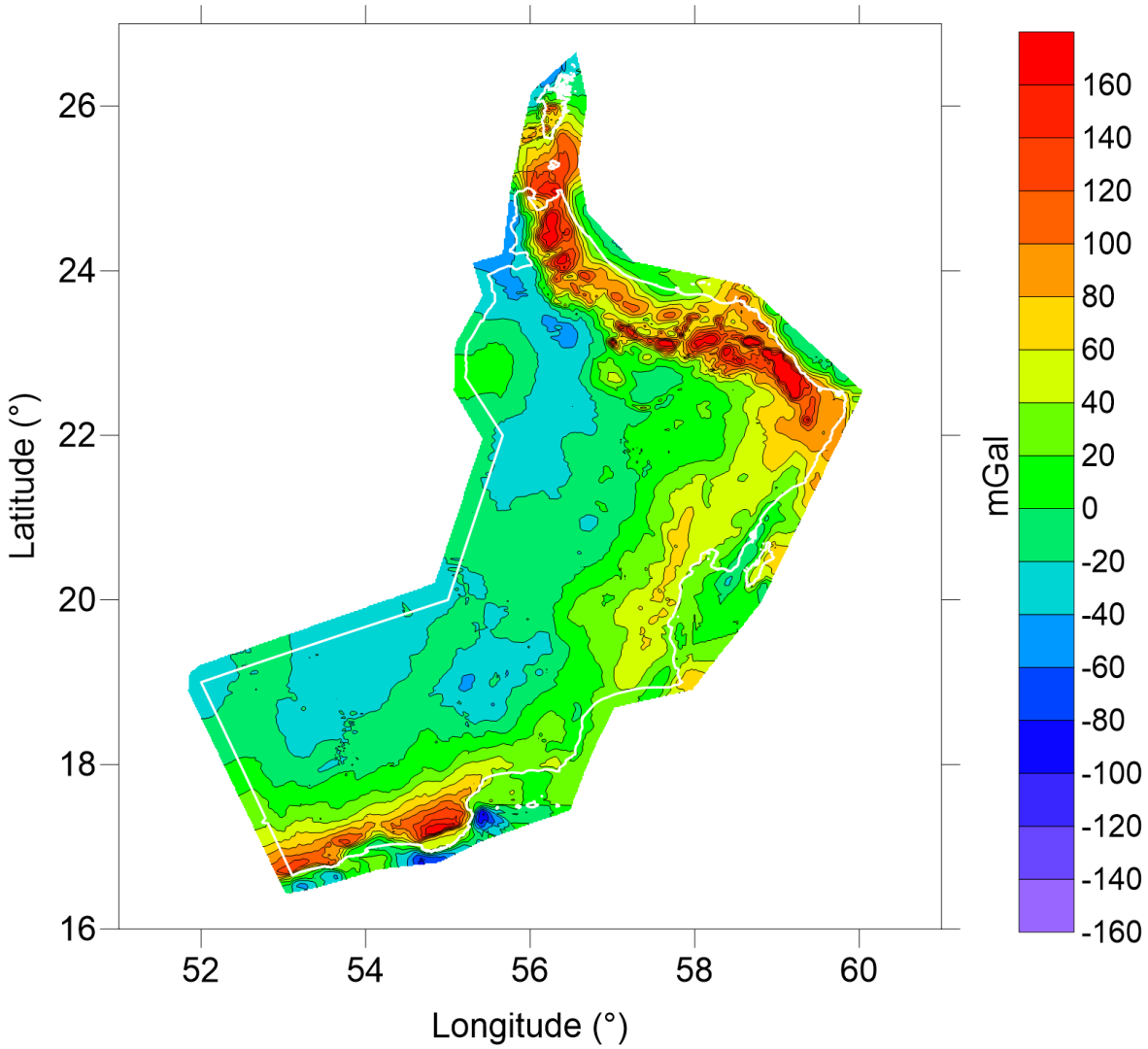

Figure 5-1. Free air anomalies at altitude. *Free air gravity anomalies at flight altitude, derived from airborne gravity disturbance measurements. The airborne free air gravity anomalies characterize the medium frequency components of Earth's gravity field, and capture features in the northern mountainous region's gravity field not present in Figure 3-10, due to the ineffective sampling in Figure 3-1.*

5.2 Downward continuation of airborne gravity anomalies

To downward continue airborne gravity anomalies to the geoid, the inverse Poisson integral must be used. As mentioned previously, the Poisson integral is the solution to the 1st BVP for the exterior gravity potential V_e, outside a boundary surface S, given the gravity potential V on S. The inverse problem starts with V_e outside S, and attempts to solve for V on S. As with all inverse problems, the solution is inexact and unstable.

The free air gravity anomalies at altitude are downward continued with the following Poisson integral formulas (Novak & Heck, 2002),

$$\Delta g(r,\Omega) = \frac{R}{4\pi r}\int_{\Omega} \Delta g(r,\Omega')K(t,u)d\Omega' \tag{5.4}$$

where

$$K(t,u) = \frac{t(1-t^2)}{\left(\sqrt{1-2tu+t^2}\right)^{3/2}} \tag{5.5}$$

and

$$t = \frac{R}{r} \tag{5.6}$$

$$u = cos\psi \tag{5.7}$$

The solution to determine the downward continued gravity anomalies is the inverse to the above equations. To facilitate this, the equations are stabilized with the Tikhonov-Phillips regularization (Novak & Heck, 2002). Downward continuing the airborne anomalies injects high frequency components into the medium frequency dataset. It attempts to transform the data measured at altitude, to what it would look like if measured on the ground.

The downward continuation of gravity anomalies is not within the scope of this thesis. The gravity anomalies at altitude were downward continued using the inverse Poisson integral by P. Novak via personal communication using proprietary software. The $1' \times 1'$ gridded free air anomalies at altitude were downward continued to the geoid determined from the global geopotential model EGM08. To facilitate the estimation of over 350 000 points, the airborne survey area was split into 30 quadrangles with no more than 20 000 points each. Each quadrangle's area was extended by 10 arc minutes, to prevent any edge effects from occurring between quadrangles when merging the results together. The results of the downward continuation can be seen below in Figure 5-2.

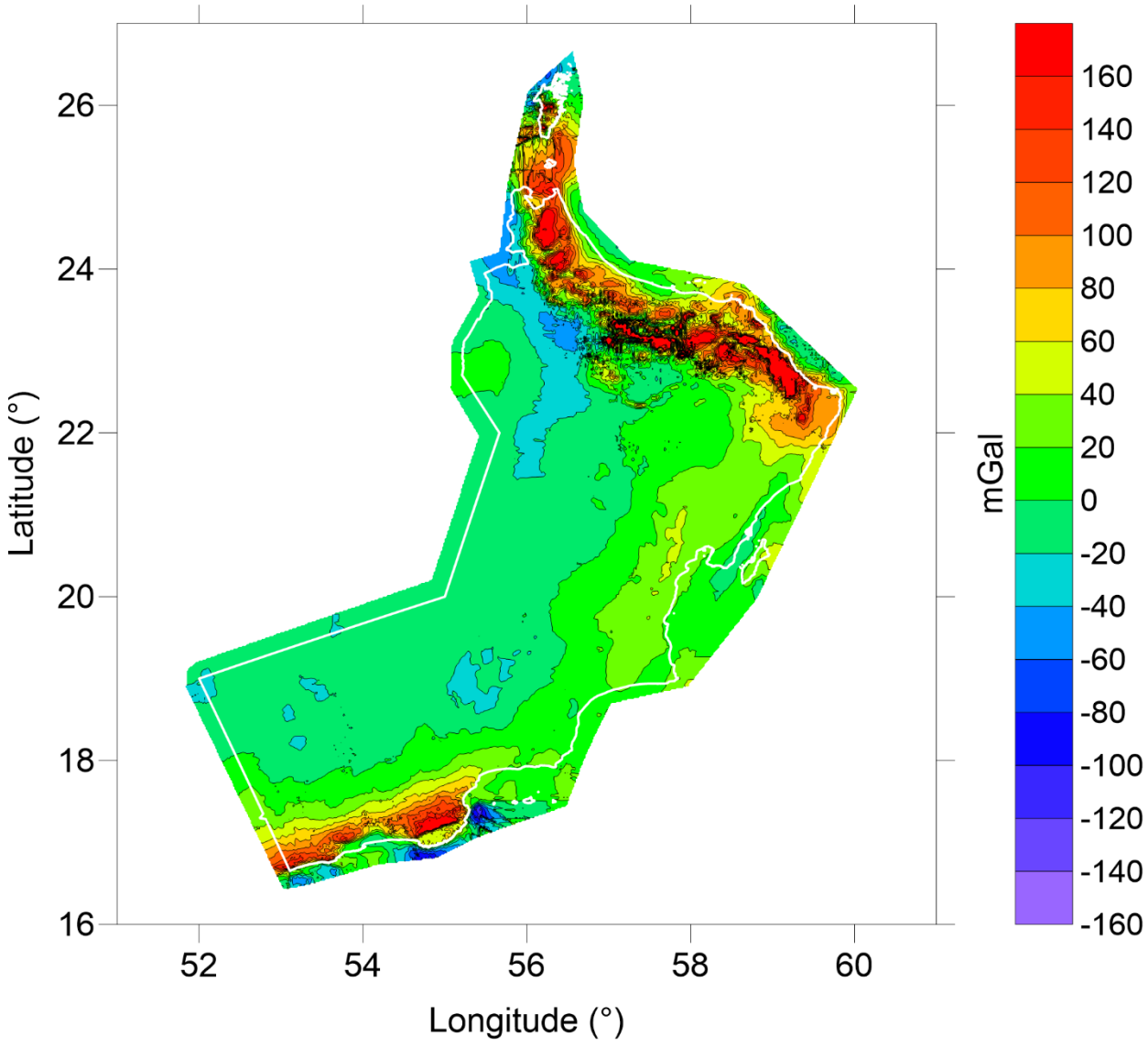

Figure 5-2. Downward continued airborne free air anomalies*. The large magnitude high frequency noisy components in the northern part of the country are artifacts from the inverse algorithm used to calculate the gravity anomalies on the geoid. The high frequency components over the mountainous regions are believed to be artifacts and are removed by low-pass filtering (see section 5.4).*

5.3 Ground-airborne geoid comparison

To verify that the ground gravity data were correctly bias repaired and the airborne data were correctly downward continued, preliminary geoids were calculated for each dataset using the methodology outlined in Chapter 6. This was done to verify that no apparent biases exist in either of the datasets and that the two datasets are compatible with each other and are therefore suitable for merging. Figure 5-3 shows the differences between the two geoids and Figure 5-4 shows the histogram of the differences.

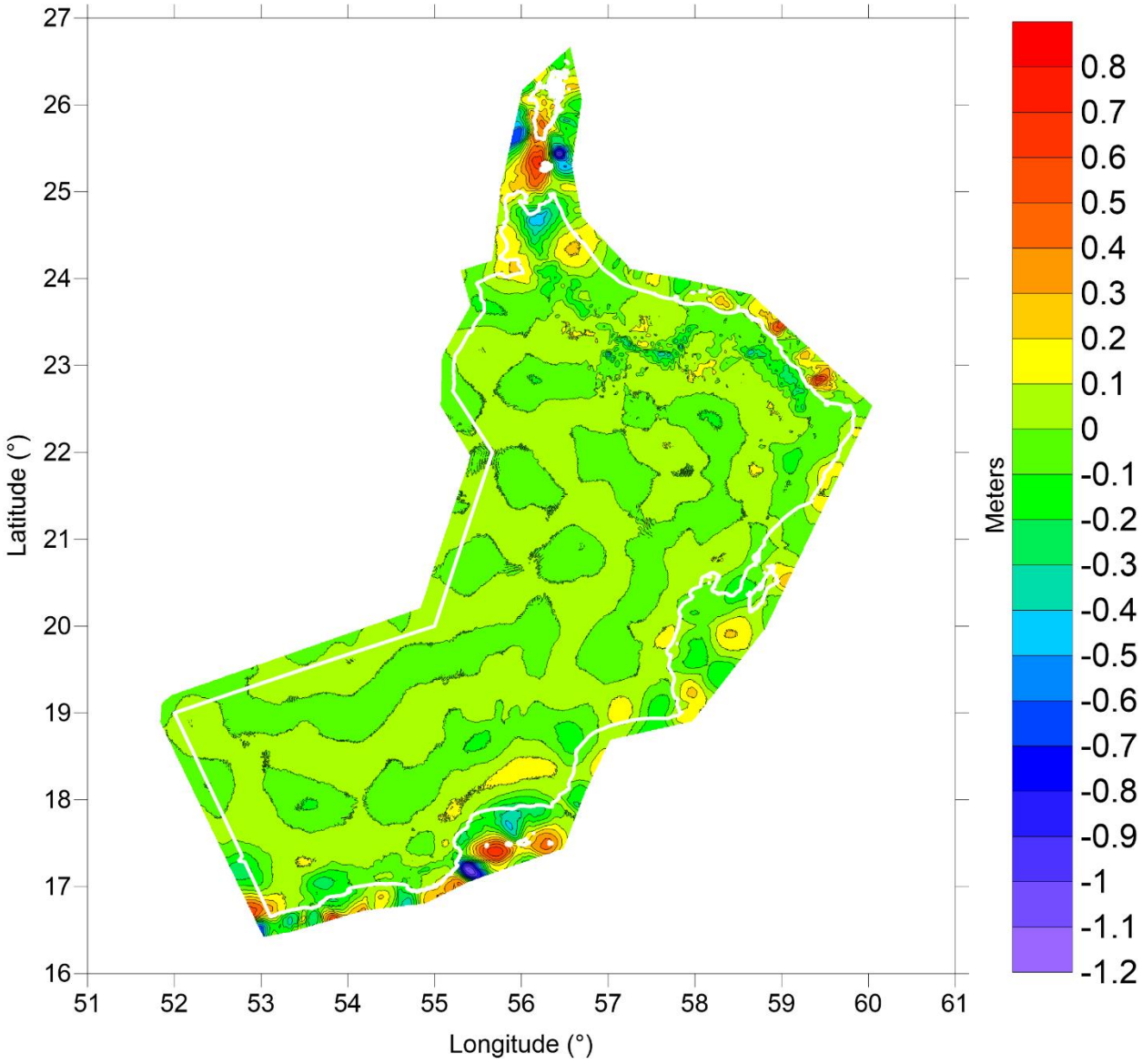

Figure 5-3. Preliminary ground geoid minus preliminary airborne geoid. The two geoids are very similar, with sub 20-centimeter agreements throughout the entire country. The majority of the differences appear smooth with the exception of the mountainous region in the northern part of the country. This area is better characterized by the ground observations and the geoid reflects this.

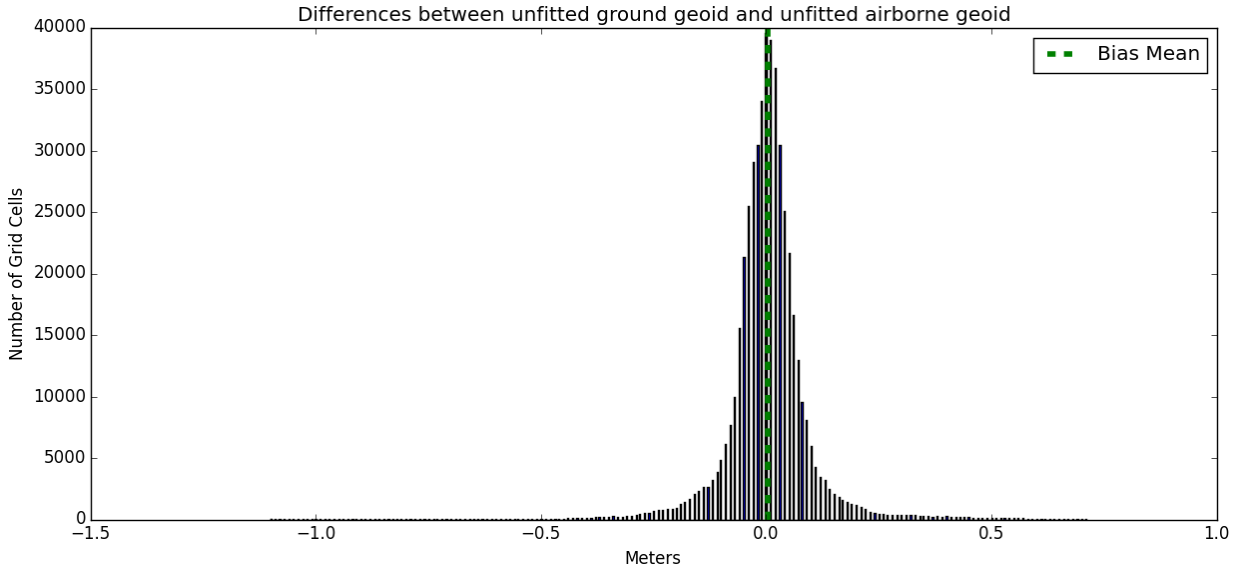

Figure 5-4. Histogram of the differences between the preliminary ground geoid and the preliminary airborne geoid. The average of the differences (ground geoid – airborne geoid) is 0 m and the standard deviation is 1 cm.

5.4 Ground-airborne data integration

Merging the adjusted ground gravity dataset with the downward continued airborne free air anomaly dataset allows the frequency content of each to be combined into one cohesive dataset. The merging is done by low-pass filtering the downward continued airborne gravity anomalies with an isometric Gaussian filter, and high-pass filtering the ground gravity anomalies using the complement Gaussian of the same cutoff frequency. The medium (airborne) and high (ground) frequency components of the gravity anomalies, are then added together, with no overlap in the frequency content.

The $1' \times 1'$ downward continued airborne free air gravity anomalies are resampled to $30" \times 30"$ to have the same spacing and coverage as the ground free air gravity anomalies. Both datasets are padded with zeros to increase the physical coverage of the grid. The ground and downward continued airborne free air gravity anomalies are filtered with an isometric 2-D Gaussian filter in the space domain, shown in Equation (5.8),

$$G(\phi, \lambda) = \frac{1}{2\pi\sigma_{km}^2} \exp\left(-\frac{d^2}{2\sigma_{km}^2}\right) \tag{5.8}$$

where σ is the standard deviation of the filter, and d is the spatial distance between the point that is being filtered and the running point. When working in spherical coordinates, the spatial distance is given by Equation (5.9),

$$d^2 = R^2(\delta\phi^2 + \cos^2\phi\delta\lambda^2) \tag{5.9}$$

where R is the mean radius of the Earth and is equal to 6371 km, ϕ is the geodetic latitude of the computation point, and $\delta\phi$ and $\delta\lambda$ are the differences in radians between the filtered point and the running point in latitude and longitude, respectively. The distance is computed using spherical geodetic coordinates instead of Cartesian coordinates, because the linear length (km) per one arc degree of longitude decreases towards the poles.

To determine the standard deviation σ that defines the cutoff frequency of the Gaussian filter in Equation (5.8), we use Equation (5.10),

$$\sigma_{km} = \frac{1}{2\pi}\frac{D_c}{\sqrt{2\ln(2)}} \approx \frac{D_c}{7.398} \tag{5.10}$$

where D_c is the cutoff wavelength; the point where 50 percent of the signal power is attenuated. When working in the space domain, D_c corresponds to the spatial wavelength required. For example, if the desired spatial resolution is D_c = 100 km, or $1° \times 1°$ in longitude (D/O 360 in spherical harmonics), σ will equal 13.5 km. For efficient computations, only points up to 3.2σ away from the point of interest should be filtered, to ensure that 99.5 percent of points with a meaningful contribution are filtered (3σ), plus a slight increase for redundancy. For example, for a spatial resolution of 100 km, the Gaussian kernel search radius should be 43.2 km. Since the highest airborne resolution is 20 km, that is, 2 times the 10 km line spacing, then the cutoff spacing for the ground data should be $\sigma = \frac{20}{7.398}$ = 3 km, and the kernel value should be computed for a 3.2×3 = 10 km radius.

The downward continued airborne and the ground free air gravity anomalies are low-pass filtered with a 3 km Gaussian filter. The low-pass filtered ground free air anomalies are subtracted from the initial unfiltered ground free air anomalies, leaving the high frequency component to be merged to the airborne anomalies (Figure 5-6). At this point, the medium (Figure 5-5) and high (Figure 5-6) frequency components are added together to make the final free air gravity anomaly dataset (Figure 5-7), and the simple Bouguer anomaly dataset (Figure 5-8) that will be used to compute the geoid.

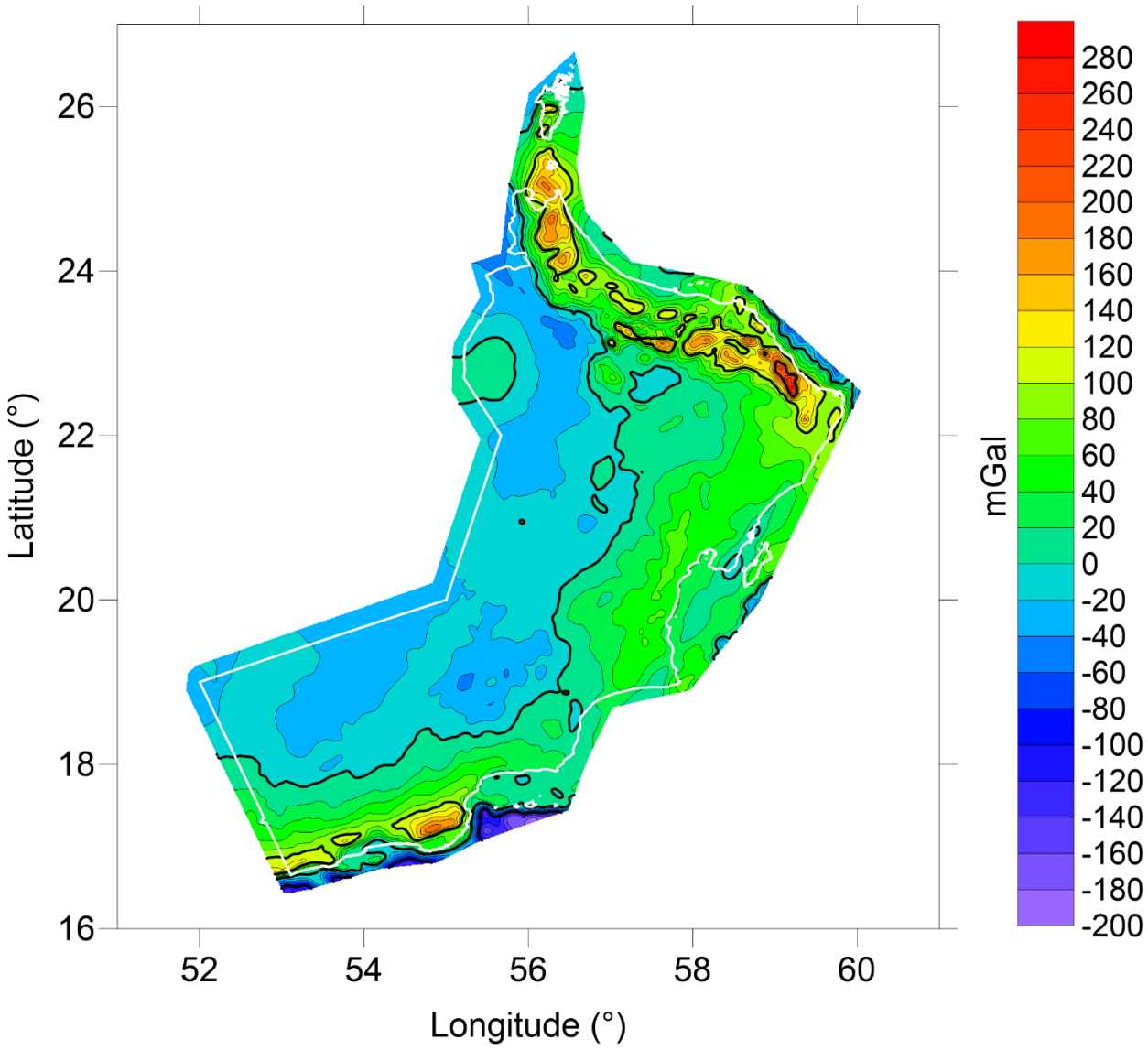

Figure 5-5. Downward continued airborne free air anomalies filtered with an isometric Gaussian filter in the spatial domain. *The airborne dataset displays the medium frequency components of Earth's gravity field after the application of the Gaussian filter.*

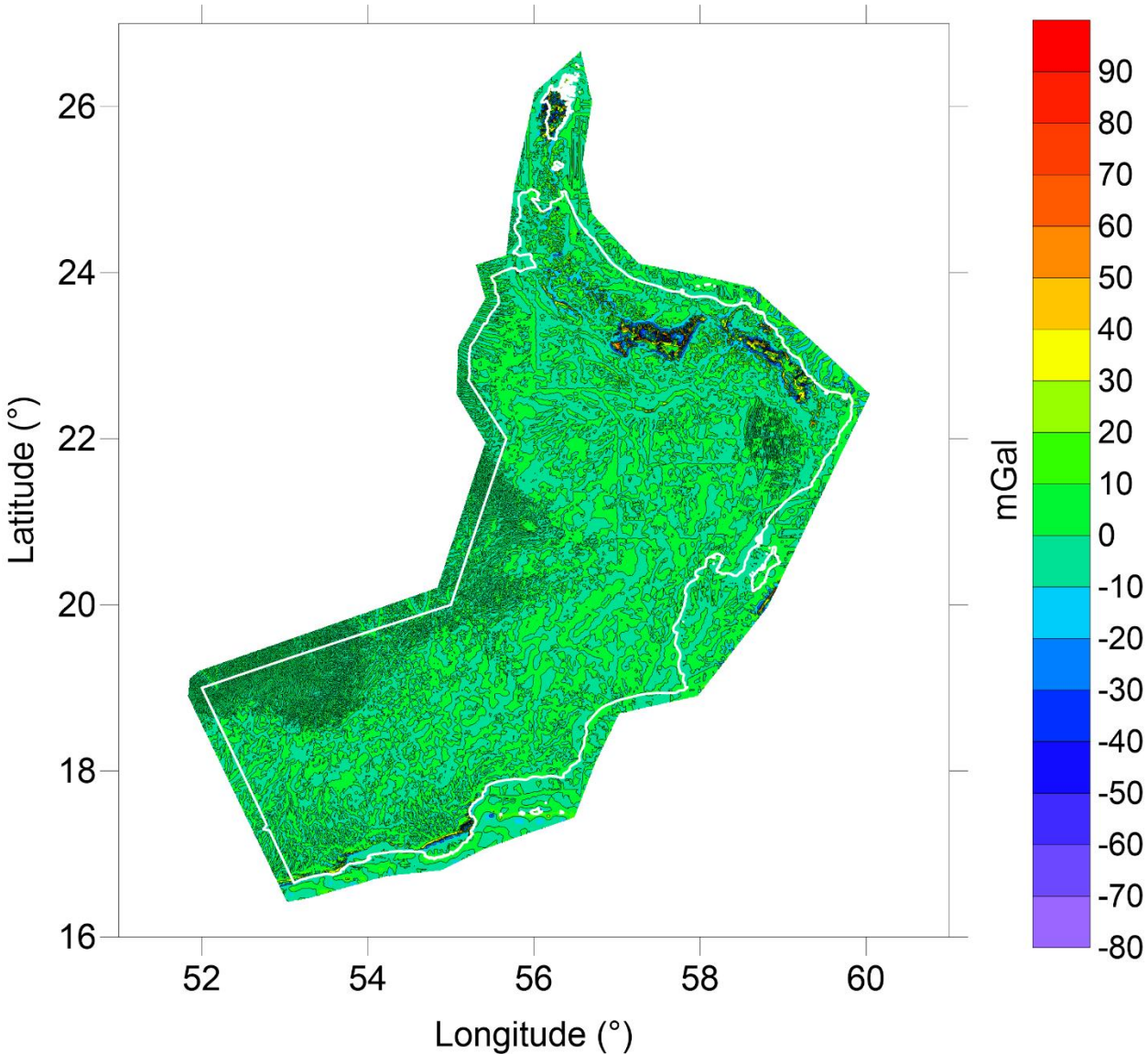

Figure 5-6. High frequency free air anomaly computed from the ground free air anomalies by Gaussian filtering.

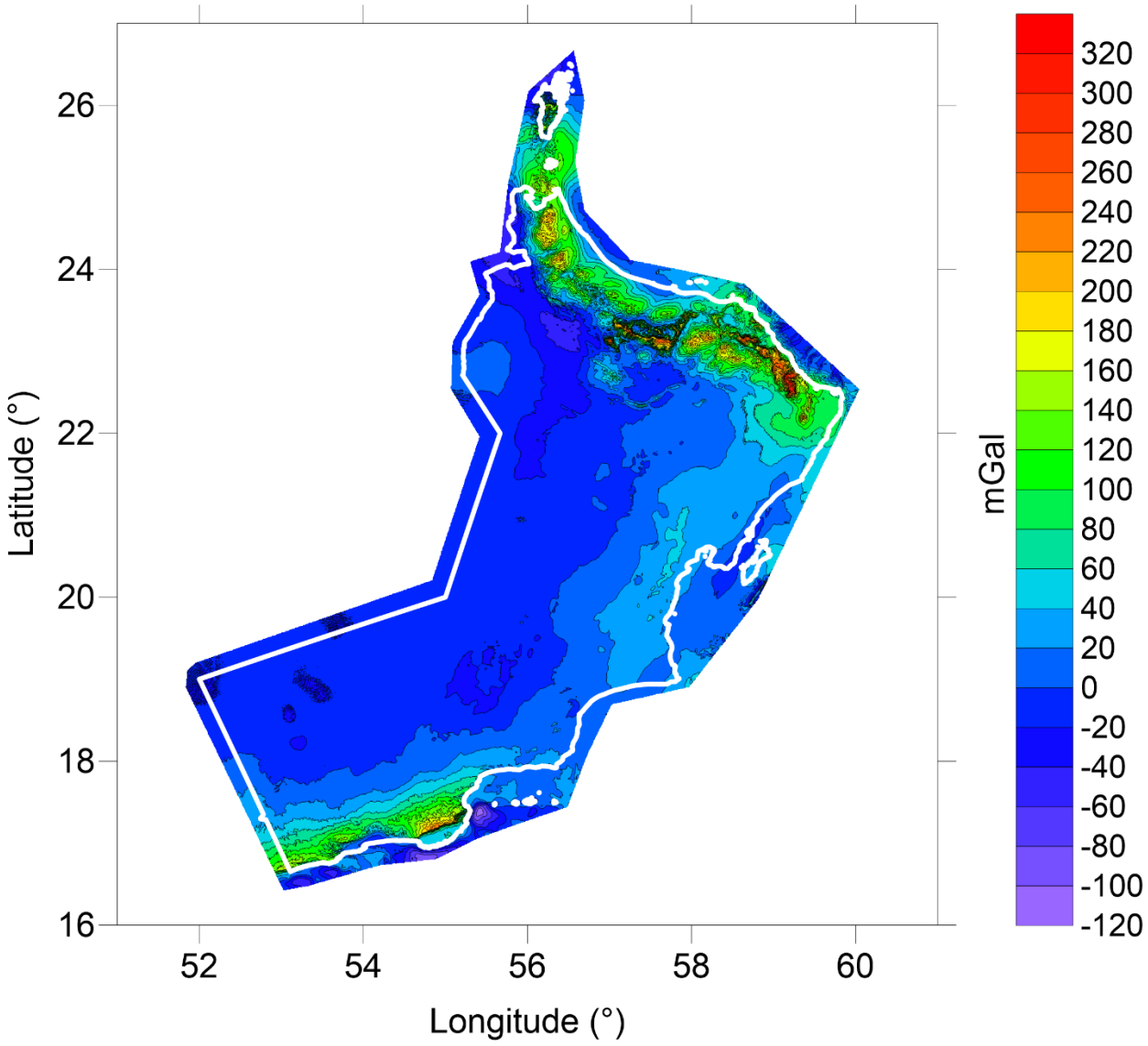

Figure 5-7. Final ground gravity free air anomalies created from airborne free air anomalies (downward continued and filtered) merged with ground free air anomalies (filtered).

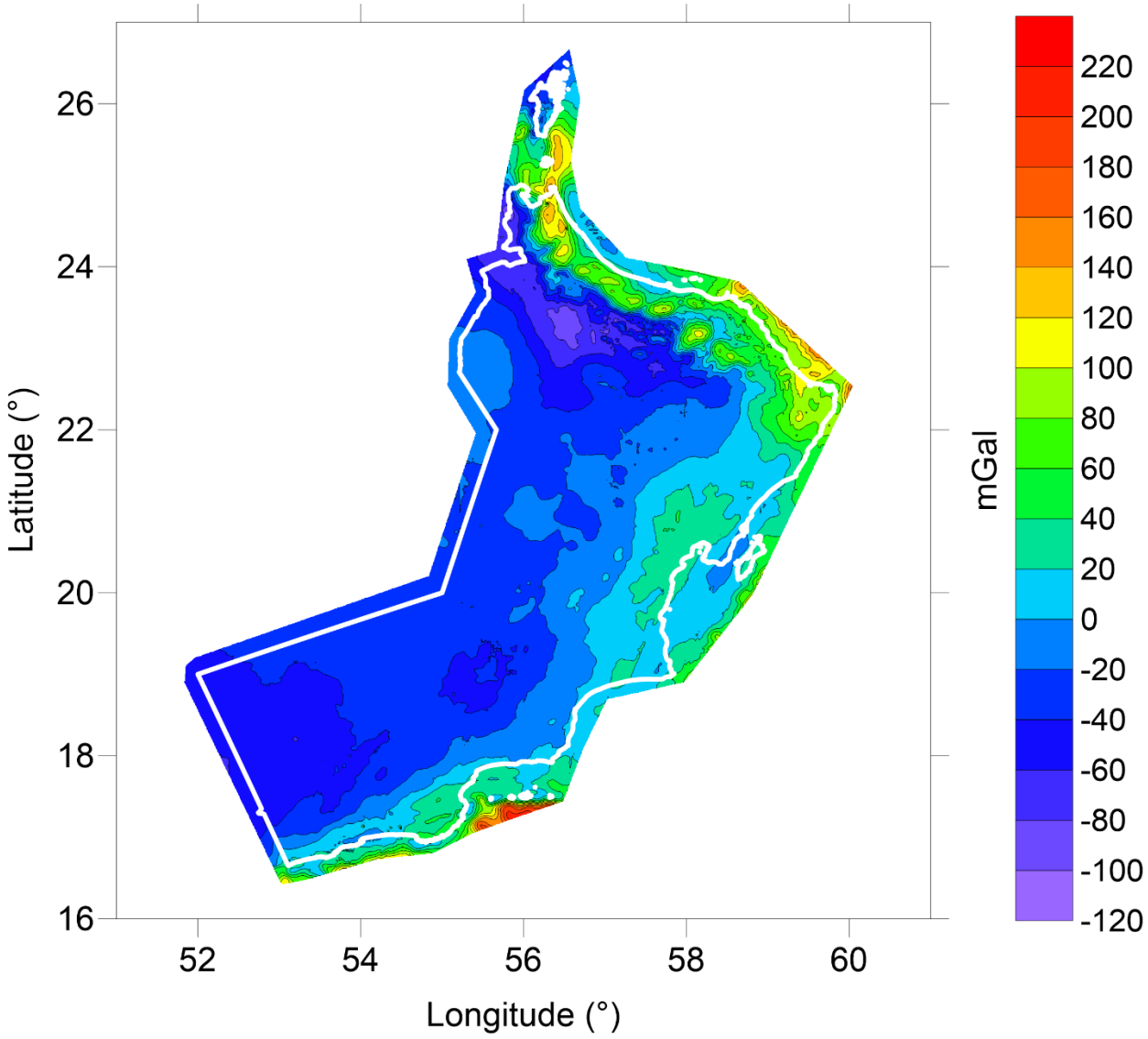

Figure 5-8. Simple Bouguer anomalies derived from final ground gravity free air anomalies.

5.5 Verifying free air anomalies with a global geopotential model

For quality control purposes, the free air anomalies in Figure 5-7 were compared to a pure, satellite determined, global geopotential model. While the satellite model would not characterize the high and medium frequencies of the free air anomalies, it would demonstrate whether any significant low frequency biases remain in the anomalies. The low-pass Stokes integral would not remove the low frequency biases, and they would persist throughout the entire remove-compute-restore process, biasing the final gravimetric geoid.

The pure, satellite determined, global geopotential model selected is the GOCO05s GGM to D/O 280, from the German Research Centre for Geosciences (GFZ) (Mayer-Gürr et al., 2015). It is generated using the International Center for Global Earth Models (ICGEM) online computation service. Figure 5-9 shows the difference between the two free air anomaly maps. Figure 5-10 shows the histogram of differences seen in Figure 5-9 within the country's borders. The differences in Figure 5-9, are expected since the GOCO05S satellite model is not capable of characterizing the high frequency variation of the ground gravity dataset. The final ground gravity dataset is acceptable because it appears that there are no longer any biases in the ground gravity dataset

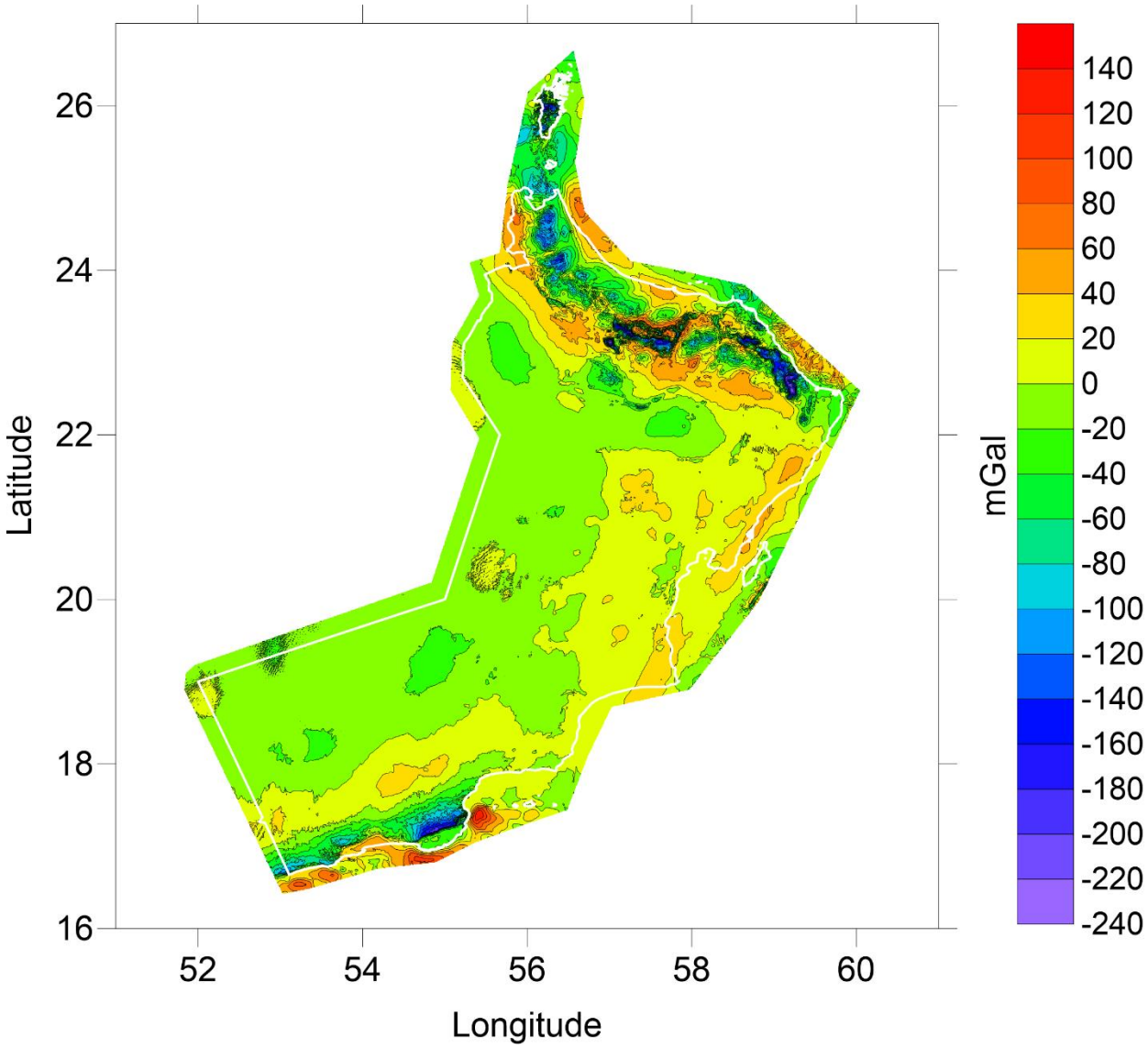

*Figure 5-9.*GOCO05s minus final free air anomalies. *The large differences in the mountainous and coastal regions are expected due to the high frequency components present in the free air anomalies. The low degree and order of the satellite model (280) cannot characterize the ground data at these high frequencies.*

The histogram in Figure 5-10 appears to be nearly normally distributed but positively skewed. The peak around -15 mGal represents the medium and high frequency components present in the mountainous areas of Oman that the satellite model cannot adequately characterize. The larger differences that are 80 to 100 mGal represent the high frequency components present in the tallest mountains that the satellite is unable to characterize.

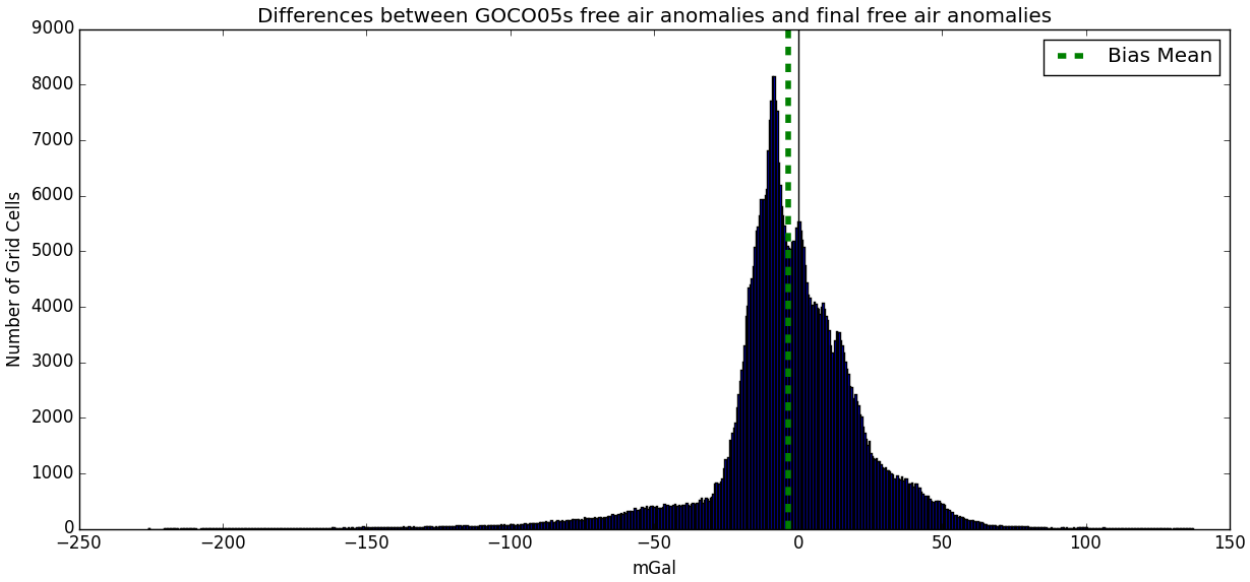

Figure 5-10. Histogram of differences between GOCO05s free air anomalies and final free air anomalies*. The average of the differences (GOCO05s – Final Free Air Anomalies) is -3.25 mGal and the standard deviation is 27.2 mGal.*

5.6 Summary

This chapter explained the steps required to create the final free air gravity anomaly dataset that will be used to calculate the geoid. First, the airborne free air gravity anomalies at altitude were downward continued to the geoid using the inverse Poisson integral. Next, using an isometric Gaussian filter, the airborne and ground free air anomaly grids were low-pass and high-pass filtered, respectively, in order to extract the low and high frequency components of the gravity field. The sum of the two frequency components are the final free air gravity anomalies, which were verified against the pure, satellite determined, global geopotential model GOCO05s.

6 Geoid calculations

6.1 Remove-compute-restore technique

The method used to calculate the geoid in Oman is the remove-compute-restore (RCR) methodology. According to this methodology, the contribution of the gravitational attraction of the topographic masses to the gravity anomalies is removed as much as possible to render them smooth. The smooth residual gravity anomalies are then convolved with the Stokes integral to compute the high frequency component of the quasigeoid. Finally, the removed effects are restored after being converted to their corresponding quasigeoid components and are added to the high frequency quasigeoid to determine the full quasigeoid. As a last step, the quasigeoid is transformed to the geoid using simple Bouguer anomalies and a DTM.

6.2 Remove step

The purpose of the remove step is to make the gravity anomalies smooth and easy to grid by removing as much information as possible. The global gravity signal is removed to eliminate the long wavelength components not adequately characterized by the discrete computation neighborhood, while the high frequency terrain effects are removed from the gravity anomalies to eliminate any short wavelength biases in the gravity anomalies from the local terrain.

The general mathematical process of the remove step is given in Equation (6.1). The long wavelength gravitational effects of a global geopotential model Δg_{egm}, such as EGM08, and the high frequency local terrain effects Δg_{ter}, (i.e., the gravitational effects of the roughness of the topography with respect to a smooth representation of the actual topography, such as a mean height reference surface), are removed from the free air anomalies Δg_{fa}, leaving behind smooth residual gravity anomalies Δg_{res}.

$$\Delta g_{res} = \Delta g_{fa} - \Delta g_{egm} - \Delta g_{ter} \tag{6.1}$$

In this research, Δg_{egm} is calculated from the EGM08 global geopotential model to D/O 360, using the International Center for Global Earth Models (ICGEM) online computation service. The effects of the terrain Δg_{ter} are computed using the RTM approach (Forsberg & Tscherning,

1981) by using a smooth height reference surface created by low-pass filtering of the actual topography (see below in Figure 6-1).

The RTM method considers only the short and medium wavelength gravitational effects of the topography. The linear approximation of Δg_{ter} for the RTM effect at a single point P is expressed in Equation (6.2) (Forsberg, 1984),

$$\Delta g_{ter} = 2\pi G\rho\left(H - H_{ref}\right) - c_p \tag{6.2}$$

which has some similarities to the terms added to free air anomalies when computing complete Bouguer anomalies. However, an additional smooth reference surface is utilized; H is the height of the computation point, H_{ref} is the height of the smooth reference surface at the same computation point, and c_p is the classical terrain correction that characterizes roughness, mentioned previously in Equation (4.3).

In essence, the first component of Equation (6.2) is the difference between two Bouguer reductions. The gravitational effects of the actual topography $2\pi g\rho H$ (with respect to the geoid) are removed from the free air anomalies, and the effects of the smooth topography $2\pi g\rho H_{ref}$ are added back, this is illustrated in Figure 6-1.

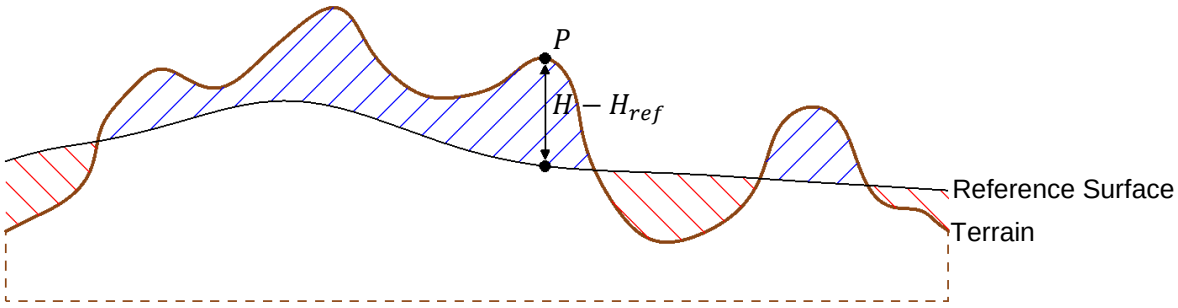

Figure 6-1. RTM terrain effect theory. *The blue hatched areas above the reference surface show the removal of the actual topography. The red hatched areas below the reference surface show the effects of the smooth topography that are added back. The empty region below the reference surface is consistent between both Bouguer reductions.*

If the smooth topography is created from a low-pass filter, the RTM reduction corresponds to an isostatic reduction (Moritz, 1968), which characterizes the medium frequency components of topography. A 100 km low-pass spatial filter is chosen for this purpose, and the mean reference surface is computed using GRAVSOFT's TCGRID function. The TCGRID function takes an input grid file and low-pass filters it based on a moving average window specified by the user.

The gridded values of Δg_{ter} are computed in Python with simple grid mathematics using the SRTM with RET bathymetry model to create the smooth reference surface over land and

oceans. The final terrain effects are shown in Figure 6-2. The classical roughness term c_p is provided by the gridded corrections computed by TC in Chapter 4. The global geopotential effects Δg_{egm} and local terrain effects Δg_{ter} are subtracted from the free air anomaly dataset with GRAVSOFT's GEOIP function, which adds or subtracts differently spaced grids. The resultant residual gravity anomaly dataset is now ready to input into the Stokes integral in the compute step.

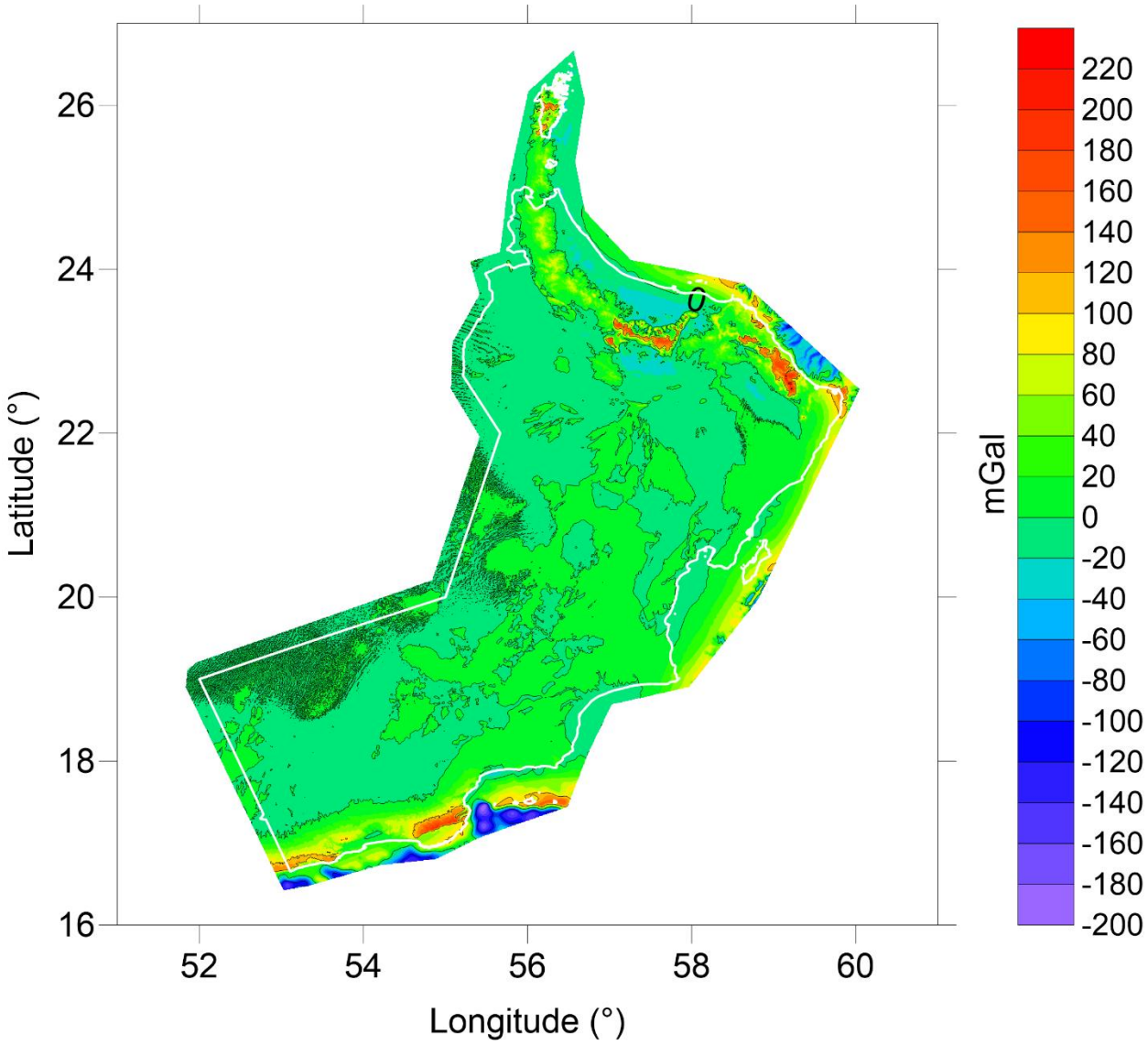

Figure 6-2. RTM terrain effects*. The purpose of creating the residual anomalies is to remove as much information as possible from the free air anomalies to make them smooth. The low frequency EGM component and the high frequency terrain effects are removed, leaving behind a smooth medium frequency surface.*

6.3 Remove step workflow

Table 6-1 shows the GRAVSOFT and Python software required to complete the remove step. Unless explicitly stated, the spatial extent of any datasets are $\phi\,[15.25°, 27.75°]$ and $\lambda\,[50.75°,\ 61.25°]$. The SRTM contains RET corrected bathymetry, and the entire dataset has a constant added to avoid negative elevations in the oceans. The computation of the roughness term c_p in step 2A does not require any software modification to remove the constant because the roughness calculation for a point is relative to that point's elevation, instead of the dataset as a whole. The constant must be removed when computing the difference in Bouguer slabs in the Python software in step 2B.

Table 6-1. Remove step software workflow

	Description	Input	Software	Output
DTM setup				
1A	Resample SRTM	$\boldsymbol{SRTM}_{[3"\times3"]}$ $\phi\,[14° \quad 28°]$ $\lambda\,[48° \quad 62°]$	**SELECT**	$\boldsymbol{SRTM}_{[30"\times30"]}$
1B	Get Reference Surface (~100 Km)	$\boldsymbol{SRTM}_{[30"\times30"]}$	**TCGRID**	$\boldsymbol{SRTM_{ref}}_{[30"\times30"]}$
Calculate Δg_{ter}				
2A	Compute c_p	List of Point Free Air anomalies from $\boldsymbol{\Delta g_{fa}}_{[30"\times30"]}$ $\boldsymbol{SRTM}_{[30"\times30"]}$ $\boldsymbol{SRTM_{ref}}_{[30"\times30"]}$	**TC**[1] in mode 3	$\boldsymbol{c_p}_{[30"\times30"]}$
2B	Compute $2\pi G\rho(H - H_{ref})$ *(Difference in Bouguer Slabs)*	$\boldsymbol{\rho} = 2.67$ $\boldsymbol{SRTM}_{[30"\times30"]}$ $\boldsymbol{SRTM_{ref}}_{[30"\times30"]}$	**TC**[1] in mode 4	$\boldsymbol{\Delta_{BA}}_{[30"\times30"]}$
2C	Calculate Δg_{ter}	$\boldsymbol{\Delta_{BA}}_{[30"\times30"]}$ $\boldsymbol{c_p}_{[30"\times30"]}$	**GCOMB** in mode 1	$\boldsymbol{\Delta g_{ter}}_{[30"\times30"]}$
Calculate Δg_{res}				
3A	Subtract Δ_{egm08} D/O 360 from Δg_{fa}	$\boldsymbol{\Delta g_{fa}}_{[30"\times30"]}$ $\boldsymbol{\Delta g_{egm08}}_{[30"\times30"]}$	**GCOMB** in mode 1	$\boldsymbol{\Delta g_{temp}}_{[30"\times30"]}$
3B	Compute Δg_{res} by subtracting Δg_{ter} from Δg_{temp}	$\boldsymbol{\Delta g_{temp}}_{[30"\times30"]}$ $\boldsymbol{\Delta g_{ter}}_{[30"\times30"]}$	**GCOMB** in mode 1	$\boldsymbol{\Delta g_{res}}_{[30"\times30"]}$

[1]Modified for large datasets

6.4 Compute step

The Stokes integral is applied to the residual gravity anomalies Δg_{res} to generate $\zeta_{\Delta g_{res}}$, the residual height anomaly (residual quasigeoid height) according to the Molodenskij approach since all gravity anomalies used in the calculations refer to the topography and not to the geoid. For this calculation, the FFT implementation of GRAVSOFT's SPFOUR (Forsberg, 2002) function is used, with Wong-Gore tapering of the Stokes Function and 100% zero padding of the input residual gravity anomalies. Equation (6.3) shows the modified Stokes function that is used to suppress the effects of any remaining long wavelength harmonics.

$$S_{mod}(\psi) = S(\psi) - \sum_{n=2}^{N} \alpha(n) \frac{2n+1}{n-1} P_n cos\psi \tag{6.3}$$

Each term of the summation is the value of the harmonic component corresponding to degree n. The tapering coefficient $\alpha(n)$ controls any Gibbs phenomenon that may arise from the "sharp" truncation of the special harmonics to degree N. The value of the summation for degree n is multiplied by the tapering coefficient, and is subtracted from the Stokes function. When $2 \leq n \leq N_1$, the function $\alpha(n)$ is equal to 1, and the corresponding summation element is removed from the Stokes function. When $N_1 < n \leq N_2$, the function $\alpha(n)$ is tapered down linearly from $0.9\overline{9}$ to 0. When $n > N_2$, the function $\alpha(n)$ is equal to 0, and the summation components are not removed. Figure 6-3 shows this tapering process.

The tapering is done to remove the same low frequency effects in the Stokes integral previously removed in the remove step in case there are still some low order harmonics present after the removal of the EGM08 of D/O 360. The Wong-Gore tapering is done to degree and order 360 because EGM08 D/O 360 has been removed; resulting in N_1 = 360 and N_2 = 365 to provide a smooth transition.

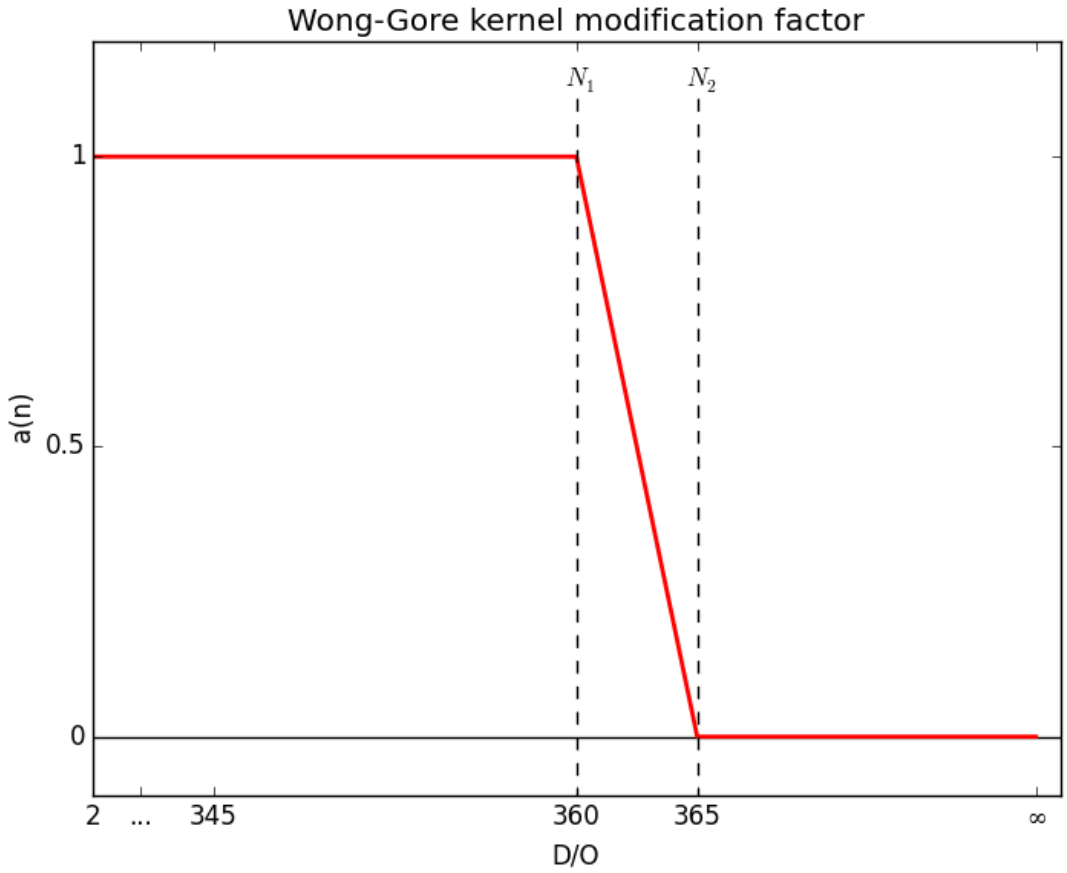

Figure 6-3. Wong-Gore Tapering kernel. *This plot illustrates the behavior of the factor $a(n)$ depending on the parameters chosen for degree and order. Every component up to N_1 is removed, components between N_1 and N_2 are removed linearly, and components after N_2 are not removed.*

6.5 Compute step workflow

Table 6-2 shows the GRAVSOFT software required to complete the compute step. The spatial extent of all datasets are ϕ $[15.25°, 27.75°]$ and λ $[50.75°, 61.25°]$.

Table 6-2. Compute step workflow

	Description	Input	Software	Output
1	Calculate $\zeta_{\Delta g_{res}}$	$\boldsymbol{\Delta g_{res}}_{[30"\times 30"]}$	**SPFOUR**[1] with Wong-Gore Kernel Modification	$\boldsymbol{\zeta_{\Delta g_{res}}}_{[30"\times 30"]}$

[1]Modified for large datasets

6.6 Restore step

The components removed from the free air anomalies to create the residual anomalies Δg_{res} need to be restored back to the residual height anomaly ζ_{res}, in the form of height anomalies ζ_{egm} and ζ_{ter}. This process is shown in equation (6.4),

$$\zeta = \zeta_{egm} + \zeta_{\Delta g} + \zeta_{ter} \tag{6.4}$$

where ζ_{egm} is the height anomaly computed from the EGM08 global geopotential model to D/O 360, using the ICGEM online computation service, and ζ_{ter} is the height anomaly due to the terrain effect, calculated by running the terrain effects Δg_{ter} through the Stokes integral without the Wong-Gore tapering. The grids holding each quantity on the right-hand side of the equation are added together using GRAVSOFT's GCOMB function, which can add or subtract grids with equal spacing and limits.

6.7 Restore step workflow

Table 6-3 shows the GRAVSOFT software required to complete the restore step. The spatial extent of all datasets are ϕ $[15.25°, 27.75°]$ and λ $[50.75°, 61.25°]$.

Table 6-3. Restore step workflow

	Description	Input	Software	Output
Calculate Quasi-Geoid				
1A	Add N_{egm08} D/O 360 to $\zeta_{\Delta g_{res}}$	$\boldsymbol{\zeta_{\Delta g_{res}}}_{[30"\times30"]}$ $\boldsymbol{\zeta_{egm08}}_{[30"\times30"]}$	**GCOMB** in mode 2	$\boldsymbol{\zeta_{temp}}_{[30"\times30"]}$
1B	Calculate ζ_{ter}	$\boldsymbol{\Delta g_{ter}}_{[30"\times30"]}$	**SPFOUR**[1]	$\boldsymbol{\zeta_{\Delta g_{ter}}}_{[30"\times30"]}$
1C	Add $\zeta_{\Delta g_{ter}}$ to N_{temp}	$\boldsymbol{\zeta_{temp}}_{[30"\times30"]}$ $\boldsymbol{\zeta_{\Delta g_{ter}}}_{[30"\times30"]}$	**GCOMB** in mode 2	$\boldsymbol{\zeta}_{[30"\times30"]}$

[1]Modified for large datasets

6.8 Gravimetric geoid step

The computation of the gravimetric geoid N from the quasigeoid (height anomaly) ζ can be done by calculating the $N - \zeta$ separation term, mentioned previously in Equation (2.24). The $N - \zeta$ correction is calculated using GCOMB in mode 9, and is added to the quasigeoid computed in Equation (6.4) to get the gravimetric geoid using GCOMB in mode 2. Figure 6-4 shows the unfitted gravimetric geoid.

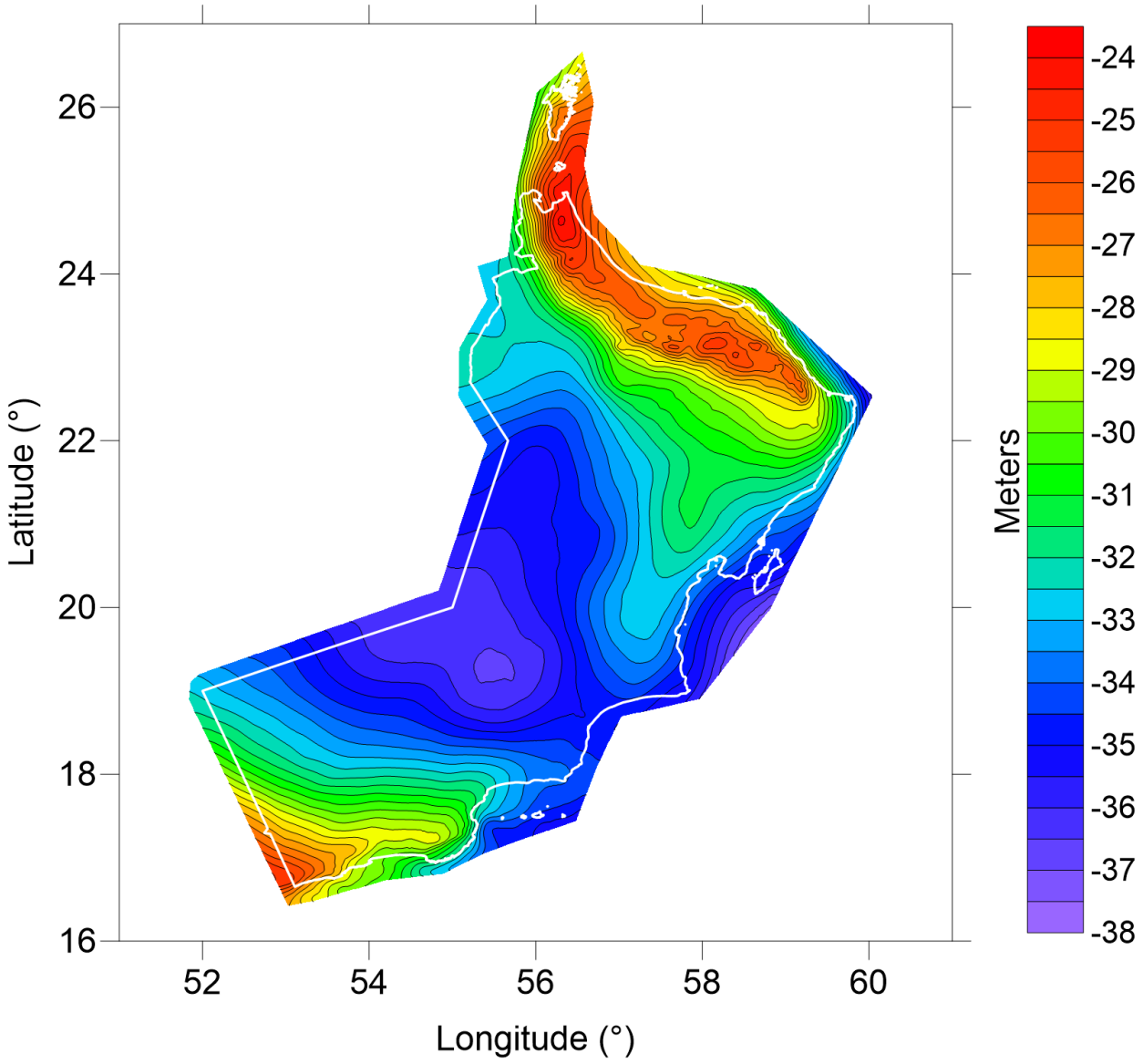

Figure 6-4. Unfitted gravimetric geoid.

6.9 Gravimetric geoid workflow

Table 6-4 shows the GRAVSOFT software required to compute the gravimetric geoid undulations from the height anomalies. The spatial extent of all datasets is ϕ $[15.25°, 27.75°]$ and λ $[50.75°, 61.25°]$.

Table 6-4. Compute gravimetric geoid *workflow*

	Description *Calculate Gravimetric Geoid*	Input	Software	Output
1A	Compute $(N-\zeta)$ corrections	$\boldsymbol{\Delta g_{sbg}}_{[30"\times 30"]}$ $\boldsymbol{SRTM}_{[30"\times 30"]}$	**GCOMB** in mode 9	$(\boldsymbol{N-\zeta})_{[30"\times 30"]}$
1B	Compute Geoid	$\boldsymbol{\zeta}_{[30"\times 30"]}$ $(\boldsymbol{N-\zeta})_{[30"\times 30"]}$	**GCOMB** in mode 2	$\boldsymbol{N}_{[30"\times 30"]}$

6.10 Fitting the gravimetric geoid model to GPS-on-benchmarks

The main application of the geoid for surveying is the acquisition of the orthometric height of a point, without measuring height differences and gravity in geodetic (spirit) levelling. Due to datum inconsistencies (tide gauge datum), errors embedded in the Orthometric heights H determined by geodetic levelling, errors in the Global Navigation Satellite System (GNSS) geodetic height h, and undoubtedly errors in the gravimetric geoid height N; it is often useful to fit the gravimetric geoid model to the geometric geoid model determined from the well-known relationship shown in Equation (2.27) at selected high precision benchmarks across the country. Such benchmarks are often called “GPS-on-benchmarks” that define the height reference frame in the country. The fitting of the gravimetric geoid to such benchmarks will allow users to determine orthometric heights from GNSS observations and the fitted geoid that are compatible with the national height system.

In addition to providing consistency to surveyors and engineers, the results of the fitting can be used to assess the external accuracy of the gravimetric geoid model. If it is assumed that the GPS-on-benchmarks and their associated orthometric heights are of good quality, then the geometric geoid can be computed using Equation (2.27). The geometric geoid can be used to determine the quality of the gravimetric geoid model by calculating the difference in geoid undulation N for each benchmark. The differences ΔN are calculated using Equation (6.5).

$$\Delta N = N_{geom} - N_{grav} \tag{6.5}$$

Gridding the calculated differences will result in a surface that can be added to the gravimetric geoid to create the “fitted geoid” on GPS-on-benchmarks.

6.11 Geoid fitting step workflow

Table 6-5 shows the Surfer software required to fit the gravimetric geoid to the GPS-on-benchmarks. The spatial extent of all datasets are ϕ $[15.25°, 27.75°]$ and λ $[50.75°, 61.25°]$.

Table 6-5. Fitting of gravimetric geoid workflow

	Description	Input	Software	Output
Fitting Gravimetric Geoid to GPS-on-Benchmarks				
1A	Compute GPS-On-benchmark residuals	$\boldsymbol{N}_{[30"\times30"]}$ **Geometric Geoid** for each GPS-On Benchmark	**Surfer** *Grid|Residuals*	Residual[2] for each GPS-On-Benchmark
1B	Grid Residuals	**Residual[2]** for each GPS-On Benchmark	**Surfer** *Grid|Data*	$\boldsymbol{Gridded\ Residuals}_{[30"\times30"]}$
1C	Fit Geoid	$\boldsymbol{N}_{[30"\times30"]}$ $\boldsymbol{Gridded\ Residuals}_{[30"\times30"]}$	**Surfer** *Grid|Math (add)*	$\boldsymbol{N_{fitted}}_{[30"\times30"]}$

[2] Surfer defines residuals as $N_{geom} - N_{grid}$

6.12 Summary

This chapter presented in detail the remove-compute-restore (RCR) method and how it was applied to calculate the gravimetric quasigeoid. The workflow for each step in the process was also included. In addition to the RCR method, the conversion from the quasi-geoid to the gravimetric geoid was presented along with the steps required to fit the gravimetric geoid to the geometric geoid using GPS-on-benchmarks.

7 Final Results

7.1 Geoid fit testing

To test the gravimetric geoid model, and subsequently fit it to GPS-on-benchmarks, 370 GPS-on-benchmarks are used; however, not all are considered for fitting the gravimetric geoid. Of the 370 points, 39 are 1st order, 284 are 2nd order, and 47 were specifically observed for the ONGM project. The location of the benchmarks and their gridded residuals with respect to the gravimetric geoid model are shown in Figure 7-1.

Nine benchmarks have relatively large residuals greater than $\pm$ 1 m, and are designated gross outliers, and removed. The large difference is likely a result of a combination of poorly observed geodetic and orthometric heights, as it is highly unlikely that the geoid would differ from the benchmarks to that level. These large residuals also appeared when comparing the GPS-on-benchmarks to full expansion EGM08 and GOCO05s geoid models, further supporting the claim that the height measurements have errors.

The remaining benchmarks are then used to produce the updated difference map shown in Figure 7-2 with their histogram in Figure 7-3. There are still multiple locations with large residuals (>$\pm$ 25 cm) that are inconsistent, relative to their surroundings. These are circled and numbered in Figure 7-2. The first six circles include one or two outlier points (8 in total) with large residuals situated in an area with comparatively smaller ones. The geoid is a smooth surface in these regions, and cannot explain abrupt residual changes for single point(s) on a levelling line. Neighboring the large residuals there exist benchmarks with very small residuals. Since all levelling lines are consistent with the reference benchmarks and exhibit misclosures at the sub-centimeter level, it is highly unlikely that only one benchmark in the levelling line is off by up to several decimeters. It is highly possible that the geodetic height used to calculate the geometric geoid at such benchmarks contain a large systematic error, likely due to adverse atmospheric conditions, poor field procedures, and/or severe multipath, or the observed orthometric height at each benchmark was not determined correctly (e.g. no gravity measurements). Furthermore, the benchmarks with larger residuals also had the same problem when testing them with other independent geoid models, such as GOCO05s and EGM08. As a result, the eight outlier benchmarks are removed leaving 347 points available to fit the geoid.

The larger discrepancies in regions seven and eight are also examined. The benchmarks in each region that reach +60 cm and –60 cm, respectively, belong to the same levelling line. Since in these regions the geoid is relatively flat (see Figure 6-4) and over a flat topography (see Figure 3-4), EGM08 and GOCO05s GGMs can also be used to test the geometric geoid. As a result of these tests, the said large discrepancies remain. Since the computed gravimetric geoid model differs from the two reference models by a few centimeters at most in these regions, the geodetic height of these benchmarks is likely the cause of discrepancies. Unlike the problems in the first six regions, which span small areas, these benchmarks are not removed as they cover extended areas rather than being single benchmarks. Until new high precision GNSS or orthometric height measurements become available, the fitted geoid in these regions will be biased by a few decimeters.

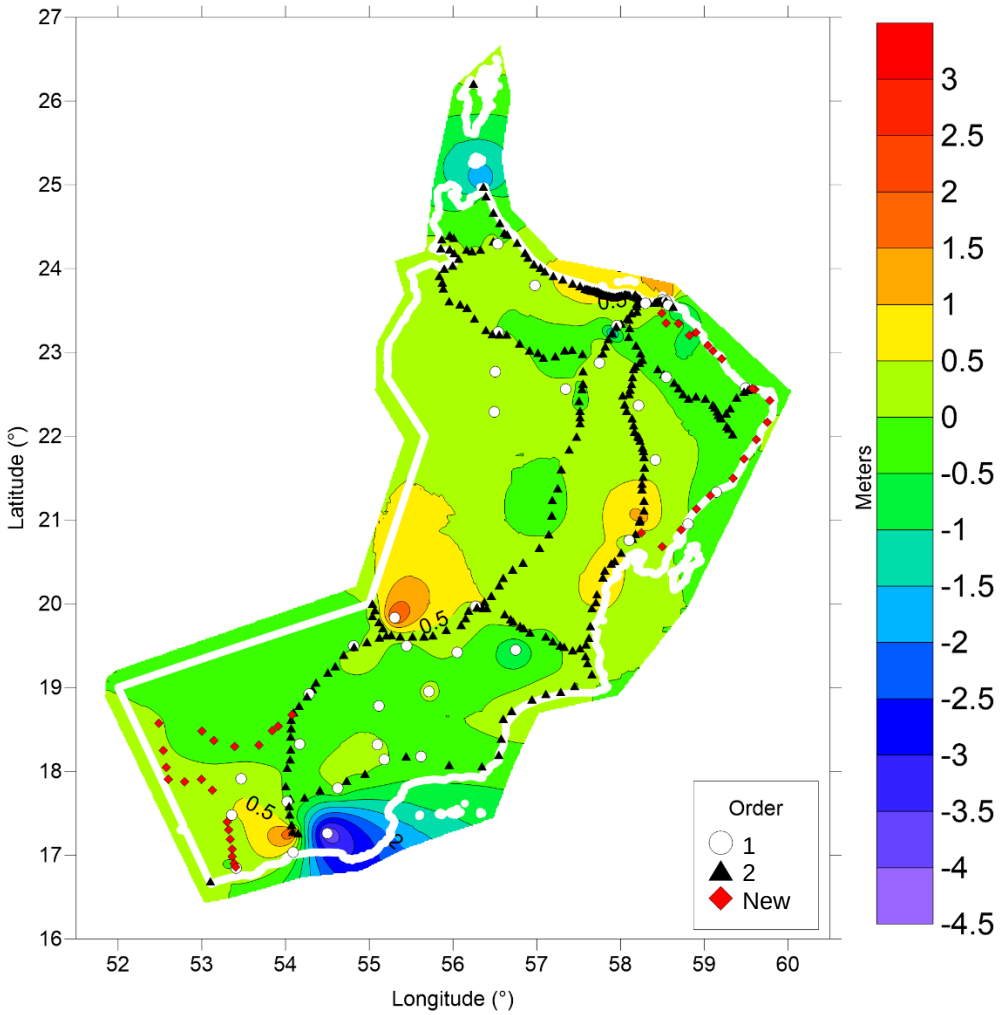

Figure 7-1. Benchmark locations. *The white circles are the primary 1st order benchmarks, the black triangles are the 2nd order points referenced to the 1st order benchmarks, and the new observation points are the red diamonds referenced to both 1st and 2nd order points. The background map shows the gridded residuals of all benchmarks.*

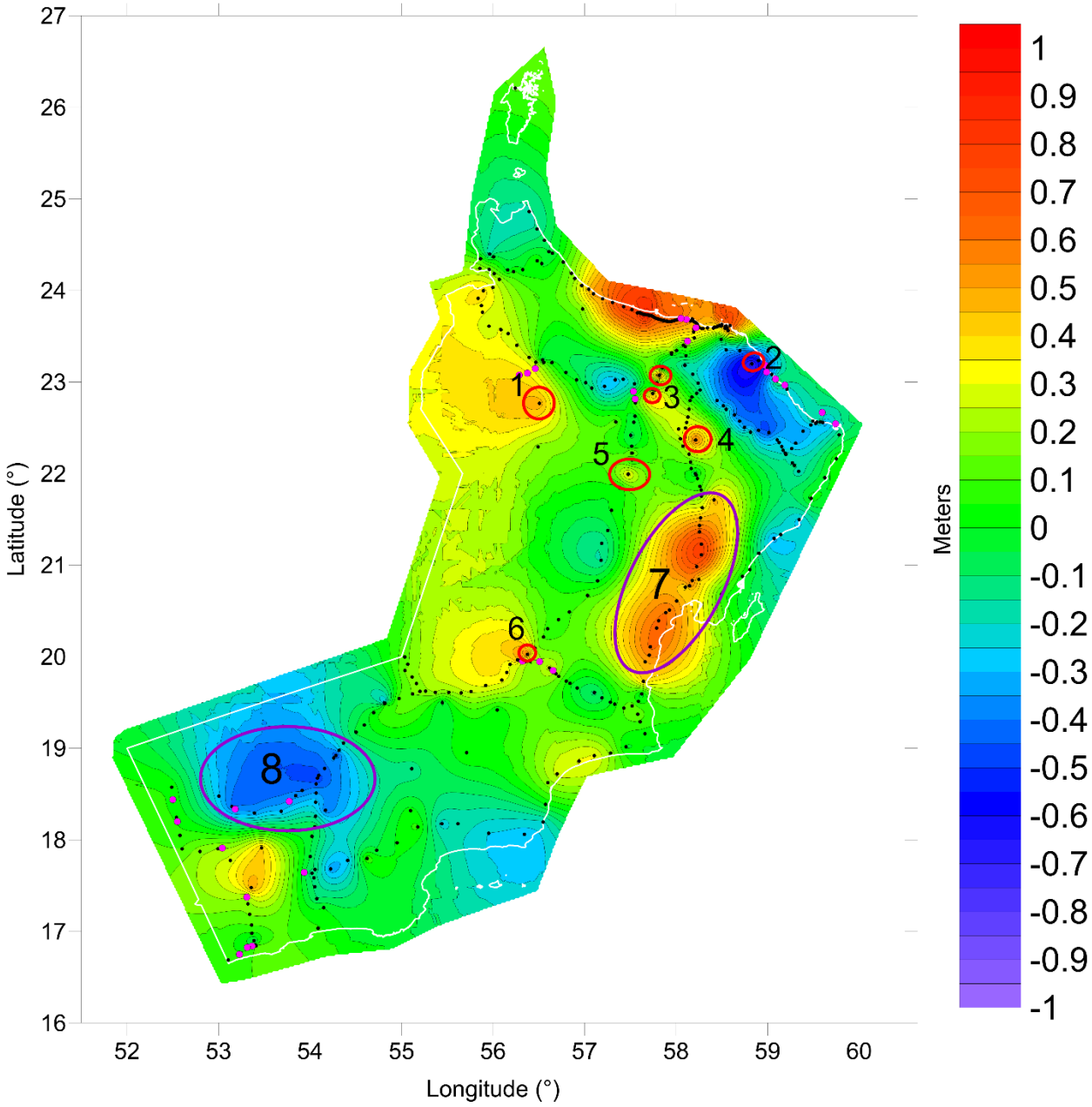

Figure 7-2. Benchmark residuals from -1 m to 1 m. *The large differences in the circled areas are discussed in the text above.*

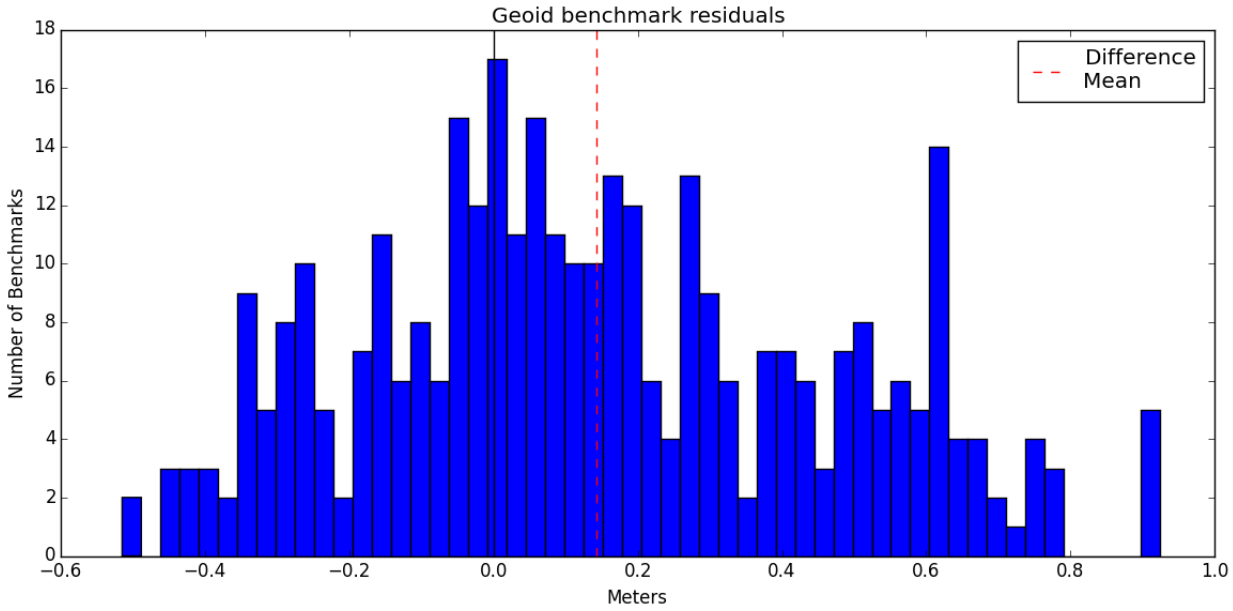

Figure 7-3. Histogram of geoid benchmark residuals*. The average difference is 14.3 cm, and the standard deviation is ± 30 cm.*

Finally, the histogram of the residuals of the differences between the fitted geoid and the GPS-on-benchmarks can be seen in Figure 7-4.

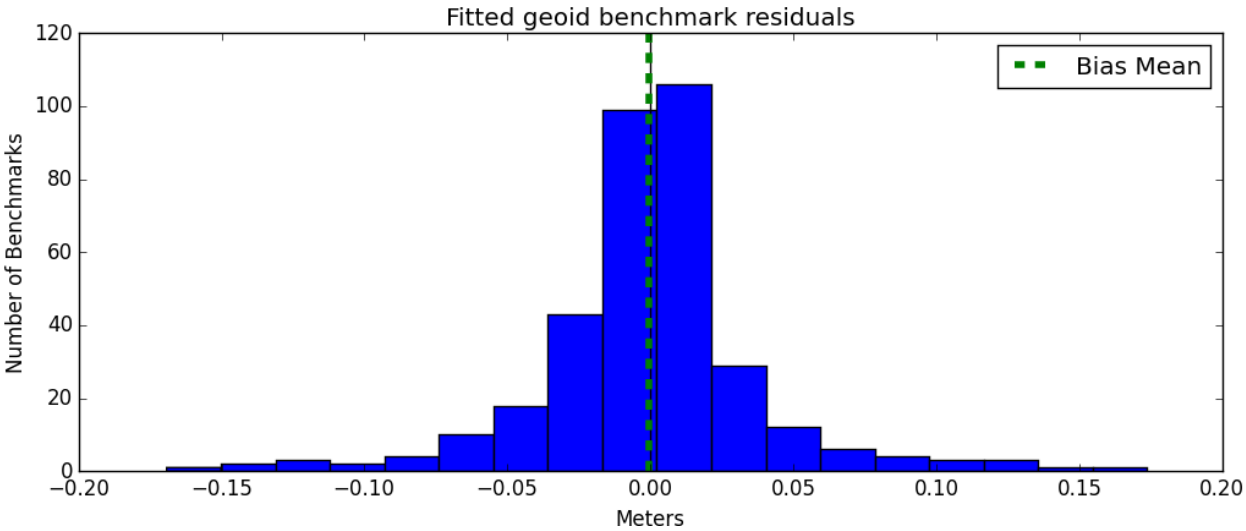

Figure 7-4. Histogram of differences between GPS-on benchmarks and the fitted gravimetric geoid*. The average difference is zero, and the standard deviation is ± 3.8 cm.*

7.2 Comparison of the Oman gravimetric geoid to GOCO05S global geopotential model

In addition to comparing the gravimetric geoid to the GPS-on benchmarks, it was also compared to a commonly used satellite based global geopotential model, GOCO05s (Mayer-Gürr et al., 2015). While the maximum degree and order (280) GOCO05s geoid cannot characterize the complete gravimetric geoid, it does provide a good indication of the external accuracy of the Oman geoid. Figure 7-5 and Figure 7-6 show the differences between the two models and their histogram, respectively. The major differences, as expected, are in Oman's mountainous regions, but the two geoids agree (< 20 cm) throughout the rest of the country.

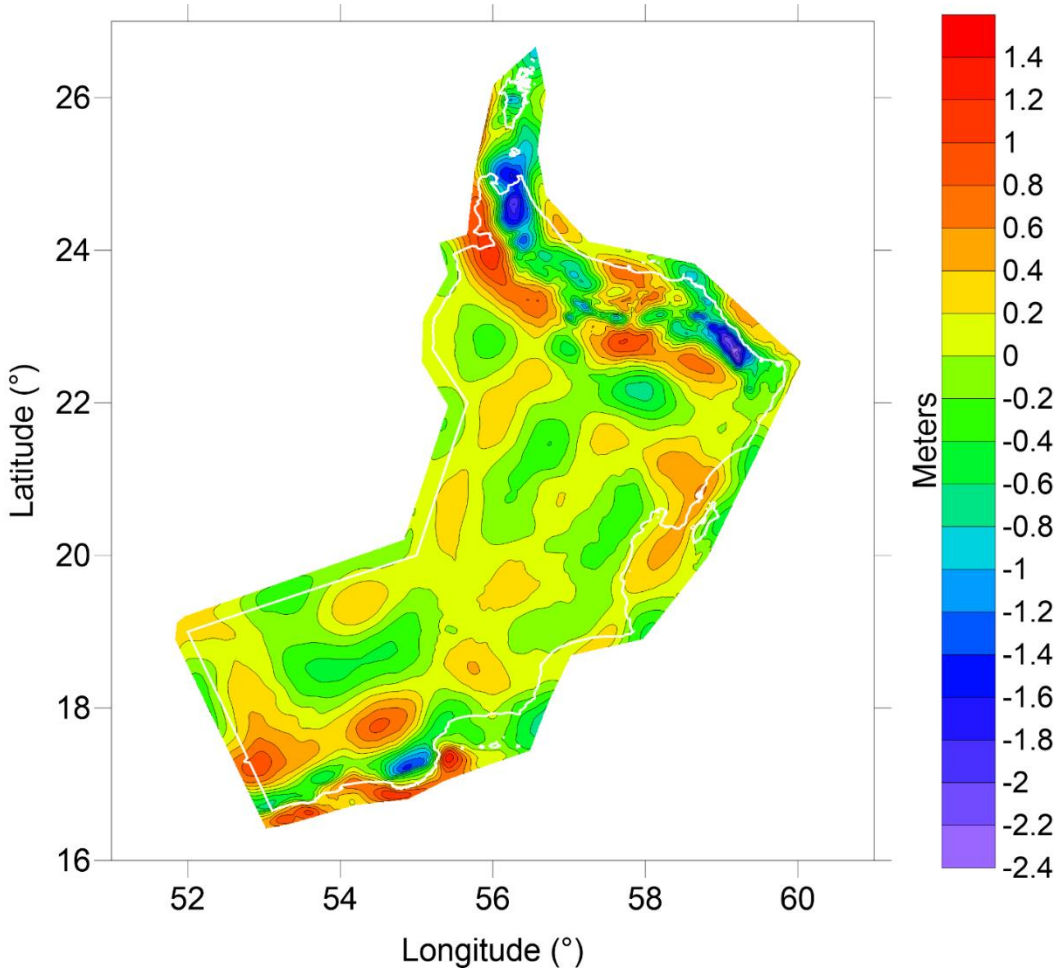

Figure 7-5. Difference between GOCO05S GGM and the gravimetric geoid. *The high frequency differences in the mountains are a result of the GGM not completely characterizing the rapid transitions of Oman's northern mountainous terrain.*

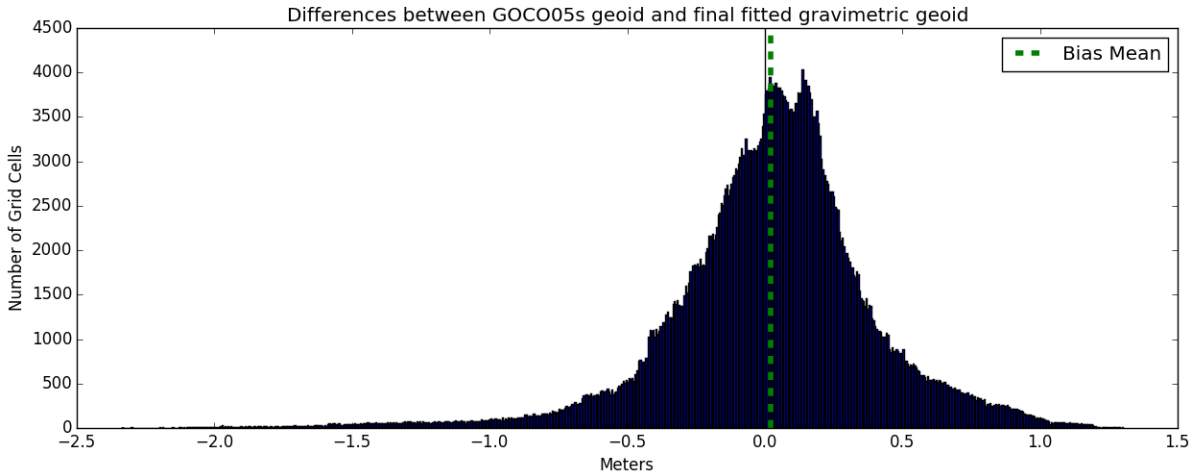

Figure 7-6. Histogram of differences between GOCO05S and the gravimetric geoid*. The average difference is 2.2 cm, with a standard deviation of ± 37.8 cm. The large peak on the right side of the histogram signifies the difference in frequency between the medium frequency gravimetric geoid and the low frequency satellite determined geoid.*

7.3 Important remarks on the accuracy of the Oman gravimetric geoid model

The unfitted gravimetric geoid model is on average 14 cm lower than the mean sea level (MSL) defined by the levelled heights (MSL) at all test benchmarks discussed in the previous section. This agrees well with the sea surface topography (SST) in the region as determined by satellite altimetry (Andersen & Knudsen, 2009).

One of the reasons for the gravimetric geoid misfit in certain regions of limited extent, and also at single benchmarks, is most probably due to errors in the geodetic heights. Verification of the accuracy of the GPS-on-benchmarks from the GPS perspective is required. The questionable benchmarks found to be incompatible with the geoid model could be re-observed with minimal effort to verify their geodetic and orthometric heights.

It is unclear whether the height network in Oman is in an orthometric height system. From careful examination of various technical reports, it is suspected that the heights of the benchmarks provided are in some normal height system. This might have introduced additional discrepancies between the gravimetric geoid and the GPS-on-benchmarks. For the 1st and 2nd order benchmarks, verification of reductions and calculations must be revisited and a readjustment of the height network of Oman must be performed.

8 Conclusions and recommendations

8.1 Summary and conclusions

In this research, the task of developing the Oman National Geoid Model (ONGM) was undertaken. A legacy ground gravity dataset was available from the National Survey Authority (NSA) of Oman, with approximately 230 000 point gravity observations. In addition, a newly observed ground gravity dataset of about 6000 points, a newly observed airborne dataset with countrywide coverage, and a set of GPS observations on Oman's current leveled benchmarks were available for this research.

The main challenges for completing this work were concentrated on the quality of the available datasets and in particular the legacy ground gravity dataset that was observed over a period of at least fifty years using various techniques, instruments and data processing methodologies whose description (metadata) was not available. In addition, the scope under which the observations were collected and the reduction methods used were for natural resource exploration and may not be suitable for the determination of the geoid model of Oman at the centimetre level of accuracy. Moreover, over the long period of the data collection, the geodetic reference systems used for processing the observations have become obsolete for modern geoid computations.

Ground gravity observations provide the high frequency components of a geoid model, that is, they make possible the calculation of the detailed short wavelength geoid structure that is indispensable for accurate GNSS levelling. As such, the legacy gravity dataset, despite its inherent problems and inconsistencies, was deemed very important for the ONGM, and a necessary addition to the recent airborne and limited new ground gravity measurements. The main contribution of this thesis was the launching and completion of a very long forensic investigation of the legacy gravity data, in complete absence of critical metadata, to render them useful and suitable for integration with the airborne data for the ONGM.

The investigation and subsequent repair of the data included the following main contributions that are described in detail in Chapters 3, 4, and 5:

1.) Identification and verification of the geodetic reference system used to provide positional information for the point gravity observations.

2.) Identification of the type of the original data, such as the type of gravity anomalies provided, which were missing in the vast majority of original gravity observations and had unknown reduction methods.
3.) Developing algorithms for the transformation of the old geodetic reference systems, such as from PDO Survey Datum of 93 (PSD93), to the modern WGS84 reference system.
4.) Development of inverse calculation algorithms to recover proxy gravity values for about 75 percent of the observations.
5.) Removing significant biases from the gravity anomalies using many different approaches, including the use of the airborne gravity anomalies. These methodologies are very useful for many other countries that hold legacy data with referencing problems.
6.) Developing spatial filtering methodologies for ground and airborne gravity anomalies for their correct integration with no frequency overlap.
7.) Deciphering the inner workings of the GRAVSOFT software package from very limited and vague documentation, including thorough testing of the functions used in this thesis.
8.) Developing software modules with Python to achieve integration of various data types, file formats, and software such as GRAVSOFT and Surfer, with minimal user input.
9.) Developing clear and well-documented automated processes on the use of GRAVSOFT for future geoid modelling work.

In summary, the following tasks were completed successfully:

1.) An inversely computed ground gravity dataset was created from ~230 000 previously observed Bouguer anomalies. Each point was assigned a new orthometric height based on NASA's SRTM using its newly converted latitude and longitude values from the PSD93 datum. The free air anomalies calculated from the dataset were biased, at most, by 100 milligals with respect to airborne free air anomalies at altitude. Attempts were made to rectify this by utilizing all available survey documentation and field notes with minimal success.
2.) The biased ground free air anomalies were repaired using airborne free air anomalies at altitude. It was postulated that the histograms of the short wavelength component of the unbiased ground data and the airborne data were the same. The difference between the means of each pair of histograms was added to the biased gravity to repair it.
3.) The unbiased free air anomalies were converted to complete Bouguer anomalies, gridded, then converted back to free air anomalies. This process injected the high frequency

component arising from the roughness of the terrain, into the ground free air anomaly dataset.

4.) The ground free air anomalies were high-pass filtered to extract their medium to high frequency components, which were then added to low-pass filtered downward continued airborne free air anomalies. This created the final free air anomaly dataset. The final dataset was compared to a full expansion GOCO05s GGM. The two models agreed on the low to medium frequencies, but differed in the high frequency. The mean of the differences between the two models was -3.25 mGal, with the majority of differences present in the mountainous regions of the country.

5.) The geoid was computed using the remove-compute-restore method. The RTM method was used to characterize the terrain effects for the remove step. It was computed using a GEBCO bathymetry model mixed with a 30" NASA SRTM DTM. The harmonic component removed was a D/O 360 expansion of the EGM08 GGM. The resultant "residual" anomalies were run through GRAVSOFT's implementation of the Stokes integral using Wong-Gore Tapering to remove effects below D/O 360. The gravimetric quasigeoid was computed by restoring the geoidal equivalents of both removed effects, and was then converted to the gravimetric geoid by adding the $N - \zeta$ effects to it. The gravimetric geoid was compared to a full expansion GOCO05s GGM geoid, and the two were approximately equal everywhere, except in Oman's mountainous regions. The mean of the differences was 2.2 cm.

6.) The gravimetric geoid was fitted to GPS-on-benchmarks to provide an estimate of the external accuracy of the geoid. The initial fit had a mean residual (geometric geoid – gravimetric geoid) of ~17 cm, but had nine gross outlier points with residuals greater than $\pm$ 1 m, which were removed. After removing a few more discontinuous outlier points, the remaining points had a mean of ~14 cm that agreed with the sea surface topography in the region. The final fitted gravimetric geoid had a mean residual of zero centimeters, with a standard deviation of $\pm$ 3.8 cm.

8.2 Recommendations

The following recommendations can be made with respect to the Oman National Geoid Model project and future geoid modeling research.

1. The accuracy of the geodetic height measurements of the GPS-on-benchmarks need to be verified, as the majority of the very large outlier benchmark residuals were due to improperly measured geodetic heights. In the future, detailed notes about the measurement practices and corrections applied to each measurement must be archived.
2. The spirit levelled heights need to be properly converted from height differences to orthometric heights using observed gravity. The current height measurements labelled as orthometric heights are not theoretically correct.
3. Measuring of the crustal mass density will contribute to more accurate orthometric heights as well as making it possible to have centimeter level geoid accuracy (Huang et al., 2001). The density will be used to better characterize the topography when dealing with the remove step of geoid calculation, or when computing any type of Bouguer anomaly.
4. The coverage of the legacy ground gravity dataset can be increased in areas where sparse gravity information is currently available. Prime locations for this extra coverage are the mountainous regions in northern Oman, and other areas in the southwestern part of the country. In addition, gravity can be observed at key locations in the gravity observation lines that were found to have large biases, but different shapes, to provide a secondary method of repairing heavily biased observation lines.
5. The gravity dataset can be augmented outside of Oman's borders; either using a full expansion high frequency GGM, or by collaborating with neighboring countries. This augmentation will increase the accuracy of the geoid near the country's borders.

References

Alpay Abbak, R., Erol, B., & Ustun, A. (2012). Comparison of the KTH and remove-compute-restore techniques to geoid modelling in a mountainous area. *Computers and Geosciences*.

Andersen, O. B., & Knudsen, P. (2009). DNSC08 mean sea surface and mean dynamic topography models. *Journal of Geophysical Research*.

Bajracharya, S., Kotsakis, C., & Sideris, M. G. (2001). Geoid Determination Using Different Gravity Reduction Techniques. *Presented in IAG meeting.* Budapest.

BODC, B. O. (2016). The General Bathymetric Chart of the Oceans.

DMA, D. M. (1987). *DMA TECHNICAL REPORT TR8350.2-a.*

Forsberg, R. (1984). *A study of terrain reductions, density anomalies and geophysical inversion methods in gravity field modelling.* Ohio State University.

Forsberg, R. (2002). GRAVSOFT subroutine SPFOUR [Computer Software].

Forsberg, R., & Tscherning, C. (1981). *The use of height data in gravity field approximation by collocation.*

Forsberg, R., & Tscherning, C. (2008). GRAVSOFT.

Forsberg, R., Solheim, D., & Kaminskis, J. (1996). Geoid of the Nordic and Baltic Region from Gravimetry and Satellite Altimetry. *International Symposium of Gravity, Geoid and Marine Geoidesy (GRAGEOMAR)* (pp. 540-547). Tokyo: Springer.

Fukuda, Y., & Segawa, J. (1990). Derivation of the Most Reliable Geoid in the Area of Japan and Some Comments on the Variability of Sea Surface Topography. *Determination of the Geoid: Present and Future*, (pp. 191-199). Milan.

Ganeko, Y. (1983). A 10'x10' Detailed Gravimetric Geoid Around Japan. *Marine Geoid 7*, 291-314.

Géophysique GPR I'ntl Inc. (2015). *GT-1A airborne gravity project filed operations and data processing. Report on the Establishment of Oman National Geoid Model (ONGM) for the Sultanate of Oman - Ministry of Defence GT-1A Airborne Gravity Survey.*

Gorokhovich, Y., & Voustianiouk, A. (2006). Accuracy assessment of the processed SRTM-based elevation data by CGIAR using field data from USA and Thailand and its relation to the terrain characteristics. *Remote Sensing of Environment*, 409-415.

Heiskanen, W., & Moritz, H. (1967). *Physical Geodesy.* Institute of Physical Geodesy.

Hofmann-Wellenhof, B., & Moritz, H. (2006). *Physical Geodesy.*

Huang, J., Vaníček, P., Pagiatakis, S. D., & Brink, W. (2001). Effect of topographical density on geoid in the Canadian Rocky Mountains. *Journal of Geodesy*, 805-815.

Kuhn, M., & Hirt, C. (2016). *Examination of approximation errors caused by Rock-Equivalent Topography (RET) for the topographic gravitational potential and its first and second derivatives.*

Liard, J., & Gagnon, C. (1993). *Absolute Gravity Survey in theSultanate of Oman.* Geological Survey of Canada. Natural Resources Canada.

Mayer-Gürr, T., & et al. (2015). The combined satellite gravity field model GOCO05s. *European Geosciences Union.* Vienna.

Moritz, H. (1968). *On the use of the terrain correction in solving Molodensky's problem.* Department of Geodetic Science.

NASA, N. A. (2016). Shuttle Radar Topography Mission.

Novak, P., & Heck, B. (2002). Downward continuation and geoid determination based on band-limited airborne gravity data. *Journal of Geodesy, 76*, 269-278. doi:10.1007/s00190-002-0252-y

NSA. (1993). *Establishment of Oman National Geodetic Datum.* National Survey Authority, Ministry of Defense, Sultanate of Oman.

Omang, O., & Forsberg, R. (2000). How to handle topography in practical geoid determination: three examples. *Journal of Geodesy*.

Ravaout, P. (1996). *The Bouguer Anomaly Map of Oman. A synthesis of existing gravity data.* Ministry of Petroleum and Minerals. National Survey Authority.

Sansó, F. (1994). *Lecture notes, International School for the Determination and Use of the Geoid.* Milan: International Geoid Service, DIIAR- Politechnico di Milano.

Sideris, M. G., & She, B. B. (1995). A new, High-resolution geoid for Canada and part of the U.S by the 1D-FFT method. *Bull Géod 69*, 92-108.

Sjöberg, L. (1984). *Least Squares Modification of Stokes and Venning-Meinesz Formulas by Accounting for Errors of Truncation, Potential Coefficients and Gravity Data.* Institude of Geophysics, University of Uppsala, Department of Geodesy.

Sjöberg, L. (1991). Refined Least Squares Modification of Stokes Formula. *Manuscripta Geodaetica 16*, 367-375.

Sjöberg, L. (2003). A General Model of Modifying Stokes Formula and its Least Squares Solution. *Journal of Geodesy*, 790-804.

Sjöberg, L. (2005). A discussion on the approximations made in the practical implementation of the remove-compute-restore technique in regional geoid modelling. *Journal of Geodesy*.

Tocho, C., Font, G., & Sideris, M. (2005). *Gravimetric Geoid Determination in the Andes.*

Vanicek, P. (1974). *Brief Outline of the Molodenskij Theory.* Lecture Notes, UNB, Geodesy and Geomatics Engineering.

Whitaker, J. (2016). pyproj: Python interface to PROJ.4 library. Retrieved from https://pypi.python.org/pypi/pyproj